Solution-Based Electrical P-type Doping of Semiconducting Polymer Films Over a Limited Depth in High-Performance Organic Photovoltaic Devices

A Thesis
Presented to
The Academic Faculty

by

Vladimir A. Kolesov

In Partial Fulfillment
of the Requirements for the Degree
Doctor of Philosophy in the
School of Electrical engineering

Georgia Institute of Technology
August 2017

Solution-Based Electrical P-type Doping of Semiconducting Polymer Films Over a Limited Depth in High-Performance Organic Photovoltaic Devices

Approved by:

Dr. Bernard Kippelen
School of Electrical Engineering
Georgia Institute of Technology

Dr. Azad Naeemi
School of Electrical Engineering
Georgia Institute of Technology

Dr. Oliver Brand
School of Electrical Engineering
Georgia Institute of Technology

Dr. Samuel Graham
School of Mechanical Engineering
Georgia Institute of Technology

Dr. Andrew Peterson
School of Electrical Engineering
Georgia Institute of Technology

Date Approved: April, 3, 2017

ACKNOWLEDGEMENTS

This work was made possible with the immense support of my family, friends, and colleagues throughout the years of my Ph.D.. First and foremost, I would like to thank my advisor Dr. Bernard Kippelen, who's guidance and patience played an important and key role in my work and development as a researcher. His hard efforts throughout the years have provided the resources, equipment, and funding necessary to conduct high caliber research. I would also like to express my gratitude to Dr. Peterson, Dr. Brand, Dr. Naeemi, and Dr. Graham for all of their advice and for agreeing to take the time to serve on my committee.

Specifically, I would like to thank Dr. Keith Knauer who provided me with assistance, training, and guidance throughout the first year of the Ph.D. program. Also, thank you to Dr. Canek Fuentes-Hernandez who is an immeasurable source of knowledge. Without his involvement, guidance, feedback, and insights, a lot of this work would not have been possible and for that I am very much indebted to him. I have also benefited greatly from the numerous discussions with past and present group member throughout the years and would like to thank them for their support: Dr. Michael Gaj, Dr. Amir Dindar, Dr. Talha Khan, Dr. Jae Won Shim, Dr. Yinhua Zhou, Dr. James Hsu, Dr. Ehsan Najafabadi, Dr. Sangmoo Choi, Dr. Cheng-Yin Wang, Felipe Larrain, Victor Rodriguez-Toro, and Wen-Fang Chou. Also, a big thanks to Dr. Naoya Aizawa who made the initial contribution to this work.

This work was funded in part by the Department of the Navy, Office of Naval Research Award No. N00014-14-1-0580 and N00014-16-1-2520, through the MURI

Center CAOP, Office of Naval Research Award N00014-04-1-0313 and by the Department of Energy through the Bay Area Photovoltaic Consortium under Award Number DE-EE0004946.

Finally, and most importantly, I would like to express how grateful I am for the support of my parents Alexander Kolesov and Irina Kolesova and my brother, Ivan Kolesov, who have provided me with support and encouragement throughout my entire tenure at Georgia Tech. My achievements would not have been possible without their hard work, assistance, and inspiration to pursue the highest level of education. I would not have been afforded this incredible opportunity without their numerous sacrifices, and I consider this achievement as much theirs as it is mine.

TABLE OF CONTENTS

LIST OF TABLES

LIST OF FIGURES

LIST OF SYMBOLS AND ABBREVIATIONS

PV	Photovoltaics
LCOE	Levelized Cost of Energy
AM0	Air Mass
PCE	Power Conversion Efficiency
CIGS	$Cu(InGa)Se_2$
OSC	Organic Solar Cells
OPV	Organic Photovoltaics
DSSC	Dye Sensitized Solar Cells
EPBT	Energy Payback Time
MEH-PPV	poly(2-methoxy-5-(2-ethyl)-hexyloxy-p-phenylenevinylene)
BHJ	Bulk Heterojunction
PEDOT:PSS	Poly(3,4-ethylenedioxythiophene) polystyrene sulfonate
PEI	Polyethylenimine
PEIE	Polyethylenimine Ethoxylated
PEG	Poly(ethylene glycol)
PMA	Phosphomolybdic Acid
PTA	Phosphotungstic Acid
POM	Polyoxometalate
PVK	Poly(N-vinylcarbozole)
OLED	Organic Light-Emitting Diode
IPA	2-propanol
PCDTBT	Poly[*N*-9′-heptadecanyl-2,7-carbazole-alt-5,5-(4′,7′-di-2-thienyl-2′,1′,3′-benzothiadiazole)]

OFET	Organic Field-Effect Transistor
LCAO	Linear Combination of Atomic Orbitals
MO	Molecular Orbital
HOMO	Highest Occupied Molecular Orbital
LUMO	Lowest Unoccupied Molecular Orbital
IP	Ionization Potential
EA	Electron Affinity
E_{fund}	Fundamental Gap
E_{opt}	Optical Gap
E_B	Binding Energy
WF	Work Function
PET	Polyethylene Terephthalate
PEN	Polyethylene Naphthalate
D-A	Donor-Acceptor
CT	Charge Transfer
CS	Charge Separated
$LUMO_A$	Lowest Unoccupied Molecular Orbital of Acceptor
$HOMO_D$	Highest Occupied Molecular Orbital of Donor
F4-TCNQ	2,3,5,6-tetrafluoro-7,7,8,8-tetracyanoquinodimethane
P3HT	poly(3-hexylthiophene-2,5-diyl)
PIPCP	poly-[4,4,9,9-tetrakis(4-hexylphenyl)-4,9-dihydro-s-indaceno[1,2-b:5,6-b']dithiophene-2,7-yl}-alt-{2,6-bis([1,2,5]thiadiazolo[3,4-c]pyridine-4'-yl)-4,4-bis(2-ethylhexyl)-cyclopenta[2,1-b:3,4-b']dithiophene-7',7''-yl]
PffBT4T-2OD	poly[(5,6-difluoro-2,1,3-benzothiadiazol-4,7-diyl)-alt-(3,3'''-di(2-octyldodecyl)-2,2';5',2'';5'',2'''-quaterthiophen-5,5'''-diyl)]
$PC_{61}BM$	[6,6]-Phenyl C61 butyric acid methyl ester

$PC_{71}BM$	[6,6]-Phenyl C71 butyric acid methyl ester
ICBA	1',1'',4',4''-tetrahydro-di[1,4]methanonaphthaleno[5,6]fullerene-C60
CB	Chlorobenzene
DCB	1,2-Dichlorobenzene
PTB7	poly[(4,8-bis-(2-ethylhexyloxy)-benzo(1,2-b:4,5-b′)dithiophene)-2,6-diyl-alt-(4-(2-ethylhexyl)-3-fluorothieno[3,4-b]thiophene-)-2-carboxylate-2-6-diyl)]
PBDTTT-C	poly[(4,8-bis-(2-ethylhexyloxy)-benzo(1,2-b:4,5-b′)dithiophene)-2,6-diyl-alt-(4-(2-ethylhexanoyl)-thieno[3,4-b]thiophene-)-2-6-diyl)]
ITO	Tin-doped Indium Oxide
R_{SH}	Sheet Resistance
DI	Deionized
PTFE	Polytetrafluoroethylene
PDMS	Polydimethylsiloxane
TLM	Transmission Line Method
CPD	Contact Potential Difference
HOPG	Highly Ordered Pyrolytic Graphite
XPS	X-ray Photoelectron Spectroscopy
IR	Infrared
EQE	External Quantum Efficiency
NIR	Near Infrared
TIPS-pentacene	6,13-bis(triisopropylsilylethynyl) pentacene
PTAA	poly(triarylamine)
PATPD	poly(acrylic tetraphenyldiaminobiphenol)
J-V	Current-Density – Voltage
AL	Active Layer

IQE	Internal Quantum Efficiency
AFM	Atomic Force Microscopy
XRD	X-ray Diffraction
RBS	Rutherford Backscattering
SIMS	Secondary Ion Mass Spectroscopy

SUMMARY

Organic photovoltaics (OPV) have the potential to be a disruptive technology used for the generation of electricity. Although OPVs currently demonstrate lower power conversion efficiencies than other thin-film solar technologies or their inorganic counterparts, their low cost and high throughput can result in low energy payback times. Due to their high tolerance to defects, OPVs can be fabricated from solution at low temperature. Here it is demonstrated that solution-processed polymer films can be electrically doped with some degree of spatial control, something previously only achieved in organic devices by co-evaporation of small molecule dopants. The addition of these dopants has a significant impact on the optical, electrical, and chemical properties of the polymer films, which can be exploited for high efficiency OPV devices with greatly simplified geometries.

Solution-based electrical doping protocols may allow more versatility in the design of organic electronic devices; yet, controlling the diffusion of dopants in organic semiconductors and their stability has proven challenging. In this dissertation, a solution-based approach is presented for electrical p-doping of films of donor conjugated organic semiconductors and their blends with acceptors over a limited depth with a decay constant of 10 - 20 nm by post-process immersion into a polyoxometalate solution (phosphomolybdic acid, PMA) in nitromethane. PMA-doped films show increased electrical conductivity and work function, reduced solubility in the processing solvent, and improved photo-oxidative stability in air. This approach is applicable to a variety of organic semiconductors used in photovoltaics and field-effect transistors. PMA doping over a limited depth of bulk heterojunction polymeric films, in which amine-containing polymers

were mixed in the solution used for film formation, enables single-layer organic photovoltaic devices, processed at room temperature, with power conversion efficiencies up to 5.9 ± 0.2% and stable performance on shelf-lifetime studies at 60 °C for at least 280 h.

CHAPTER 1

Introduction

1.1 Renewable Energy

With a rising world population and economic developments, the demand for energy is projected to continue to increase in the coming decades. Currently, energy production is dominated by non-renewable fossil-based sources, accounting for 80% of today's energy supply. In 2014, electricity accounted for 15% of total world's energy use [1]. With the total electricity consumption projected to increase 64% by 2040 [2], there have been significant efforts to find more sustainable and environmentally friendly energy sources, also known as renewable energy sources. Renewable energy sources consist of sources such as hydropower, biomass, wind, and solar. In 2015, renewables accounted for an estimated 23.7% of the total generation of electricity [3] and are quickly growing. By 2040, the U.S. Energy Information Administration forecasts that electricity generation from renewables will equal that of coal and natural gas as shown in Figure 1-1 [1, 2].

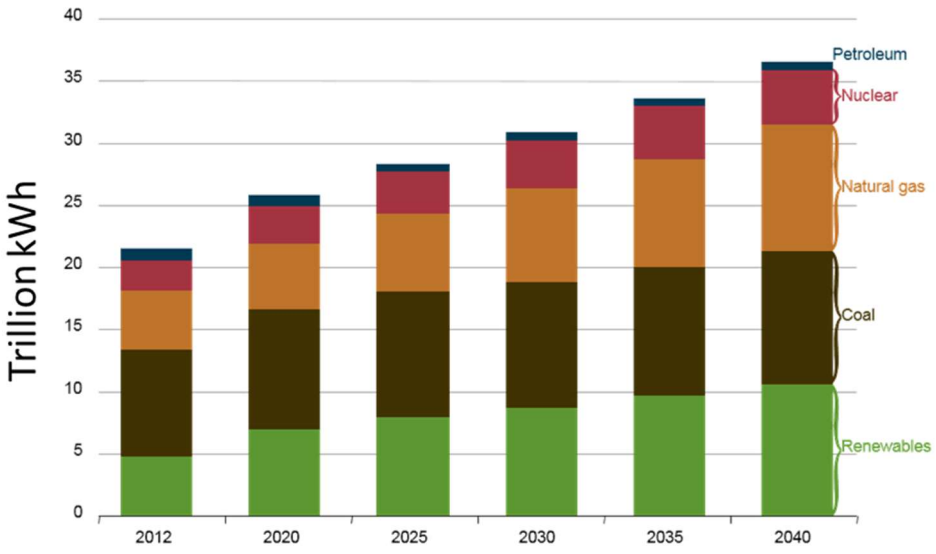

Figure 1-1 World net electricity generation by energy source [1].

This growth is driven by the imperative to address climate change and the pursuit of local economic development and community-owned energy [3]. Renewables can significantly reduce greenhouse gas emissions, be accessible in remote areas, and are replenishable. Of the renewable energy sources, both wind and solar photovoltaics (PV) are also becoming cost competitive with fossil fuels, with a levelized cost of energy (LCOE) of 0.06 $/kWh, 0.08 $/kWh, and 0.045 - 0.14 $/kWh respectively, and have seen yet another year of record growth in 2015 with an additional 50 GW of install capacity [3].

1.2 Solar Energy

The radiant energy from the sun is essential for determining the earth's temperature and for natural process on its surface. It is emitted by the sun as a result of nuclear fusion reactions. Even though the center of the sun reaches temperatures of 20,000,000 K, once the energy is reradiated through the photosphere, the spectrum of the sun's solar radiation is similar to that of a black body at a cooler 5800 K. The radiant power of the sun per unit area perpendicular to the sun outside of the earth's atmosphere but at the mean earth-sun distance is known as the solar constant or air mass zero (AM0) radiation. The accepted value of the solar constant is 1.353 kW m^{-2} [4]. The AM0 radiation spectral distribution differs from the ideal black body radiation as seen in Figure 1-2. Differences from the AM0 and black body spectral distributions arise from the varying transmissivity of the sun's atmosphere at different wavelengths [4].

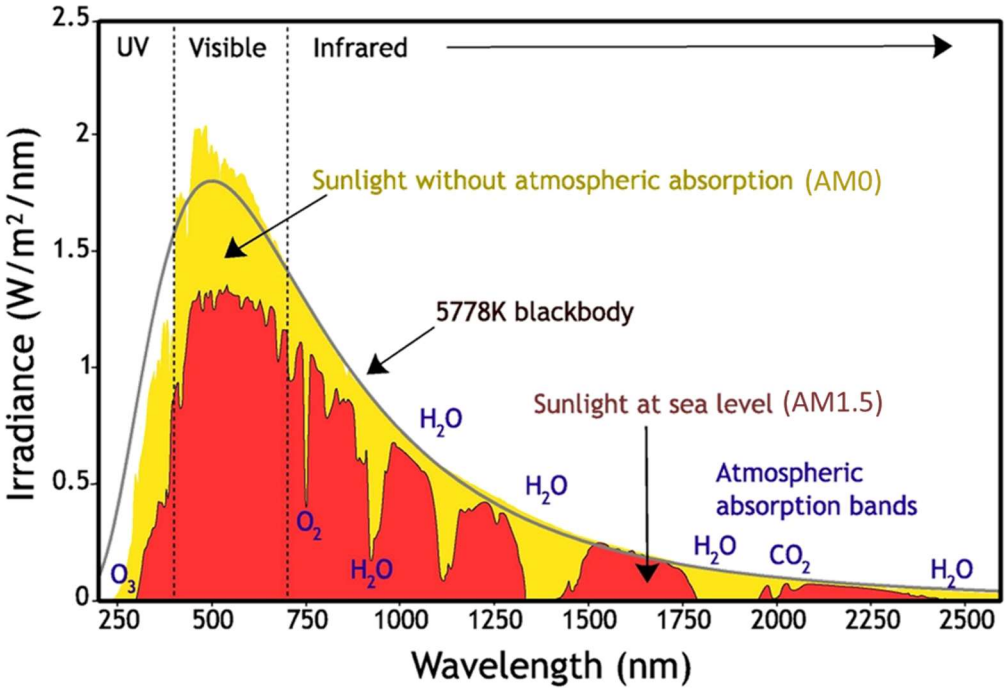

Figure 1-2 Solar radiation spectrum with showing blackbody radiation at 5778K, AM0, and AM1.5G.

Due to various scattering mechanisms and absorption by the atmosphere and its constituent gases, the sunlight is attenuated by at least 30% when it reaches the earth's surface. The amount of attenuation is highly variable and dependent on the length of the light path through the atmosphere. The ratio of the actual path to the minimum path is known as the optical air mass, and this length is shortest when the sun is directly overhead, air mass one (AM1). When the sun is at an angle of θ with respect to being directly overhead, the air mass is governed by (1-1:

$$Air\ mass = \frac{1}{\cos\theta} \tag{1-1}$$

In order to compare the performances of solar cells around the world, the most widely used standard is AM1.5 corresponding to an angle of 48.19°, shown in red in Figure 1-2, scaled up to produce a total power density of 100 mW cm^{-2}.

1.3 Photovoltaics

Solar PV is the world's fastest-growing form of renewable energy. Photovoltaic devices, or solar cells, directly convert incident solar radiation into electricity. The photovoltaic effect was first observed by Edmound Becquerel in 1839 while experimenting with an electrolytic cell consisting of two metal electrodes placed in an electricity-conducting solution [5, 6]. In 1877, in an effort to investigate the photoconductive effect in selenium, Adams and Day were the first to demonstrate the photovoltaic effect in an all solid-state system [7]. These findings were the foundation of solar cells, but it was not until 1954 that Daryl Chapin, Gerald Pearson, and Calvin Fuller at Bell Labs discovered a silicon-based p-n junction solar cell with a power conversion efficiency (PCE) of 6% [8]. Since this discovery, various solar cell technologies have emerged, implementing different semiconducting materials as photoactive layers.

The driving force behind the necessary transition to renewable energies is the harmful effect of fossil or nuclear energy byproducts have on our environment [9]. Photovoltaic devices are unique in their ability to convert sunlight directly into electricity without requiring rotating turbines to generate power or resulting in any greenhouse emissions. Paired with a method of energy storage, they can be designed and constructed as stand-alone off-grid systems generating power ranging from microwatts to megawatts. Although solar cells still suffer from the problem of having low PCEs, on the order of 20% for more

commonly produced silicon PV modules, they continue to be the fastest growing and most promising technology for electricity generation. PV technology has seen a growth rate from 2.6 GW of install capacity in 2004 to 227 GW in 2015 [3], an 87 fold increase. Currently, 93% of the PV market is accounted for by silicon based PV devices, but the cost, energy, and scarcity of materials [10] associated with their fabrication has resulted in the emergence of new PV technologies.

1.4 Current Solar Cell Technologies

There are currently many forms of photovoltaic device technologies at various stages of production or research phases. The most commonly deployed and commercially available technology is either single-crystal or multicrystalline silicon and inorganic thin film technologies. Still primarily in the research phase are the emerging PV technologies such as dye-sensitized, organic thin-film, and perovskite solar cells. This section will give a broad overview of these technologies. The highest recorded power conversion efficiencies as certified by the National Renewable Energy Laboratory are given in Figure 1-3.

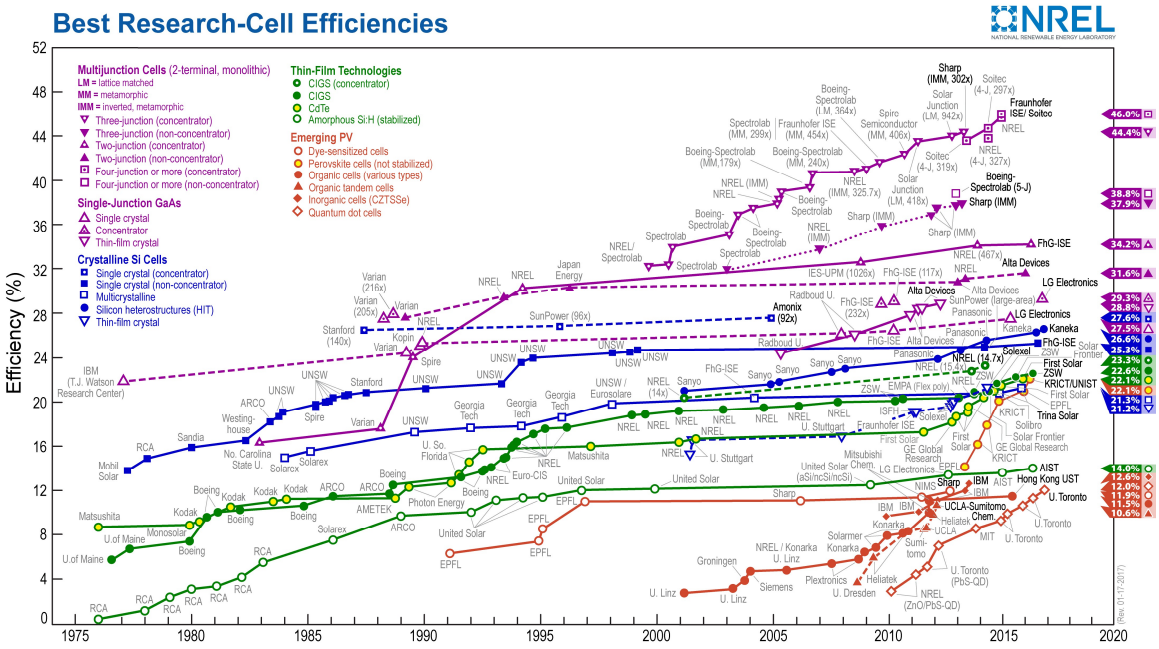

Figure 1-3 Highest power conversion efficiencies for various PV technologies (NREL January 17, 2017) [11].

1.4.1 Silicon-based Solar Cells

In the last few years, single crystal and multicrystalline silicon solar cells have achieved record high efficiencies of 25% and 21.3% respectively [11]. They have become the most developed PV technology, benefiting from the concentrated effort to understand how to process silicon for integrated circuit applications. Compared to other PV technologies, they have the advantage of using a photoactive absorber material that is stable, non-toxic, abundant, and well-understood [12].

Single crystal silicon PV devices are, as the name suggests, fabricated from a single continuous crystal structure. They are made through the Czochralski method, forming a solid crystal structure around a seed known as an ingot. After the seed is slowly drawn out of the molten silicon, it is finely sliced into wafers and made into a solar cell. Although

single crystal solar cells have higher power conversion efficiencies, the fabrication is costly and energy intensive.

Multi-crystalline PV devices are similarly processed from molten silicon, but instead of drawing the seed out, the silicon is allowed to cool in place. This process reduces the cost of producing silicon, but also forms more defects in the silicon causing additional recombination losses and a lower performance. The reduction in cost has outweighed the decrease in performance, and, currently, multi-crystalline PV modules account for 68% of the total commercial PV device production [13].

Silicon has an energy band gap of 1.12 eV, which is well matched to the solar spectrum. Since silicon has an indirect band gap, it is a weakly absorbing semiconducting material and therefore requires 10 times more material to absorb light than direct band gap semiconductors [14]. Since fabricating high purity silicon typically accounts for about 50% of the total PV module cost [10], other thin film technologies, such as $Cu(In,Ga)Se_2$, CdTe, and a-Si, using direct band gap semiconducting materials with higher absorption coefficients have emerged.

1.4.2 Inorganic Thin-Film Technologies

While silicon currently dominates the PV market, the remaining share of deployed solar cells are based on inorganic thin films. The absorption coefficients of various semiconducting materials used in PV devices in relation to crystalline silicon is shown in Figure 1-4.

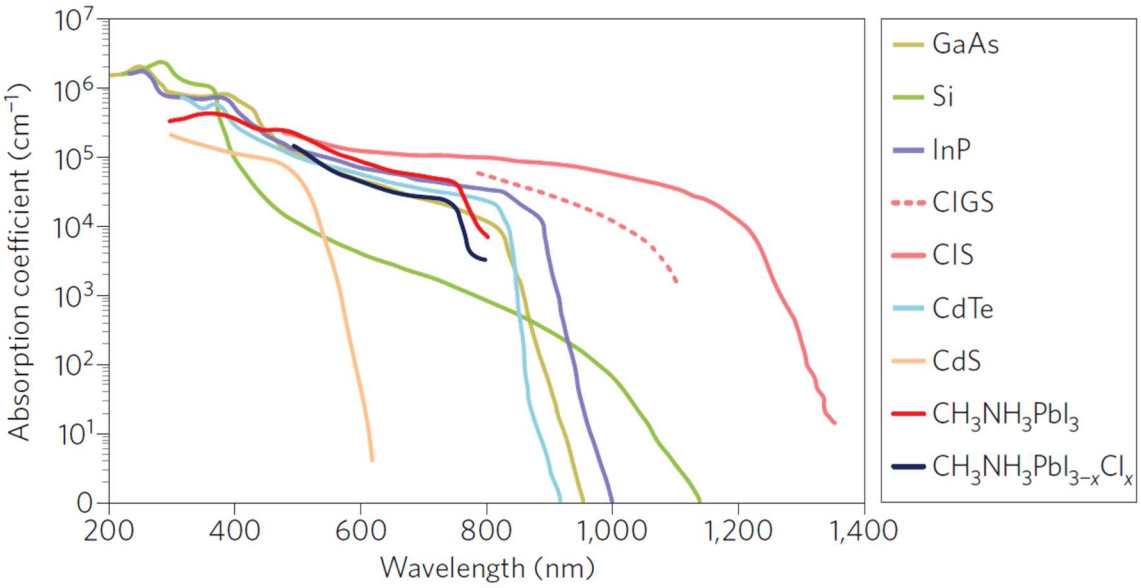

Figure 1-4 Absorption coefficients of semiconducting materials for PV applications [15].

Due to the strong absorption, thinner films, on the order of a few micrometers, of these semiconducting materials need to be deposited on substrates to absorb a significant amount of light. These thinner films have a higher tolerance for defects due to the shorter distances carriers need to travel and, therefore, can be processed at lower temperatures. While the amount of material required and low-temperature processing reduces the cost of thin-film PV devices, the power conversion efficiencies also decrease. The most common thin-film PV technologies, a-Si, CdTe, and CIGS (or $Cu(InGa)Se_2$), have certified efficiencies of 13.6%, 22.1%, and 22.3% respectively [11]. Still, there are concerns about the long-term applications of these technologies due to the scarcity and toxicity of some the materials used in their photoactive layers.

1.4.3 Emerging Technologies

Although still primarily in the research phase with only limited commercial availability, other PV technologies have emerged. These thin-film PV technologies use either organic light-absorbing semiconducting materials for organic solar cells (OSC) (or organic photovoltaics (OPV)) and dye sensitized solar cells (DSSC) or organic-inorganic hybrid materials, often lead-based, as seen in perovskite solar cells, which have gained a significant amount of attention in the last several years. While these types of cells still suffer from shorter lifetimes than silicon-based PV, the driving force behind these technologies is in the ease at which they can be processed often from solution with large areas and on flexible substrates through techniques such as blade coating, spray coating, printing, and slot-die coating. These techniques can often be done at low temperatures, reducing the thermal budget and cost associated with the solar-cell manufacturing [16].

1.4.3.1 Dye Sensitized Solar Cells

Dye sensitized solar cells, or Grätzel cells, were originally developed by Michael Grätzel and Brian O'Regan in 1988 at EPFL Lausanne, Switzerland [17]. DSSCs absorb light in an organic, inorganic, or metal-organic dye that is anchored to a mesoporous metal oxide layer, which acts as a photo-anode often developed from TiO_2 nanoparticles [18]. The absorption of light excites an electron within the dye molecule and injects it into the conduction band of the photo-anode. These electrons then travel through the external load and then to the counter electrode. The counter electrode typically consists of an iodide electrolyte coated over a conductive sheet, often platinum metal. To replace the lost electron, the I^- ion donates an electron to the dye and is then oxidized to I_3^-. Once the

electron passes through the load, it regenerates the I^- ion at the counter electrode. These types of cells have reached efficiencies of 11.9% [11].

The simple fabrication procedure and a performance close to that of amorphous silicon solar cells have brought attention to this emerging technology. While the materials used to manufacture DSSCs are lower in cost, the liquid electrolyte causes stability issues. Low temperatures could cause freezing of the electrolyte and therefore no power production as well as physical damage to the cell. At higher temperatures, the electrolyte expands and so the sealing of the panels must be robust. There is still an ongoing research effort to find alternatives by using solid electrolytes.

1.4.3.2 Perovskite Solar Cells

Interest in oganic-inorganic halide perovskite solar cells has surged, and this has led to their rapid development. Stemming from work on DSSC cells, perovskites were originally used as sensitizers by coating nanoporous TiO_2 surfaces in the seminal work of Miyasaka et al. in 2009 [19]. The breakthrough that caused the emergence of perovskite solar cells came in 2012, when Snaith et al. reported that using a mixed-halide $CH_3NH_3PbI_{3-x}Cl_x$ material exhibited better stability and carrier transport than just its pure iodide equivalent. Since 2012, the power conversion efficiency has grown from 10.9% to 22.1% [15, 20]. Snaith's et al. work in 2012 also demonstrated that the conducting TiO_2 can be replaced by non-conducting Al_2O_3, indicating that perovskites have a much broader impact on this new technology. Rather than just behaving as sensitizers, perovskites are also able to effectively transport electrons and holes to their respective electrodes [20]. Although this technology has shown potential for commercialization, its reliance on Pb as a key component of the

perovskite material is a concern due to its toxicity. Therefore, it may not be conducive for consumer applications. The robustness of this technology is also a major concern as they quickly degrade in the presence of moisture in the current state of advancement.

1.4.3.3 Organic Solar Cells

Organic solar cells, or OPV cells (hereon these two terms will be used interchangeably), are a category of solar cells consisting of solid-state organic semiconducting films placed between two electrodes, for hole- and electron-collection [21]. There are two main categories of organic solar cells based on the material composition of their photoactive layers, small molecule (smaller and well-defined molecular weight compounds) and polymer (materials with large and varying molecular weights containing repeating monomer units) solar cells. Polymer films are typically solution processed while small molecules can be either solution processed or, more often, thermally evaporated using vacuum deposition techniques. In this work, the focus will be exclusively on solution processed polymer solar cells.

When a photon is absorbed in the organic photoactive layers, power is generated within the cell in the form of a photocurrent and a photovoltage. Although OPV cells have some drawbacks, most notably their lower power conversion efficiencies and lifetimes, the technology is driven by short manufacturing times and a low thermal budget. Due to their tolerance of imperfections, polymer films and some small molecules can be processed at room temperature and are ideal candidates to print or coat large area devices onto flexible substrates using techniques such as roll-to-roll coating and other fast-process printing methods. Organic materials have high absorption coefficients on the order of 10^5 cm^{-1}, so

only a thin film of the photoactive layer (< 200 nm) is necessary to absorb a significant amount of light [22], leading to light-weight and cost-efficient photovoltaic devices.

As can be seen from Figure 1-3, organic PV devices have lower power conversion efficiencies at this stage than many of other PV technologies, only up to 11.5%. While the conversion efficiency is often used as the metric to evaluate the performance and potential usefulness of a technology or system, it does not take into account the large scale of the problem and the potential unavailability of elements or components. It also does not account for how much time is necessary for the device to produce the energy that was required in its making and constitution. This is referred to the energy payback time (EPBT).

1.5 Energy Payback Time

The EPBT addresses how quickly energy producing technologies pay back the energy spent making them. Energy payback time for the most widely available PV technology based on crystalline silicon is still on the order 1 – 2 years depending on the level of insolation [23]. Unlike silicon, organic photovoltaics have a clear advantage in their fast manufacturing speed and low thermal budget, and, therefore, their EPBT could potentially be reduced to just one day [23]. The EPBTs for some of the common PV technologies are shown in the Table 1-1.

Table 1-1 Energy payback times for common PV technologies [23].

Technology	EPBT (years)
Silicon mono- and polycrystalline	1.65-4.12
Amorphous silicon	1.13
GaAs	2.36-5

GaInP/GaAs	2.14-4.6
CdTe	0.73-1.61
CIS	2.02-2.26
OPV	0.2-4

1.6 Development of Organic Photovoltaics

1.6.1 Earliest Photovoltaic Technology

One of the first designs of a photocell for converting solar radiation into electrical power was created by Chapin, Fuller, and Pearson at Bell Laboratories in 1954 [8]. It was a demonstration of a silicon-based solar cell with a p-n junction, yielding a PCE of around 6%. The first generation of organic photovoltaic cells consisted of a single organic layer between two metal electrodes of different work functions. P-type organic layers and the low work function metal created a Schottky-barrier to which the rectifying behavior was attributed. These solar cells only achieved PCEs on the order of 0.1% and up to 0.7% [24, 25]. The next breakthrough came with the introduction of a bilayer structure of the photoactive layer in organic solar cells, having two layers of materials with an offset in energy levels. Tang demonstrated this bilayer structure in which excitons are generated in the photoactive materials, diffuse through the bulk to the interface of the two materials, and separate into free charge carriers, due to this energy offset providing the driving force for separation. The structure of this OPV device was ITO/CuPC/PV/Ag with an efficiency of around 1%.

1.6.2 Bulk Heterojunction Devices

In 1993, Sariciftci et al. reported the fabrication of a diode from a solution processed semiconducting polymer, a soluble derivative of poly(2-methoxy-5-(2-ethyl)-hexyloxy-p-phenylenevinylene) (MEH-PPV), and an evaporated fullerene, C_{60} [26]. The rectification ratios in the current-voltage characteristics exceeded 10^4. Although the PCE was reported of only 0.04% under 1 mW/cm^2 monochromatic illumination at 514.5 nm, this presented a major advance into solution-processed polymer solar cells. The primary limitation in bilayer organic solar cells comes from the short exciton diffusion length, and, therefore, these devices were inefficient at generating photocurrent. Either the excitons generated in the photoactive layers would recombine due to the short exciton diffusion length before reaching a donor-acceptor interface and dissociating, or the layers were too thin to absorb all of the incident photons. To rectify this problem a major breakthrough came with the introduction of bulk heterojunctions (BHJs) from the research group of Alan Heeger. Yu et al. used a blend of the semiconducting polymer MEH-PPV and the soluble fullerene derivative $PC_{61}BM$ to form the photoactive layer [27]. With this mix of polymer and fullerene domains, the distance an exciton travels to reach a donor-acceptor interface is minimized for more efficient dissociation. This also opened up a pathway for fabricating thicker photoactive layers with increased absorption.

Advances in materials and approaches to form interlayers have played a fundamental role in optimizing device performance and stability [28]. Simultaneously, over the last few decades, the effects of processing conditions such as processing solvents, additives, thermal annealing, drying times, etc. on morphologies and device performance parameters have been thoroughly studied [29-31]. Considerable progress has been made

leading to the demonstration of PCE values of around 10% in single bulk-heterojunction organic solar cells [32-35].

1.7 Objectives

The initial objective of this research is to tailor the electrical and optical properties of polymers used in the photoactive layer of OPV devices by introducing electrical dopants. Using dopants in organic semiconductors has always been problematic primarily due to the lack of spatial control, their potential to migrate, and the poorly understood mechanisms of charge transfer between the host and dopant. In inorganic semiconductors, a significant amount of control over the doping process is retained, whereby it can be limited to merely doping around the contact or further into a layer to induce differential doping. Therefore, it is imperative to understand how doping works in organic semiconductors in order to implement similar strategies and open up the possibility for new and more efficient device structures. We investigate how a simple post-process immersion procedure of polymer films in a strong oxidizing agent (phosphomolybdic acid) could drastically affect the film properties. An investigation of the penetration depth and spatial self-limitation is provided as well as some photo-oxidative stability studies.

The second objective of this research is to apply the methods of the initial studies on electrical doping to practical device applications. Focusing on organic photovoltaic devices, we investigate how the performance of the devices that have a directly electrically doped photoactive layer perform in comparison to our reference devices using separate thermally evaporated hole-collecting layers. Efficient charge collection at the corresponding electrodes is essential part of OPV device performance. An investigation into how we can reduce device geometry complexity while still maintaining efficient

charge collection was also conducted. The study focuses on incorporating charge generation and charge collection into a single layer sandwiched in between two conductive electrodes while maintaining the device performance. This could potentially reduce fabrication costs and thermal budget, thereby reducing the energy payback times. Device stability is also an essential key bring organic solar cells to become a commercial technology. Here we look into how devices with doped photoactive layers are affected under elevated temperatures for an extended amount of time, and whether the diffusion of the dopants could cause problems to the device stability. Furthermore, we investigate how this single-layer structure can be incorporated into one of the simplest multi-junction OPV devices.

1.8 Structure of Dissertation

In chapter 2, the fundamentals of organic semiconductors, semiconductor physics, and operating principles of organic solar cells will be discussed. An overview will be given of the relevant metrics, necessary energy levels, and structure of organic solar cells. The role of interlayers and electrical doping in OPV devices will also be introduced.

Chapter 3 will cover all of the materials and fabrication procedures used to for solar cells with various device architecture. It will also give a brief overview of the equipment used for characterization of the polymer films and OPV devices.

Chapter 4 details the use of dopants in donor polymer films, and characterizes the chemical, electrical, and optical properties of the doped films. The wide applicability to a wide range of organic semiconducting materials will also be shown using a novel and simple doping technique.

Chapter 5 explains how the new method described in chapter 4 is implemented in OPV devices. Various simplified device architectures are introduced and compared with reference devices. The stability of the devices is also investigated.

Chapter 6 will present the conclusion of this work as well as some future directions, which can be further explored.

CHAPTER 2

Background of Organic Solar Cells

The physics that govern the operation of an organic solar cell are complex involving concepts from optics, semiconductor physics, and organic chemistry. This section will provide the necessary technical details about the physics of organic semiconductors, operating principles of organic solar cells, and electrical doping of organic semiconductors.

2.1 Organic Semiconductors

Organic semiconducting materials are the foundation of OPV technology. In the context of OPVs, the focus is primarily on two categories of organic semiconductors with distinct differences, either small molecules or polymers with a system of alternating single- and double-bonds between carbon atoms. Polymers are constituted by repetition of a fundamental unit, a monomer. They have large molecular weights, are soluble in organic solvents, and have good film-forming properties, therefore can be coated from a liquid state by means of spin-coating or other similar processes. Although some small molecules have larger molecular weights and with some structural modifications may be similarly solution processed, they are primarily insoluble in organic solvents due to their low molecular weights and are deposited via thermal evaporation. Just as in inorganic semiconductors, these carbon-based materials can also be used to fabricate solid-state devices such as organic light-emitting diodes, organic field-effect transistors (OFETs), and organic photovoltaics. Organic semiconductors offer unique advantages over their inorganic counterparts such as the ability to finely tune their electrical and optical properties through modification of their chemical structures.

2.1.1 Atomic Orbitals

The time dependent Schrödinger equation can be solved for the wavefunction ($\boldsymbol{\Psi}$) using Eq. (2-1):

$$i\hbar\frac{\partial}{\partial t}\boldsymbol{\Psi}(\boldsymbol{r},t) = \hat{\boldsymbol{H}}\boldsymbol{\Psi}(\boldsymbol{r},t) \tag{2-1}$$

Here i is the imaginary number, $\hbar$ is the reduced Planck's constant, and $\hat{\boldsymbol{H}}$ is the Hamiltonian operator. This wave equation describes the total energy of a hydrogen atom. The wavefunction corresponds to an allowed energy level for an electron, since the electron can only exist at discrete energy levels. From the wavefunctions, atomic orbitals can be mathematically generated centered around the nucleus of the atom.

In organics, the more commonly encountered elements are from the first and second row (H, C, N, and O), so the discussion here will be primarily limited to atomic orbitals utilized by these elements which are: 1*s* orbital, 2*s* orbital, and 2*p* orbital. The symmetric spherical shapes of the *s* orbitals and the dumbbell shaped degenerate *p* orbitals are shown in Figure 2-1.

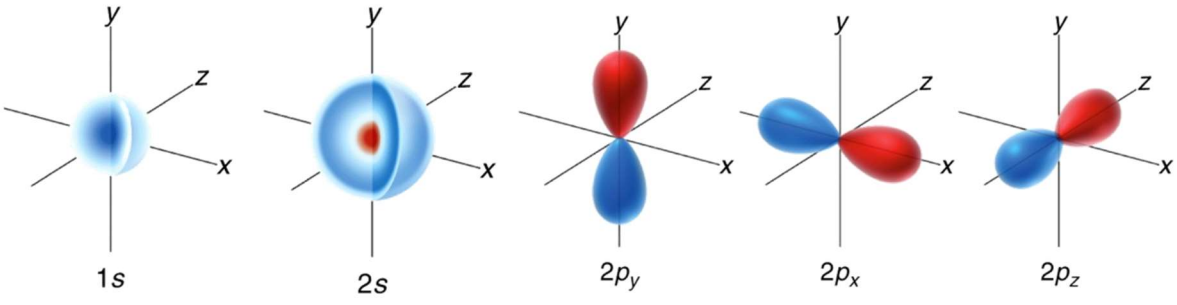

Figure 2-1 Illustration of *s* and *p* orbitals [36].

By the Aufbau principle, Pauli exclusion principle, and Hund's rule, electrons fill the lowest energy orbitals first, a maximum of two electrons can occupy an orbital that have opposite spin, and when filling atomic orbitals with the same energy, degenerate orbitals such as p orbitals, an electron is placed in each orbital first before being paired up [36]. This can be seen in the example for a carbon atom with an atomic number of 6 in Figure 2-2.

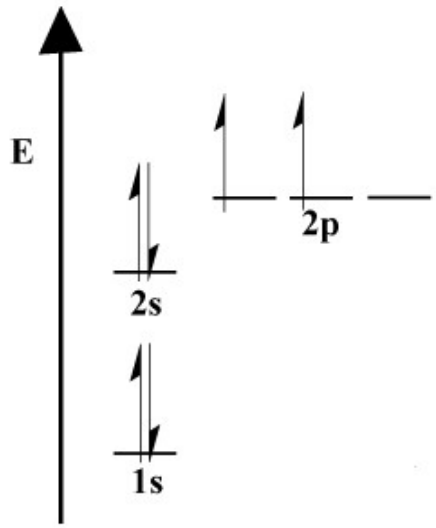

Figure 2-2 Atomic orbitals of a carbon atom [36].

2.1.2 Molecular Orbitals

When atomic orbitals overlap, they have constructive or destructive interference. When the atomic orbitals have constructive interference, the overlap forms strong covalent bonds. The atomic orbital overlap is often described using a linear combination of atomic orbitals (LCAO). This mathematical method combines atomic orbitals to form molecular orbitals (MOs), which are associated with the entire molecule and are filled in much the same way as those of an individual atom.

2.1.2.1 sp^3 Hybridization

A carbon atom has four valence electrons in its 2*s* and 2*p* atomic orbitals. When the carbon atom forms four single bonds as in the case of methane (CH_4), the carbon is thought to be in an excited state where an electron in the 2*s* orbital is promoted to the 2*p* orbital. This provides carbon with the four atomic orbitals containing an unpaired electron necessary to form bonds. To explain the larger bonding angles in the methane molecule, the 2*s* and 2*p* orbitals are mathematically averaged or hybridized to from four degenerate sp^3-hybridized orbitals. These sp^3 orbitals form strong σ bonds with the *s* orbitals of the hydrogen atoms.

2.1.2.2 sp^2 Hybridization

Organic semiconductors contain hydrocarbon chains with alternating single and double bonds. When a carbon containing compound forms a double bond, it only needs to bond to three atoms instead of four. Therefore, it only requires three hybridized orbitals formed by mixing the *s* and two of the *p* orbitals as shown for the simple case of an ethylene molecule (C_2H_4) in Figure 2-3, referred to as sp^2 hybridization.

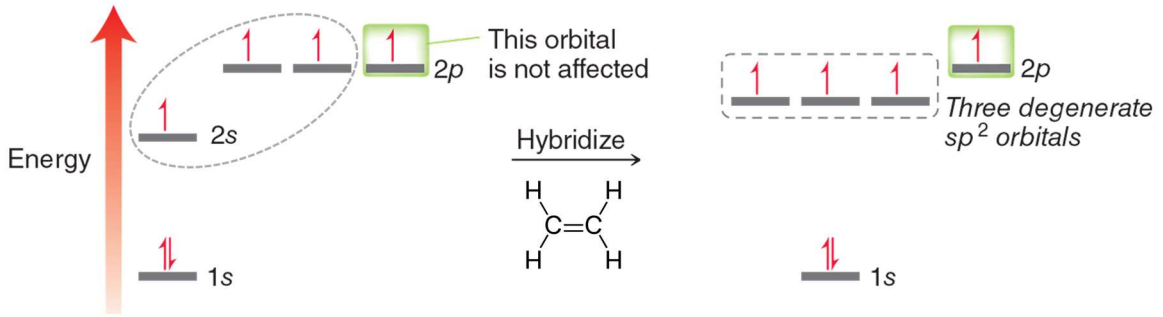

Figure 2-3 sp^2 hybridization of a carbon atom. Figure adapted from [36].

The p_z orbital remains unhybridized. While the three sp^2-hybridized orbitals form σ bonds with the carbon and hydrogen atoms, the unhybridized p_z orbitals perpendicular to the σ bonded orbitals between adjacent carbon atoms overlap forming a π bond or a π^* anti-bond and a share highly delocalized π electrons across this group of atoms, known as conjugation. The bonding molecular orbital is formed when the wave functions of the individual atomic orbitals are added and is energetically favorable since its energy is lower than that of the isolated atomic orbitals. The anti-bonding molecular orbital is formed when the wave functions of the atomic orbitals are subtracted and is energetically unfavorable since the energy is higher than that of the isolated atomic orbitals. These two bonding interactions (σ and π) comprise the double bond. A simple example of π bonding in ethylene is shown in Figure 2-4.

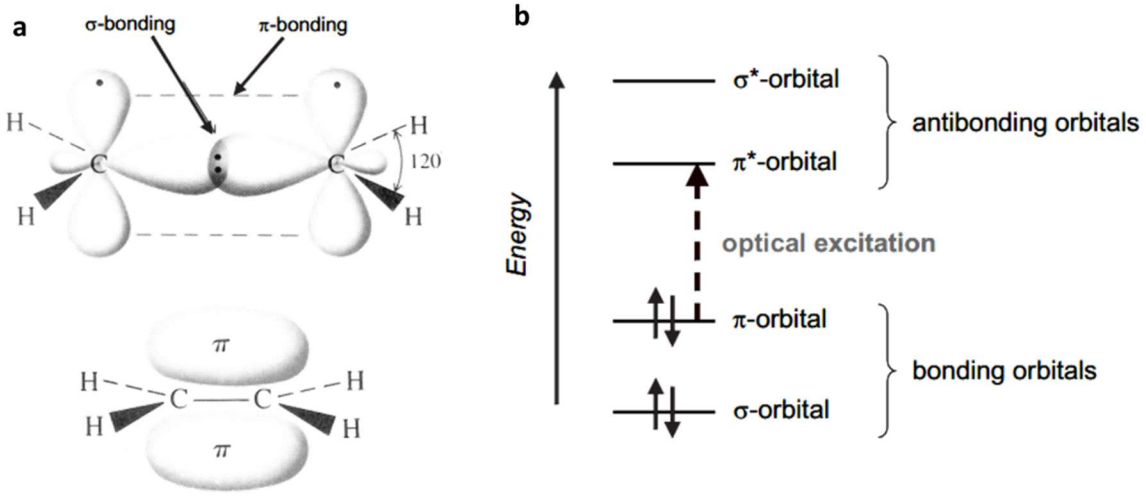

Figure 2-4. a, σ and π bonds in the conjugated π electron system of ethylene. **b,** Lowest electronic excitation between the π and π^* orbitals.

Hence, the lowest electronic excitations of the conjugated molecules are the π-π^* transitions with energy gaps ranging between 1.5 eV and 3 eV. This energy gap leads to light absorption or emission in OPV photoactive layers or OLED light-emitting layers respectively in the visible spectral range. The delocalization of π electrons in a conjugated system is shown in the example for a 1,3 – butadiene molecule in Figure 2-5.

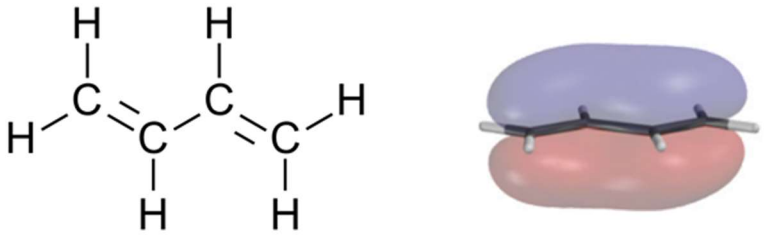

Figure 2-5 Delocalized π electrons in a 1,3 – butadiene molecule with four carbon atoms. Adapted from [37].

Highly conjugated compounds have more molecular orbitals and smaller energy gaps in between them. Therefore, systems exhibiting a greater extent of conjugation require less energy to excite an electron to a higher energy level. This extends the maximum wavelength at which the compound absorbs or emits light.

2.1.3 Frontier Orbitals

The π bonding molecular orbital and the π^* anti-bonding molecular orbital form what are known as the frontier orbitals. The highest energy π bonding molecular orbital is referred to as the highest occupied molecular orbital (HOMO) and the lowest energy π^* anti-bonding molecular orbital is referred to as the lowest unoccupied molecular orbital (LUMO). Together, the HOMO and LUMO are known as the frontier orbitals. These energy levels are of the most interest since the electrons in the HOMO are weakly held and are the ones that are transferred from a molecule. When electrons are transferred to a

molecule, they go into the LUMO since it is the lowest energy orbital available. The σ electrons are not explicitly considered since they are strongly held together [37].

Molecular orbitals correspond to one-electron wavefunctions and therefore can be computationally calculated, including the ones of special interest, the HOMO and LUMO. However, what is measured experimentally upon excitation is the difference between the N-electron ground state and the N ± 1-electron excited state [38].These differences in experimentally measured energies are known as the ionization potential (IP) and electron affinity (EA). The IP is the minimum energy required to create a positive charge carrier, and the EA is the energy gained by adding a negative charge carrier, which are often used as close approximations to the HOMO and LUMO respectively.

In the case of a single molecule, the energy difference between the IP and EA is defined as the fundamental gap, E_{fund}:

$$E_{fund} = IP - EA \tag{2-2}$$

This quantity is experimentally determined by a combination of gas-phase ultraviolet photoelectron spectroscopy and electron attachment spectroscopy. Again, it is important to note that the computationally calculated HOMO-LUMO gap is different and only a close approximation to E_{fund}.

The optical gap (E_{opt}) in a molecule is the lowest electronic transition possible at the onset of absorption of a single photon, where E_{opt} is substantially smaller than E_{fund}. Since in the excited state the electron and hole are electrostatically bound, the difference between E_{fund} and E_{opt} is accounted for by the binding energy of the electron-hole pair (E_B) [38], defined by:

$$E_B = E_{fund} - E_{opt} \tag{2-3}$$

Contrary to single molecules, in polymeric or bulk materials the intermolecular interactions broaden the molecular energy levels into electronic bands [38]. These bands are referred to as the HOMO bands and LUMO bands in organic semiconducting materials, analogous to the valence and conduction bands in inorganic semiconductors respectively. The widths of these bands are dependent on the electronic coupling between adjacent molecules and disorder. Here we define the top of the HOMO band as the IP and the bottom of the LUMO band as the EA. The energy difference between the EA and IP is known as the band gap or transport gap in the bulk materials case. It is important to note that the E_{trans} is not equal to and in general smaller than E_{fund} in the single molecule case.

2.1.4 Excitons

When light is absorbed in organic semiconducting materials, an exciton is generated. Excitons are Coulombically bound electron-hole pairs. In inorganic semiconductors Wannier-Mott excitons are generated having binding energies of only a few meV (9.3 meV for Si [39]), and, therefore, room temperature thermal energy (k_BT~ 0.026 eV) is sufficient to quickly dissociate the exciton into free charge carriers. On the other hand, organic semiconductors have low dielectric constants (ε_r ~ 3 – 4) and substantial electron-electron and electron-vibration interactions [38]. Therefore, Frenkel excitons are generated with binding energies that are an order of magnitude larger than their inorganic counterparts, varying from 0.2 to 1.5 eV [40, 41]. The binding energy is described by:

$$E_B = \frac{e^2}{4\pi R \varepsilon_0 \varepsilon_r} \tag{2-4}$$

where e is the charge of the electron, ε_0 is the permittivity of vacuum, ε_r is the dielectric constant of the medium, and R is the electron-hole separation distance. Since excitons have such a high binding energy in organic semiconductors, OPV devices must have a driving force to dissociate them into free charge carriers.

Different electron affinities and ionization potentials in the materials comprising the absorber or photoactive layer create an electronic asymmetry, which provides the necessary driving force for exciton dissociation OPV devices. The photoactive layer contains an electron-rich material that is "donor-like", a small molecule or conjugated polymer, with a small IP that behaves as the hole-transport material. It also contains an electron-poor material that is "acceptor-like", primarily a fullerene derivative, although recent progress has been made using non-fullerene acceptors [42], with a large EA that behaves as an electron-transport material. Hereon we will refer to these materials as donors and acceptors. The energy level diagram for a typical OPV device as well as common donor and acceptor materials is shown in Figure 2-6.

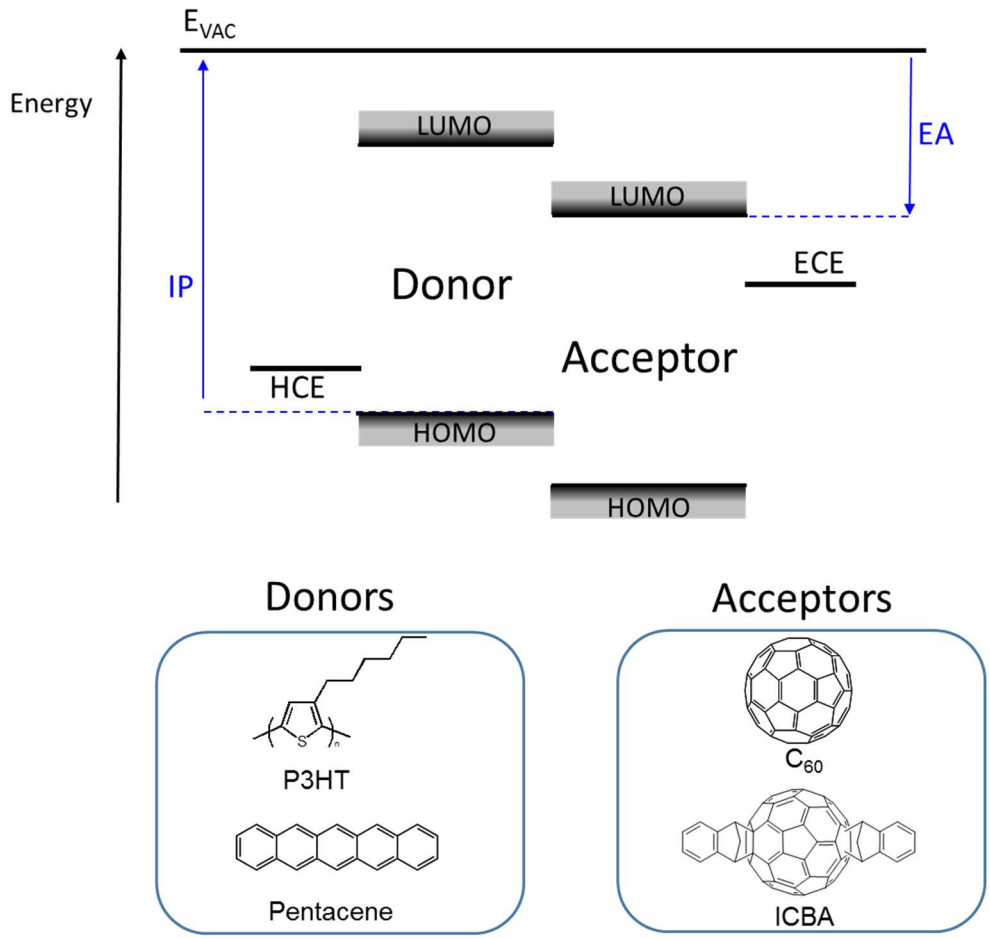

Figure 2-6 Energy level diagram of an OPV device showing the energy offset between the donor and acceptor. The bottom of the figure shows some common small molecule and polymer materials for the donor, and fullerene and fullerene-derivatives for the acceptor. HCE refers to the hole-collecting electrode, and ECE refers to the electron-collecting electrode.

Acceptors must have higher EAs than donors to be energetically favorable for electron transfer by having a large enough EA difference between the donor and acceptor acting as the driving force to overcome the binding energy of an exciton generated in the donor.

2.2 Semiconductor Physics

2.2.1 Fermi Level Energy at Equilibrium

The Fermi level energy is the average energy, and can be considered as the electrochemical potential, of a particle that is part of a system in thermal equilibrium. Thermal equilibrium is defined by a balanced system in which no energy is exchanged between parts of the system or between the system and its environment. For a non-degenerate semiconductor, this energy level is positioned somewhere in the band gap of the semiconductor where there is no density of states. The Fermi-Dirac distribution function describes the probability of occupancy of allowed energy levels by electrons at thermal equilibrium as follows:

$$f(E) = \frac{1}{1+e^{(E-E_F)/k_BT}} \tag{2-5}$$

where T is the temperature of the system, E_F is the Fermi level energy, and k_B is the Boltzmann constant. Under equilibrium, the Fermi level energy is flat across the entire semiconductor. For non-degenerate semiconductors (2-5) can be further simplified to:

$$f(E) = \frac{1}{1+e^{(E-E_F)/k_BT}} \cong e^{(E_F-E)/k_BT} \tag{2-6}$$

where the approximation holds when $(E - E_F) > 3k_BT$. Using this approximated distribution, an expression for the density of electrons and holes in a non-degenerate semiconductor at thermal equilibrium can be derived:

$$n_0 = N_C e^{(E_F-E_C)/k_BT} \tag{2-7}$$

$$p_0 = N_V e^{(E_V-E_F)/k_BT} \tag{2-8}$$

where n_0 (p_0) is the electron (hole) density, N_C (N_V) is the effective density of states per unit volume in the conduction (valence) or LUMO (HOMO) band, and E_C (E_V) is the energy at the bottom (top) of the conduction (valence) or LUMO (HOMO) band. Form these expressions we can calculate the density of electrons or holes given a Fermi level energy and effective density of states and vice versa.

2.2.2 Quasi-Fermi Level Energies

When an external perturbation is applied to a system causing non-equilibrium conditions, carrier densities may still be calculated using a Fermi-Dirac distribution but with different Fermi level energies, if the condition is close to equilibrium. Such perturbations include either an applied bias or illumination of the semiconductor and result in the system being in quasi-equilibrium. The total electron and hole densities are given by:

$$n = n_0 + \Delta n = n_i e^{(F_n - E_i)/k_B T} \tag{2-9}$$

$$p = p_0 + \Delta p = p_i e^{(E_i - F_p)/k_B T} \tag{2-10}$$

where F_n (F_p) is the quasi-Fermi level energy for electrons (holes) and n_i (p_i) is the intrinsic electron (hole) density, which can be derived from Eqs. (2-7) and (2-8) when $E_f = E_i$ (the intrinsic Fermi level energy). It is often convenient to express the equations for the quasi-Fermi level energies explicitly by substituting the carrier densities from Eqs. (2-7) and (2-8) for an intrinsic semiconductor into Eqs. (2-9) and (2-10):

$$F_n = E_C + k_B T \ln\left(\frac{n}{N_C}\right) \tag{2-11}$$

$$F_p = E_V - k_B T \ln\left(\frac{p}{N_V}\right) \tag{2-12}$$

2.2.3 Carrier Transport

Another important aspect of solar cell operation is the transport of carriers to their respective electrodes. The driving force behind the dissociation of an exciton into free charge carrier will be discussed in a later section. The two processes of carrier transport are due to an applied electric field, referred to as drift, and the other is due to a carrier density gradient, referred to as diffusion.

An electron travels in a straight path until it is influenced by a scattering mechanism that changes its direction and velocity. When a uniform electric field is applied to a semiconductor, electrons drift at a constant velocity in the direction proportional and opposite to the electric field. This proportionality constant is known as the mobility μ measured in units of cm^2/Vs:

$$\mu = \frac{e\tau_c}{m^*} \tag{2-13}$$

where τ_c the average time between collisions and m^* is the effective mass. From this a simplified one dimensional drift current density for electrons and holes can be written as:

$$J_{drift,n} = en\mu_e E \tag{2-14}$$

$$J_{drift,p} = ep\mu_h E \tag{2-15}$$

where E is the electric field.

The carrier diffusion process acts to even out carrier density variations, and, therefore carriers will diffuse from areas of high carrier density to low carrier density. This redistribution of carriers results in a diffusion current given by the simplified one dimensional expression for electron and hole diffusion current density:

$$J_{diffusion,n} = eD_e \frac{dn}{dx} \tag{2-16}$$

$$J_{diffusion,p} = -eD_h \frac{dp}{dx} \tag{2-17}$$

where D_e (D_h) is the diffusion coefficient for electrons (holes).

Combining both the drift and diffusion current densities yields the total current density:

$$J_{total,n} = en\mu_e E + eD_e \frac{dn}{dx} = n\mu_e \frac{dF_n}{dx} \tag{2-18}$$

$$J_{total,p} = ep\mu_h E - eD_h \frac{dp}{dx} = p\mu_h \frac{dF_p}{dx} \tag{2-19}$$

2.3 Operating Principles of Solar Cells

2.3.1 Electrical Characterization and Performance Parameters

Solar cells produce photo-generated current and voltage from which power is generated ($P = IV$). Figure 2-7 depicts the typical operation of a solar cell under illumination.

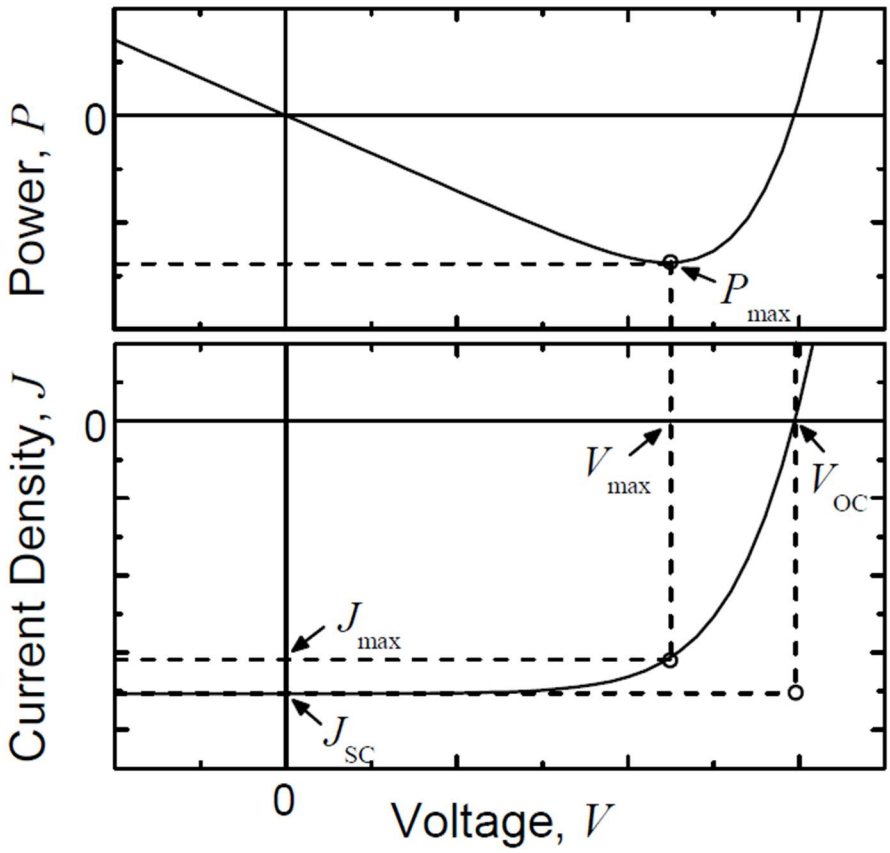

Figure 2-7 *J-V* and *P-V* curves of an OPV device under illumination.

Here we can see that the solar cell produces power in the fourth or PV quadrant as is indicated in the power versus voltage graph where a negative power indicates power generated. This places the focus on four main parameters used to characterize the performance of a solar cell: the short-circuit current density (J_{SC}), open-circuit voltage (V_{OC}), the fill factor (*FF*), and the power conversion efficiency (PCE).

2.3.1.1 Short-Circuit Current Density

J_{SC} is the current that flows through the external circuit when there is no applied bias and the electrodes of the solar cells are short circuited. It is the maximum current the solar cell can deliver and is strongly dependent on the optical properties of the solar cell. For an ideal case, the *Jsc* is identical to the photocurrent density (J_{ph}). However, deviations from the ideal case may arise due to parasitic effects. Since $V = 0$ at this point, no power is generated by the solar cell.

2.3.1.2 Open-Circuit Voltage

V_{OC} is the voltage across the solar cell when there is no current flow through the device, or the device is open circuited. Since $J = 0$ at this point, no power is generated by the solar cell. It is the maximum voltage a solar cell can deliver and corresponds to the forward bias point at which the dark current density compensates the photocurrent density.

2.3.1.3 Fill Factor

FF is defined as the ratio of the maximum power point ($P_{max} = V_{MPP} \times J_{MPP}$) of a solar cell to the product of the V_{OC} and J_{SC}:

$$FF = \frac{V_{MPP} \times J_{MPP}}{V_{OC} \times Jsc} \tag{2-20}$$

Although a large fill factor is desirable, parasitic resistances and recombination losses often result in lower FFs.

2.3.1.4 Power Conversion Efficiency

The key metric for solar cell performance is the PCE, or the ratio of the maximal generated electrical power to the incident optical power. For consistency across all PV devices, a standard optical power of 1 sun or 100 mW/cm^2 with an AM1.5G spectrum shown in Figure 1-2 is used for the measurements. The PCE is affected by changes in all of the previously mentioned metrics J_{SC}, V_{OC}, and FF and is defined as:

$$PCE = \frac{P_{out}}{P_{in}} = \frac{V_{OC} \times J_{SC} \times FF}{P_{in}} \times 100\% \tag{2-21}$$

2.3.2 Design of Organic Solar Cells

In general, OPV cells have one of two types of architectures depicted in Figure 2-8, conventional or inverted. Both structures have at least one semi-transparent electrode to allow photon penetration and absorption into the photoactive layer and two charge extraction layers on either side to tailor the work function (WF) for efficient charge collection, with the only difference being which sides collect carriers i.e., bottom electrode collects holes (inverted) or collects electrons (conventional). Here it is important to note that efficient collection of carriers is a critical aspect for performance of any photovoltaic device. The importance of having electrodes with contrasting WF values, high and low, will be highlighted in the next section on solar cell operation.

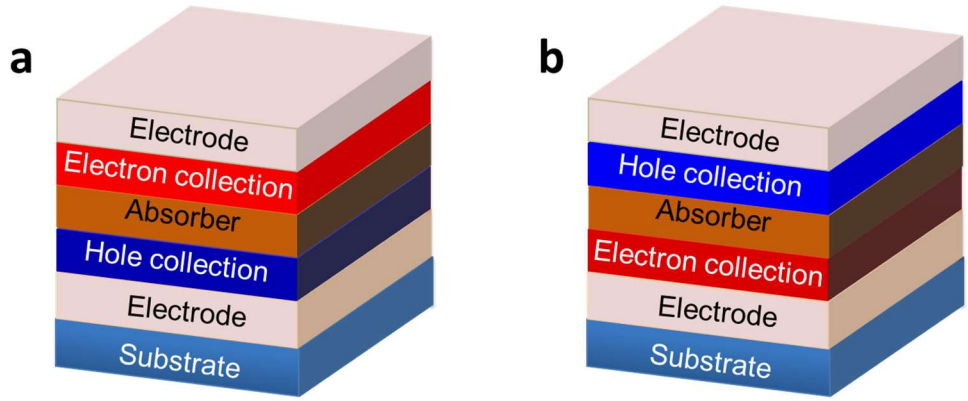

Figure 2-8 a, Conventional and **b,** inverted architecture of organic solar cells.

The most commonly used substrate is glass due its 90% transmittance of wavelengths in the visible and infrared range, corresponding to the wavelengths of the solar spectrum. Although glass simplifies the fabrication of OPV devices, its rigidity does not lend to applications such as electronic skin, textiles, and surface conforming and wearable electronics. Since OPVs require only thin-films to absorb a significant amount of light and are mechanically resilient, they have also been shown to be fabricated on plastic, such as polyethylene terephthalate (PET) or polyethylene naphthalate (PEN), and other semi-transparent flexible substrates [43].

Another key aspect for optimal OPV device performance is in the correct choice of electrodes to efficiently extract free charge carriers. In inorganic solar cells, the most common approach is to use differential doping in order to create Ohmic contacts. Since controlled doping is difficult in organic semiconductors, a different approach is taken by using electrodes with a high and low WF. The approach taken with many organic solar cells is to use charge-extracting interlayers on either side of the photoactive layer, but, as will be seen in a later section, our recent work shows that this is not always necessary. In fact, limited electrical doping in polymer films is indeed possible for organic solar cells

[44]. A few examples of these interlayers include either low WF metals (e.g. Ca, Ba, Mg) and metal oxides (e.g. ZnO), high and low WF polymer layers (e.g. PEDOT:PSS, PEIE), or independently doped polymer films. The electrodes also have to have a high conductivity and are therefore often capped with a metal or a conductive polymer to extract charges to the external leads. One of these electrodes must be semi-transparent to allow incident light to pass through the device, while it is desirable for the other electrode to be highly reflective. Light that is not absorbed in the first pass through the photoactive layer will then be reflected off of the back electrode to make a second pass.

Photoactive layers are in organic solar cells can be designed in several different ways. In thermally evaporated small molecule solar a cells, a commonly employed structure is a planar-mixed heterojunction, where a mixed donor-acceptor layer is deposited in between two homogenous layers of donor and acceptor materials [45]. For photoactive layers in solution processed polymer solar cells, a BHJ is used, where the donor and acceptors are mixed to create a single blended layer with many interfaces. The BHJ is a three-phase system with aggregated donor and acceptor domains in addition to mixed amorphous regions. The bulk heterojunction photoactive layer is shown in Figure 2-9.

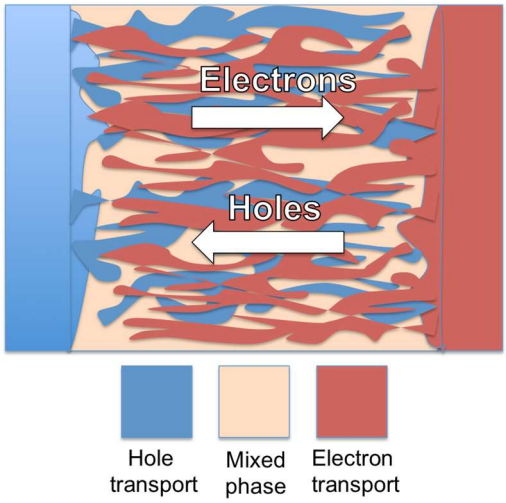

Figure 2-9 Bulk heterojunction photoactive layer.

To dissociate excitons generated in the photoactive layer, the exciton must reach a donor-acceptor interface at which the offset in energy levels provides the driving force needed in order to create free charge carriers. The thickness of the photoactive layer therefore has to be on the same scale as the exciton diffusion length ($L = \sqrt{D\tau}$, where D is the diffusion coefficient and τ is the lifetime of the exciton), around 10 nm for organic semiconducting materials [46, 47]. With such a short exciton diffusion length, a compromise has to be reached, either sacrificing sun light absorption due to a thin photoactive layer or introducing losses into the OPV device due to the recombination of excitons. To mitigate this problem, the BHJ uses a blend of donor and acceptor materials to reduce the distance an exciton needs to travel before reaching a donor-acceptor interface. The morphology of a photoactive layer blend is highly variable and is affected by processing parameters including choice of solvent, donor/acceptor concentrations, thermal annealing times and temperatures, solvent annealing conditions, additives, and interlayer surface energies, and it is still an extremely active topic of research. In general, a BHJ photoactive layer will have an interpenetrating network of donor and acceptor materials with domain sizes on the order of the exciton diffusion length for efficient exciton dissociation, while maintaining continuous charge transport pathways to the electrodes [46].

2.3.3 Operation of Organic Solar Cells

Although the exact details of the operation of organic solar cells is still under debate, it can generally be broken down into several steps. When a photon with an energy greater

than the optical gap, defined as the lowest optical transition in a π-conjugated organic material, is absorbed in the photoactive layer, an exciton is created. The difference between E_{trans} and E_{opt} lies in the exciton binding energy. In order for an exciton to overcome the binding energy and dissociate into free charge carriers, it must reach a donor-acceptor (D-A) interface. The behavior of the exciton at this interface is still a topic of research with no consensus of exactly how the dissociation occurs. The most common explanation is that the exciton becomes a weakly Coulombically bound polaron pair in the charge transfer (CT) state at the D-A interface, where it either recombines or is finally dissociated into a charge separated (CS) state [48]. How the additional energy states, energy transfer, and rates of the processes that occur at this interface influence device performance is still not fully understood.

To insure that charges are swept in opposing directions to their corresponding electrodes, a PV device has to have electronic asymmetry. In crystalline silicon solar cells this asymmetry is achieved by having *n* and *p*-doped regions, combined to form a *pn*-junction. After the *n* and *p* regions come into contact, the junction reaches thermal equilibrium and Fermi level is flat across the entire device, which forms a built-in electric potential (φ_{bi}). This φ_{bi} creates a selective junction whereby electrons entering the junction will flow towards the *n*-doped region, while holes have difficulty overcoming this potential energy barrier and instead flow towards the *p*-doped region. Analogous to crystalline silicon solar cells, organic solar cells achieve asymmetry by using donor and acceptor materials to separate charges and also by using electrodes with contrasting WF values. This asymmetry is illustrated in Figure 2-10, where only the relevant energy levels are shown,

the LUMO of the acceptor ($LUMO_A$) and the HOMO of the donor ($HOMO_D$) of the photoactive layer and the WFs of the two electrodes before making contact.

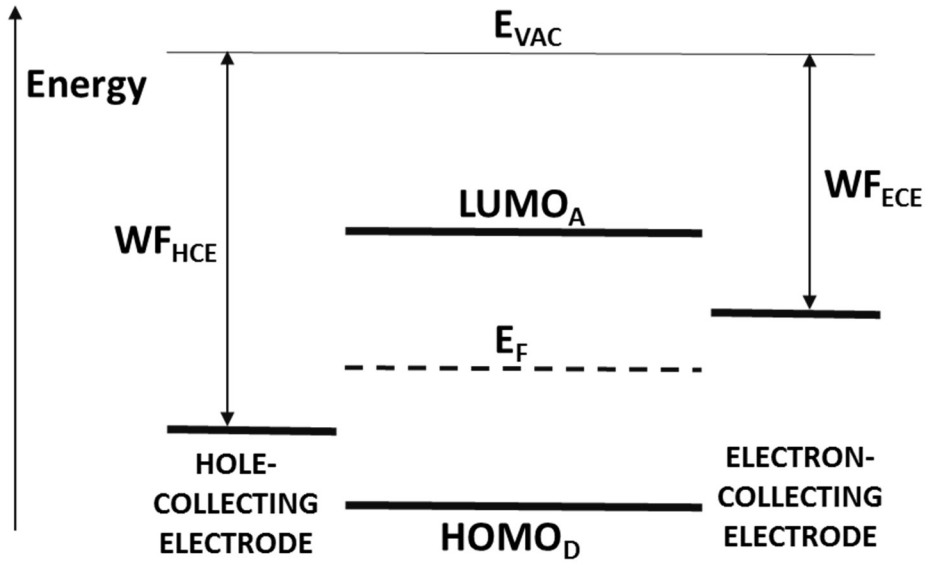

Figure 2-10 Energy level diagram of the layers of an OPV device before making contact.

Firstly, the energy offset between the hole-transport material (donor) and electron-transport material (acceptor) materials provides the driving force to separate the exciton into free charge carriers that proceed to accumulate in their respective transport materials. Second, electrodes are used which have WFs that are larger or smaller than the E_F of the donor or acceptor respectively. As is in the case of crystalline silicon solar cells, this creates a built-in electric potential φ_{bi} ($e\varphi_{bi} = WF_{HCE} - WF_{ECE}$) after the electrodes make contact with the photoactive layer in OPV devices as seen in Figure 2-11.

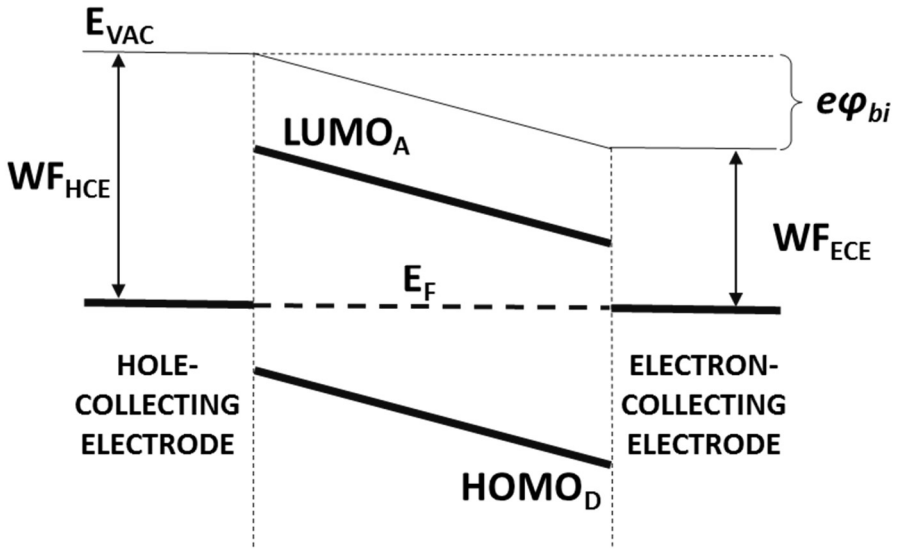

Figure 2-11 Energy level diagram of an OPV device after the electrodes make contact with the photoactive layer.

Under illumination the OPV device is no longer in equilibrium, leading to an accumulation of carriers at both photoactive layer/electrode interfaces. This inhomogeneous spatial distribution of charge carriers results in a splitting of the hole and electron quasi-Fermi level energies. The difference in quasi-Fermi level energies at the electrodes produces the photovoltage (V_{ph}):

$$eV_{ph} = F_n(x = d) - F_p(x = 0) \tag{2-22}$$

where d is the thickness of the photoactive layer. Figure 2-12 shows the energy levels of an OPV device under illumination.

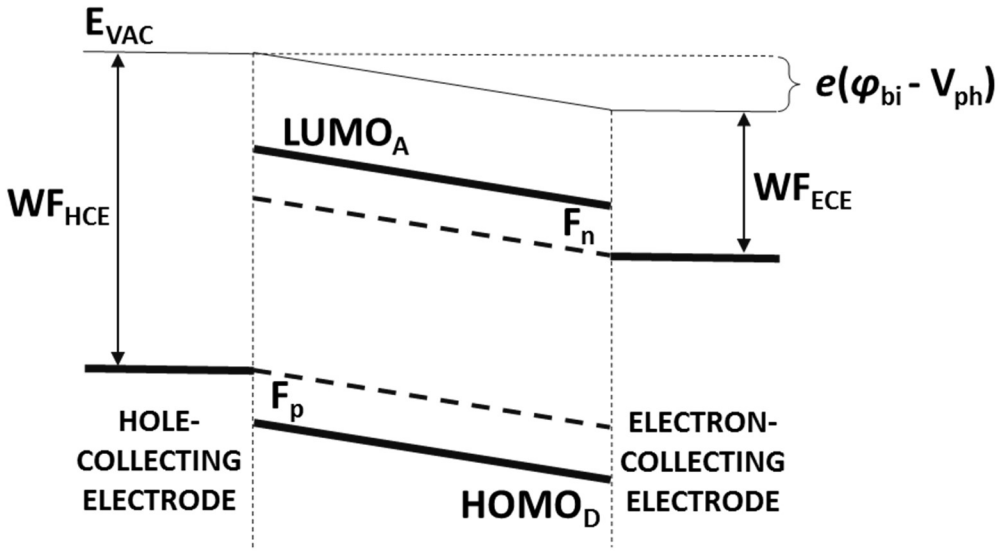

Figure 2-12 Energy level diagram of an OPV device under illumination.

As previously seen in Eqs. (2-18) and (2-19), the gradient of the quasi-Fermi level energies drives the resulting photocurrent. In the extreme case when the quasi-Fermi level energies are equal at the photoactive layer/electrode interfaces, there is no photovoltage and therefore the device is at the short-circuit condition. When the quasi-Fermi level energies are spatially invariant across the device, there is no gradient, and the device is in the open-circuit condition. These two extreme conditions are illustrated in Figure 2-13.

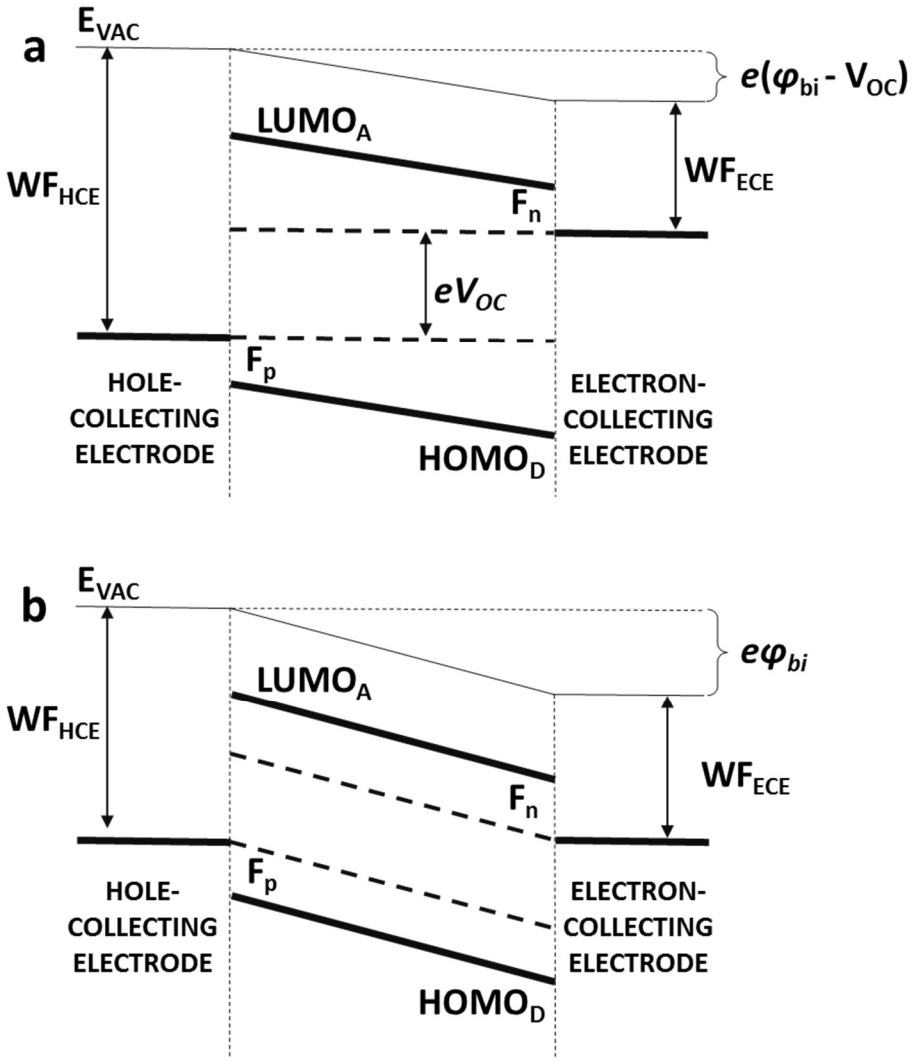

Figure 2-13 Energy level diagram of OPV device under a, open-circuit condition and b, short-circuit condition.

From these energy level diagrams, it becomes evident that the photovoltage and therefore the open-circuit voltage is limited by φ_{bi}. If φ_{bi} is compensated by the photovoltage, the bands are no longer tilted and the necessary electronic asymmetry needed for the operation of the OPV is eliminated. This stresses the importance of having a large WF difference between the electrodes in order to achieve a high V_{OC} in organic solar cells.

In crystalline silicon solar cells this is typically achieved through increased levels of doping.

2.3.4 Equivalent Circuit Model

In an ideal solar cell, the contribution by the photocurrent density is described by a circuit with a current source in parallel with a diode, to model the solar cell's rectifying behavior. The current-voltage characteristics of an ideal solar cell can be described using the ideal Shockley diode equation with an additional term for the photocurrent J_{ph} produced under illumination shown by:

$$J = J_0 \left(\exp\left(\frac{eV}{nk_BT}\right) - 1 \right) - J_{ph} \tag{2-23}$$

where J is the current density (A cm^{-2}), J_0 is the reverse saturation current density, V is the voltage across the device, n is the ideality factor ranging from 1 (radiative recombination only) to 2 (Shockley-Read-Hall recombination), k_B is the Boltzmann constant, T is the temperature, and J_{ph} is the photocurrent density. From equation (2-23), we can derive the solar cell output parameters:

$$J_{SC} = -J_{ph} \tag{2-24}$$

$$V_{OC} = \frac{nk_BT}{e} \ln\left(\frac{J_{ph}}{J_0} + 1\right) \tag{2-25}$$

where J_{SC} is the short-circuit current density and V_{OC} is the open-circuit voltage. The J-V characteristics for an ideal diode in the dark and under illumination is given in Figure 2-14.

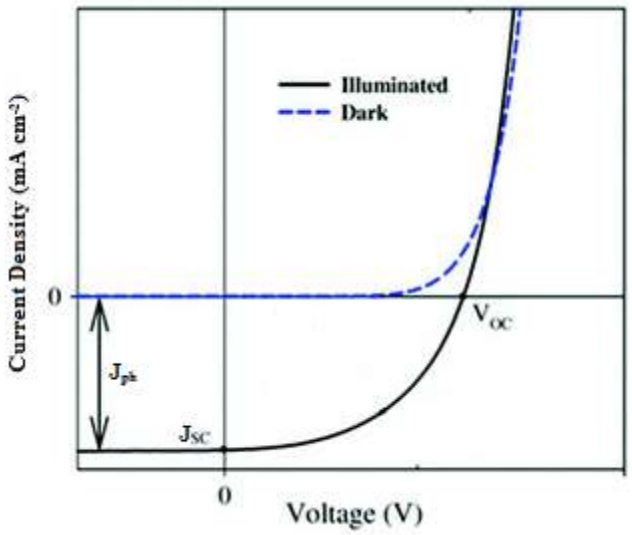

Figure 2-14 *J-V* characteristics of an ideal solar cell in the dark and under illumination

Unfortunately, in practical solar cells there is an important influence of parasitic resistances on their operation, modeled with the equivalent circuit shown in Figure 2-15 Equivalent circuit model for a solar cell. An area scaled series resistance (R_SA) accounts for the resistance of the semiconducting material, the contact resistance at the semiconductor/electrode interface, and resistance to the external leads. Additionally, the shunt resistance (R_PA) accounts for carrier loss and leakage paths resulting from impurities or pinholes in the film [47].

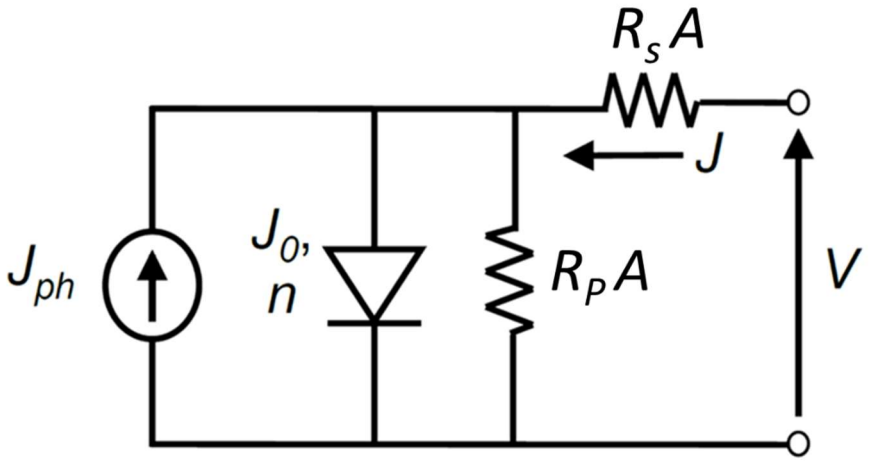

Figure 2-15 Equivalent circuit model for a solar cell.

After performing a circuit analysis, a general equation for the current density in the solar cell can be derived:

$$J = \frac{1}{1+R_S/R_P}\left[J_0\left\{\exp\left(\frac{V-JR_SA}{nk_BT/e}\right)-1\right\}-\left(J_{ph}-\frac{V}{R_PA}\right)\right] \quad (2\text{-}26)$$

where R_s is the series resistance, R_P is the shunt resistance. In an ideal solar cell $R_S = 0$ and $R_P \rightarrow \infty$. From this general equation, the J_{SC} and the V_{OC} can be explicitly derived.

2.4 Electrical Doping of Semiconductors

2.4.1 Inorganic Semiconductors

Doping of inorganic semiconductors is a controlled and well understood process used to increase the number of free charge carriers. In a doped inorganic semiconductor, atoms from the lattice are replaced by an impurity atom. Doping of crystalline silicon is shown as an example in Figure 2-16.

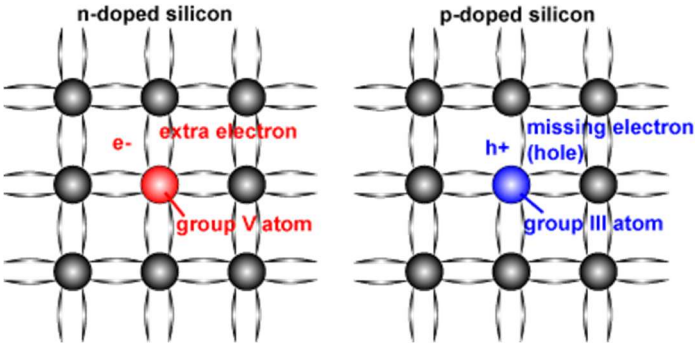

Figure 2-16 N and p-type doping of crystalline Si. Figure reproduced from [49].

The dopants occupy positions within the lattice of the host material (substitutional) and therefore, have a high doping efficiency (typically generating one free charge carrier per dopant atom). This leads to a dramatic increase in inorganic semiconductor conductivity even at ultralow doping ratios, thus retaining high charge carrier mobilities, as the crystalline order of the highly pure host is largely unperturbed. Donor impurity atoms have one valence electron more than necessary for chemical bonding with neighboring atoms, while acceptor impurity atoms have one valence electron less than is necessary for chemical bonding with the neighboring atoms. Therefore, shallow donors, which have electrons weakly Coulombically bound to the dopant atom, will readily ionize at room temperature since they require little thermal energy to donate the excess electron into the conduction band of the semiconductor. Similarly, shallow acceptors have energy levels close to the top of the valence band and readily capture electrons, or donate weakly bound holes. Introducing dopants leads to a shift of E_F towards the conduction band in the case of *n*-doping and towards the valence band in the case of *p*-doping. On the other hand, deep dopants are harmful to solar cells as they cause recombination centers or electron/hole traps

[9]. The mass action law for non-degenerate doped semiconductors still holds ($n_0 p_0 = n_i^2$) and the carrier densities are defined as:

$$n_0 = n_i e^{(E_F - E_i)/k_B T} \tag{2-27}$$

$$p_0 = n_i e^{(E_i - E_F)/k_B T} \tag{2-28}$$

where n_0 is the density of conduction electrons, p_0 is the density of holes, n_i is the intrinsic carrier density, E_F is the Fermi level energy, E_i is the Fermi level energy of the intrinsic material, k_B is the Boltzmann constant, and T is the temperature. In inorganic materials, doping is typically achieved at high temperatures by the diffusion of dopant atoms or through ion implantation, allowing a more sharply defined dopant distribution [9].

2.4.2 Organic Semiconductors

In organic semiconductors, controlled and stable electrical doping requires the addition and immobilization of strong oxidizing or reducing molecules in specific regions of a device to induce *p*- or *n*-type electrical doping, respectively. Organic semiconductors are considered to be intrinsic because no dopants are intentionally introduced. While doping inorganic materials by introducing impurity atoms into a crystalline semiconductor is a highly controllable process, early attempts at introducing alkali metals or halides as dopants in organic semiconductors proved challenging since they are not covalently bonded to the host and have a strong tendency to diffuse. The relatively low mass density of organic semiconductors and propensity for diffusion or migration of small molecule dopants throughout the bulk of these materials contributes to the disorder in the material. Molecular doping emerged as a promising alternative by introducing much larger electron

acceptors or donors to tune the optical and electrical properties of donor polymers [50]. Even at low levels, controlled electrical doping can fill traps thereby increasing charge mobility, conductivity, and improve overall charge transport [51]. Recent work has shown molybdenum based [52, 53] and 2,3,5,6-tetrafluoro-7,7,8,8-tetracyanoquinodimethane (F4-TCNQ) [54] dopants effectively dope layers of the donor polymer poly(3-hexylthiophene-2,5-diyl) (P3HT).

Unlike their inorganic counterpart, doping of organic semiconductors involves an intermolecular charge transfer between the host and dopant molecule. A molecular *n*-dopant donates an electron from its HOMO to the LUMO of the host material, while a molecular *p*-dopant accepts an electron from the HOMO of the host to its LUMO, in effect creating a hole in the host. Similar to inorganic semiconductors, introducing *n* (*p*)-type dopants causes a shift in E_F closer to the LUMO (HOMO) band of the organic semiconducting material. Although the doping mechanisms in organic semiconductors are poorly understood, in general a favorable energy alignment is necessary, with the LUMO of the dopant having a higher energy than the HOMO of the host for efficient p-type doping and the reverse being true for n-type doping. This charge transfer is shown in an energy level diagram in Figure 2-17.

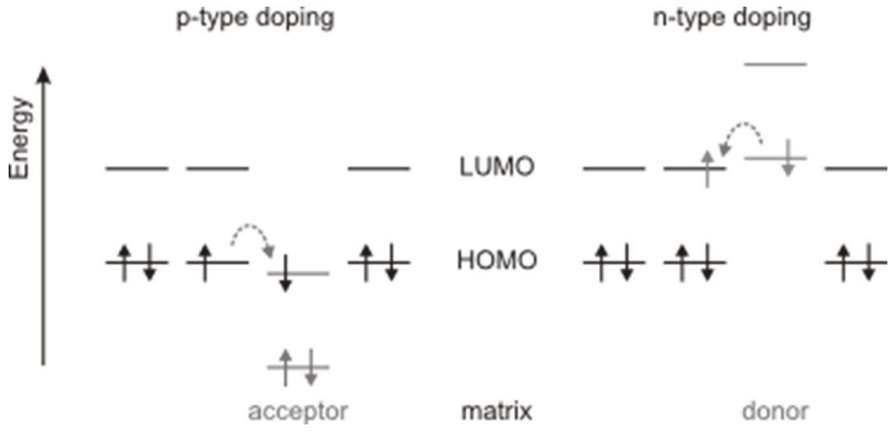

Figure 2-17 Charge transfer during *n* and *p*-type doping of organic semiconductor host matrix.

The doping process is generally broken down into two main steps. The dopants are first ionized by transferring an electron or hole to the host and leaving a hole or electron behind on the dopant molecule. Second, the Coulombically bound charge pair must be dissociated into free charge carriers. Whereas in inorganic semiconductors the thermal energy at room temperature is enough to dissociate the electron (hole) on the host from the Coulomb attraction of the of the remaining hole (electron) on the dopant molecule, this is not the case for organic semiconductors. The binding energy of holes (electrons) to the negatively (positively) ionized molecular dopant in organic semiconductors is on the order of ~0.5 to 0.8 eV due to the low dielectric constant of organic semiconductors [55]. This poor dissociation efficiency results in high doping ratios, necessitating dopant concentrations on the order of a percent for practical applications. However, at such high concentrations, the structural integrity of the organic semiconductor may be compromised resulting in it becoming more amorphous upon doping. In turn, this results in an increased density of traps and scattering centers for free charge carriers, which is detrimental to their mobility [56].

2.5 Interlayers in OPV Devices

Efficient and stable charge-collecting interlayers play a pivotal role in OPV device performance. Most common approaches rely on either the use of electron (hole) collection layers or surface-modification of an electrode through the chemisorption or physisorption of certain materials. In the first approach, thin layers of either metal-oxides (e.g. MoO_x or

ZnO), conducting polymers like poly(3,4-ethylenedioxythiophene) polystyrene sulfonate (PEDOT:PSS), or electrically-doped organic semiconductors with electron or hole-transport properties, are used. Transition metal-oxides, which have very large WF values (5.5 - 6.9 eV) [57], depending on their history of air exposure, are substitutes to the more traditionally used PEDOT:PSS. Shrotriya et al. show that layers as thin as 3 to 5 nm of these materials evaporated on an ITO substrate act as a hole-collecting layer and have performances similar to the P3HT:PCBM reference device using PEDOT:PSS [58]. For electron-collecting layers, ZnO is the preferred low WF metal-oxide, deposited either by sputtering or from solution [57, 59]. In the second approach, chemisorbed surface modifiers, polyelectrolytes, or physisorbed non-conductive materials are used to modify the work function of electrodes upon the formation of surface dipoles. Simple aliphatic amines (e.g. polyethylenimine (PEI) and polyethylenimine ethoxylated (PEIE)) or poly(ethylene glycol) (PEG) have recently been shown effective at facilitating electron collection from OPVs, and yield air-stable contacts that improve OPV lifetime. In 2012, Zhou et al. [60] showed a universal and air stable way of modifying the work function of many conductors often used as electrodes in organic electronics. Low concentrations of PEIE in 2-methoxyethanol were spun on the conductor to induce a vacuum level shift and therefore a reduction in the WF. This amine-containing large band gap polymer is insulating and not considered a charge- collecting layer, instead it behaves as a surface modifier. It was able to modify the WF in some cases by over 1 eV and produced efficient electron-collecting electrodes in OPV devices. Recently, self-forming electron-collecting interlayers have been demonstrated in OPVs by incorporating either PEIE or PEG directly in the bulk of the OPV device photoactive layer [61-64]. When small concentrations of

PEIE were added to the photoactive layer blend, upon deposition, the PEIE phase separated to the bottom. This created dipoles on the conductive bottom layer, decreasing the WF for efficient electron collection. This self-organization of an electron-collecting layer facilitated the fabrication of a simplified and efficient tandem solar cells with efficiencies of up to 10.8%. In the case of PEG, a blend of the photoactive layer with PEG was also deposited, but, upon the deposition of the Al top electrode, instead of staying at the bottom interface PEG created an electron collecting layer by migrating to the top blend/Al interface.

2.6 Electrical Doping in OPV Devices

Controlled electrical doping of organic semiconductors already plays a central role in the design and fabrication of efficient OPVs [65]. Doping in OPVs is often done through vacuum thermal evaporation since it provides a path for fabrication of complex single- and multi-junction OPV devices with efficiencies up to 13.2% because the deposition of a new layer on top of an existing layer and the co-deposition of two materials can be easily implemented [65-67]. While electrical doping using vacuum-based techniques is widely used, the fabrication of multilayer devices with doped layers using vacuum-free solution-based processing techniques remains a major challenge. OPVs doped in solution using small molecule p-typed dopants such as the model F4-TCNQ showed poor performance and stability [68, 69]. Previous studies using F4-TCNQ in the bulk of the photoactive layer demonstrated the formation of deep traps and a decrease in the V_{OC} due to trap-assisted recombination. The sharp drop in V_{OC} with decreasing light intensity is directly dependent on the additional traps. To resist the diffusion of dopants into the active layer, large ionic

polymer dopants were used to limit the migration to the region at the metal/organic interface [70]. The sub-monolayer deposition of non-conjugated strong polyelectrolytes e.g. sulfonated poly(sulfone)s led to contact doping at the anode-semiconductor interface and efficient hole-extraction. The amount of doping still remained a challenge as the performance of the devices was heavily dependent on the degree of sulfonation of the dopant polymer and the thickness of the dopant layer.

Concerned about introducing traps into the photoactive layer, recent demonstrations showed a separately doped transfer-laminated donor polymer layer that would behave as a hole-collecting layer [52, 53]. A molybdenum based dopant, molybdenum tris-[1-(methoxycarbonyl)-2-(trifl uoromethyl) ethane-1,2-dithiolene ($Mo(tfd\text{-}CO_2Me)_3$), was dissolved in the same solvent as the donor polymer at varying concentrations. The doped film was separately spun on a silicon substrate and then transferred, via soft contact transfer lamination using a polydimethylsiloxane stamp, onto the target substrate containing the photoactive layer. These OPV devices with a doped layer demonstrated efficient hole collection and comparable performance to those using PEDOT:PSS for hole-collection.

2.7 Polyoxometalates in Organic Electronics

Phosphomolybdic acid (PMA) and phosphotungstic acid (PTA) belong to a class of polyoxometalates (POMs) with a Keggin structure [71]. In the context of organic electronics, PMA was mixed in small concentrations to with a solution containing poly(N-vinylcarbozole) (PVK) to create cross-linked hole-injecting layers in efficient blue phosphorescent organic light-emitting diodes (OLEDs) [72]. In this approach, p-type

electrical doping of the layer was not observed. In the context of OPVs, spin-coated layers of PMA and PTA processed from 2-propanol (IPA) have been reported to behave as standalone hole-collecting interlayers in both conventional and inverted device architectures [73-76]. However, it was suggested, through measurements of the XPS spectrum of the solution-processed POMs, that either no doping or only slight interfacial *p*-type doping was present in these devices [75]. Recently, we have shown that PMA induces *p*-type doping and crosslinks the donor polymer poly[*N*-9′-heptadecanyl-2,7-carbazole-alt-5,5-(4′,7′-di-2-thienyl-2′,1′,3′-benzothiadiazole)] (PCDTBT), which was then used as a hole-collection interlayer in OPVs with a conventional geometry [77].

CHAPTER 3

EXPERIMENTAL PROCEDURES AND CHARACTERIZATION

The steps in the fabrication process of OPV devices are discussed here. The tools, experimental setups, and procedures to accurately characterize the electrical and optical properties of OPV devices and doped polymer films will be presented in this section.

3.1 Materials

Various materials were used as donors and acceptors in the photoactive layer blends. The donors consisted of poly(3-hexylthiophene-2,5-diyl) (P3HT) (Reike Metals), poly-[4,4,9,9-tetrakis(4-hexylphenyl)-4,9-dihydro-s-indaceno[1,2-b:5,6-b']dithiophene-2,7-yl}-alt-{2,6-bis([1,2,5]thiadiazolo[3,4-c]pyridine-4'-yl)-4,4-bis(2-ethylhexyl)-cyclopenta[2,1-b:3,4-b']dithiophene-7',7''-yl] (PIPCP) (synthesized by the Bazan group at UCSB), and poly[(5,6-difluoro-2,1,3-benzothiadiazol-4,7-diyl)-alt-(3,3'''-di(2-octyldodecyl)-2,2';5',2'';5'',2'''-quaterthiophen-5,5'''-diyl)] (PffBT4T-2OD) (Cal-OS). For acceptor materials, various fullerene derivatives were used [6,6]-Phenyl C61 butyric acid methyl ester ($PC_{61}BM$) (Nano-C), [6,6]-Phenyl C71 butyric acid methyl ester ($PC_{71}BM$) (Solenne), and 1',1'',4',4''-tetrahydro-di[1,4]methanonaphthaleno[5,6]fullerene-C60 (ICBA) (LumTec). Combinations of these donors and acceptors were blended together in solution to form the photoactive layer ink. The solvents used to dissolve the mixture of donors and acceptors was either chlorobenzene (CB) (Sigma Aldrich), 1,2-dichlorobenzene (DCB) (Sigma Aldrich), or a CB/DCB blend. The choice of solvent has profound effect on the drying time due to the difference in boiling

points (131 °C for CB and 180 °C for DCB) and also on the morphology and growth of the photoactive layer [78, 79]. By choosing the correct solvent or combination of solvents results in better performing devices. To further optimize the photoactive layer morphology, additives such as 1,8-Diiodooctane (DIO) (Sigma Aldrich) are used in small concentrations mixed directly with photoactive layer ink. Other films of donor polymers and small molecules were used for characterization of changes in their optical and electrical properties as well as their photo-oxidative stability after being electrically doped. These donors were not incorporated into device structures and include poly[(4,8-bis-(2-ethylhexyloxy)-benzo(1,2-b:4,5-b′)dithiophene)-2,6-diyl-alt-(4-(2-ethylhexyl)-3-fluorothieno[3,4-b]thiophene-)-2-carboxylate-2-6-diyl)] (PTB7) (1 – Material), and poly[(4,8-bis-(2-ethylhexyloxy)-benzo(1,2-b:4,5-b′)dithiophene)-2,6-diyl-alt-(4-(2-ethylhexanoyl)-thieno[3,4-b]thiophene-)-2-6-diyl)] (PBDTTT-C) (Solarmer), X2, and poly[*N*-9′-heptadecanyl-2,7-carbazole-alt-5,5-(4′,7′-di-2-thienyl-2′,1′,3′-benzothiadiazole)] (PCDTBT) (LumTec).

For electron collection, an amine containing polymer PEIE diluted in 2-methoxyethanol was used a surface modifier to lower the WF of the bottom electrode. For hole collection, either a thermally evaporated layer of MoO_3 or directly doped photoactive layer was used. Doping of the polymer films, which will be described in the next chapter, was achieved using a strong oxidizing agent, PMA, mixed at various concentrations in nitromethane. To reverse this process and de-dope the polymer, a strong reducing agent is used, hydrazine hydrate, mixed with acetonitrile.

3.2 Fabrication

The fabrication of the OPV devices introduced in later sections consist of depositing several layer of organic materials, metals, and metal oxides on a substrate. Each of these layers serves an electrical function, and the overlap serves as the active area of the device. The absorbing photoactive layer is deposited from solution where a donor polymer and fullerene-derivative is blended in a common solvent. The top metal electrode and the hole-collecting transition metal oxide (MoO_3) for reference devices is thermally evaporated, while an amine containing polymer used for electron collection is solution processed. The details of the fabrication processed will be discussed in this section.

3.2.1 Substrate Preparation

An important step of device fabrication includes the patterning, cutting, and cleaning of the substrates. For all of the devices presented in future sections, a glass substrate pre-coated with tin-doped indium oxide (ITO) (Colorado Concept Coatings LLC) with a sheet resistance (R_{SH}) of ~15 Ω/ is used. The low R_{SH} paired with a high degree of transparency is necessary for optimal device operation, to avoid any additional series resistance as well as to allow the penetration of incident light into the device. For large area devices, the R_{SH} has to be minimized.

The OPV devices are fabricated on 1” x 1” substrates. Since the sheet of glass/ITO is 14” x 14”, it has to be cut down to the appropriate size. Firstly, the non-uniform part of the deposited ITO around the perimeter of the sheet is removed by cutting 0.5-1” off all the way around. The sheet is then scored on a cutting mat into 1” x 4” strips in order to pattern them via acid etching.

These shorter strips are then masked off using Kapton tape, covering half of the ITO along the length of the strip. A beaker was then filled with 100 mL of a mixture of hydrochloric (HCl) and nitric acid (HNO_3) in a 3:1 ratio. The strips of masked glass/ITO are then gently lowered into the beaker lengthwise on its edge without fully submerging the entire strip. After ~3 min, the strip is removed from the acid mixture and rinsed thoroughly with deionized water. If no unetched islands of ITO on the unmasked portion of the strip are present, the Kapton tape is removed and the strip is cut down to the correct 1" x 1" size. If the ITO is not fully etched, it is important to place the strip back into the beaker until only glass remains on the unmasked portion.

Once all of the strips are etched and cut down to the 1" x 1" size, they are placed into a sample holder. They are then manually scrubbed with Liquinox detergent in deionized (DI) water to remove any remaining tape residue. The cleaning steps of the substrates are essential to formation of uniform films when processing the subsequent layers. The samples then go through four sequential baths of DI water and Liquinox, DI water, acetone, and IPA in an ultrasonicator (Branson 5510) for at least 20 min each at 45 °C. After the last bath, the samples are removed, blown dry by a stream of N_2 gas, and placed in Petri dishes.

3.2.2 Doping of Polymer Films

Solutions of PMA (Alfa Aesar) or phosphotungstic acid (PTA) (Alfa Aesar) with different concentrations in nitromethane (Sigma Aldrich) were prepared by mixing it with a magnetic stirrer in a glass vial inside a N_2-filled glove box. Substrates containing the polymer films were then dipped for times varying from 60 s to 60 min into a petri dish with

the PMA solution. To remove any remaining electron-accepting PMA residue at the interface, the doped devices were sprayed and spin-rinsed with 1 mL of pure nitromethane at 2000 rpm for 30 s.

For the characterization of their electrical and optical properties, neat polymer films of the aforementioned donors were fabricated on glass or on glass/ITO substrates. Although not patterned as necessary for full OPV devices, the substrates did undergo the same cleaning procedure. Solutions were then prepared with P3HT films used for XPS, optical, and electrical measurements were spun from a 10 mg mL^{-1} or 30 mg mL^{-1} solution in chlorobenzene, giving thicknesses of 30 nm and 210 nm respectively, which had previously stirred at 70 °C at 500 rpm for 12 h inside a N_2-filled glovebox, at 800 rpm for 30 s on glass/ITO or plain glass. They were then solvent annealed for 3 h and thermally annealed at 150 °C for 10 min on a hot plate. Using the doping procedure described above with a 0.5 M or 50 μM concentration of the PMA nitromethane solution, the films were immersed for various times.

Similar to P3HT, solutions of PBDTTT-C, PTB7, PIPCP, and PffBT4T-2OD were prepared in 10 mg mL^{-1} solution in chlorobenzene and spun on glass or glass/ITO substrates at 1000 rpm for 30 s. These films were then also characterized. PCDTBT was prepared in 30 mg mL^{-1} solution in chlorobenzene and used for photo-oxidative stability studies.

3.2.3 Reference Devices

Reference devices have a general three-layer structure in between two electrodes shown in Figure 3-1.

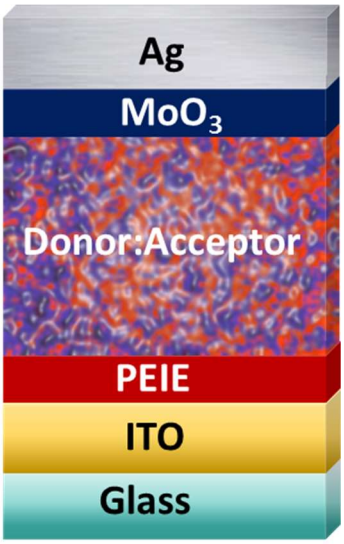

Figure 3-1 Cross section of reference device structure.

A solution of 1:1 by weight P3HT:ICBA in 1,2-dichlorobenzene (Sigma Aldrich) was simultaneously mixed with a total concentration of 80 mg mL^{-1} for thick-active-layer (500 nm) devices and 40 mg mL^{-1} for thinner (200 nm) active layer devices on a hot plate at 70 °C at 500 rpm and set to stir for 12 h inside a N_2-filled glovebox. A 0.4 wt.% PEIE solution was prepared in 2-methoxyethanol and spun on each of the substrates at 5000 rpm for 60 s through a 0.2 µm polytetrafluoroethylene (PTFE) filter (VWR) under a fume hood in ambient conditions and then thermally annealed at 100 °C for 10 min. A PEIE layer on an ITO surface has been previously demonstrated to reduce the WF and improve electron collection [60]. The samples were then transferred into a N_2-filled glove box to process the photoactive layer. A film of P3HT:ICBA was spun on top of glass/ITO/PEIE at 800 rpm for 30 s through a 0.2 µm PTFE filter. The films were solvent annealed for 4 h and then thermally annealed at 150 °C for 10 min on a hot plate to remove any remaining solvent and aid in the crystallization of P3HT in a N_2-filled glovebox. Chemical resistant wipes were then soaked in chlorobenzene and used to wipe away the top portion of the

photoactive layer and expose the underlying ITO, in order to make Ohmic contact to the bottom electrode.

For PIPCP devices, a solution of 1:2 by weight PIPCP:$PC_{61}BM$ in chloroform:chlorobenzene with a 3:2 ratio by volume was simultaneously mixed with a total concentration of 30 mg mL^{-1} for 110 nm-thick devices at 40 °C at 500 rpm and set to stir for 12 h inside a N_2-filled glovebox. A 0.4 wt.% PEIE solution was prepared in 2-methoxyethanol and spun on each of the substrates at 5000 rpm for 60 s through a 0.2 μm PTFE filter under a fume hood in ambient conditions and then thermally annealed at 100 °C for 10 min. The samples were then transferred into a N_2-filled glove box to process the photoactive layer. A film of PIPCP:$PC_{61}BM$ was spun on top of glass/ITO/PEIE respectively at 2000 rpm for 60 s through a 0.2 μm PTFE filter. The films were solvent annealed for 1 h. No additional thermal annealing steps were required.

For PffBT4T-2OD devices, a solution of 1:1.4 by weight PffBT4T-2OD:$PC_{71}BM$ in dichlorobenzene:chlorobenzene with a 1:1 ratio by volume with 3 v% DIO was simultaneously mixed with a total concentration of 43.2 mg mL^{-1} for 230 nm-thick devices at 110 °C at 500 rpm and set to stir for 12 h inside a N_2-filled glovebox. A 0.4 wt.% PEIE solution was prepared in 2-methoxyethanol and spun on each of the substrates at 5000 rpm for 60 s through a 0.2 μm PTFE filter under a fume hood in ambient conditions and then thermally annealed at 100 °C for 10 min. The samples were then transferred into a N_2-filled glove box to process the photoactive layer. A film of PffBT4T-2OD:$PC_{71}BM$ was spun on glass/ITO/PEIE at 800 rpm for 20 s from hot solution onto substrates pre-heated to 110 °C. The films were solvent annealed for 1 h, vacuum annealed for 1 h, and then thermally annealed at 110 °C for 5 min.

All of the devices were transferred to a connecting N_2-filled glovebox containing a high-vacuum thermal evaporation system (SPECTROS, Kurt J. Lesker). The samples were placed on a sample holder and secured with Kapton tape. The sample holder was then set onto a mask holder with a mask used to pattern the electrodes. Five finger electrodes and a rectangular section define the bottom and top electrodes. The top view indicating the electrodes is shown in Figure 3-2.

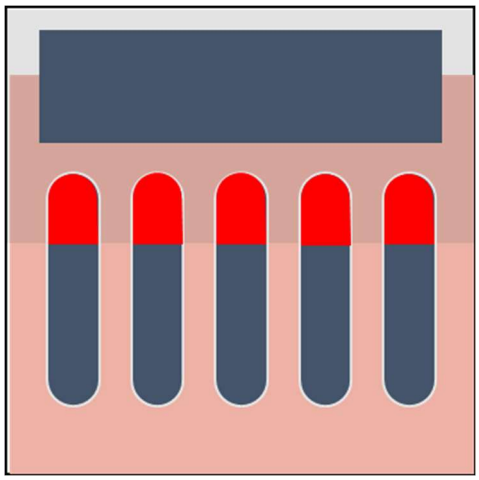

Figure 3-2 Top view of completed OPV device. Red semi-circular areas define the overlap of all layers, known as the active area.

The stacked sample and mask holder are placed into the chamber of the thermal evaporator, and the pump down process is initiated. Once the pressure is $<10^{-7}$ torr, the material source is heated to reach the material sublimation temperature through a series of ramping and soaking steps. During the deposition process, the stage is rotated to prevent a shadowing effect on the electrodes. The hole-collecting MoO_3 and an array Ag or Al top contacts were evaporated sequentially.

3.2.4 Two-layer OPV Devices

Two-layer devices in general follow the same fabrication steps as described for the reference devices. Here, the only difference is in the formation of the hole-collecting layer. After completing all processing and post-processing steps of the photoactive layer, the substrate with the stack of layers was immersed into the PMA nitromethane solution at a concentration of 0.5 M for PMA-im-P3HT:ICBA devices, 0.05 M for PMA-im-PIPCP:$PC_{61}BM$ devices, and 0.1 M for PffBT4T-2OD:$PC_{71}BM$ devices for 60 s using the procedure described above. Lastly, the top Ag metal electrodes were evaporated to complete the device structure.

3.2.5 Single-layer OPV Devices

Single-layer OPV devices incorporate the electron-collecting PEIE directly into the photoactive layer solution. After mixing the photoactive layer in the glovebox for 12 h, 0.4 wt% PEIE in 2-methoxyethanol was added to the P3HT:ICBA solution 6% v/v and to the PIPCP:$PC_{61}BM$ solution 4% v/v and stirred at room temperature in a N_2-filled glovebox for 1 h. The remaining fabrication steps are identical to the two-layer devices.

3.2.6 Devices with Transfer Laminated Hole-Collecting Interlayer

To investigate the behavior of doped polymer films as hole collecting interlayers, a soft contact transfer lamination method was used to transfer a pristine film of P3HT onto a device with a 200 nm-thick P3HT:ICBA photoactive layer. The P3HT:ICBA layer was similarly processed as described earlier from 40 mg mL^{-1} solution in DCB. A separate film of polydimethylsiloxane (PDMS) was fabricated on a smooth Si wafer by thoroughly

mixing a PDMS base and cross-linker together, pouring it on the Si wafer, and curing it in a vacuum oven at 80 °C for 1 h. The PDMS film was then placed onto a separately spin coated film of pristine P3HT and immersed in distilled water. The P3HT film transfers onto the PDMS, which is then stamped onto the target substrate and slowly peeled off. The entire stack was then again annealed at 150 °C for 10 min, immersed into 0.5 M PMA nitromethane solution for 5 or 15 min, and rinsed with pure nitromethane before loading into the thermal evaporator for top Ag electrode deposition. The process flow is illustrated in Figure 3-3.

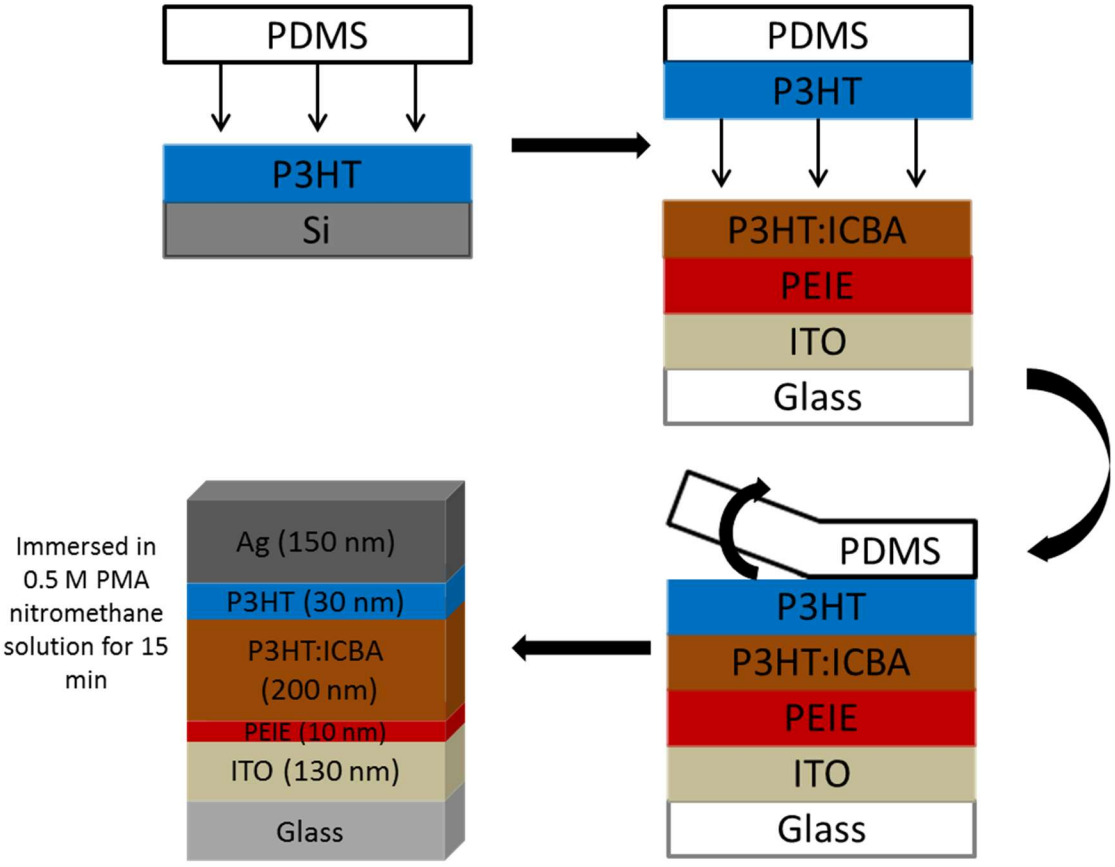

Figure 3-3 Process flow of using transfer lamination to use a doped polymer film for hole-collection in OPV device.

3.3 Characterization

3.3.1 Transmission Line Method

For doped semiconductors, changes in the conductivity or sheet resistance (R_{SH}) were measured using the transmission line method (TLM). The cross section of a polymer film is shown in Figure 3-4

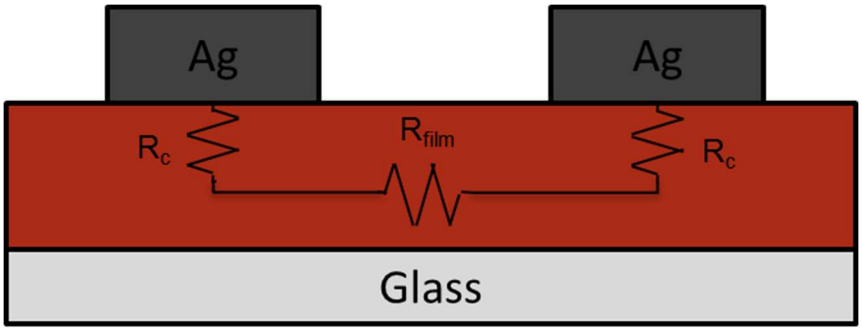

Figure 3-4 Cross section of polymer film on a glass substrate.

Here we calculate the total resistance (R_{total}) as the sum of the two contact resistances (R_C) and the film resistance (R_{film}) given by:

$$R_{total} = R_{film} + 2R_C \tag{3-1}$$

R_{film} is the resistance of the polymer film and is treated as a three dimensional conductor with a uniform cross section. This is given by:

$$R_{film} = \rho \frac{L}{A} = \rho \frac{L}{Wd} \tag{3-2}$$

where ρ is the resistivity, L is the length, W is the width, and d is the thickness of the film. Sheet resistance is defined as:

$$R_{SH} = \frac{\rho}{d} \tag{3-3}$$

The polymer films were immersed in PMA solution for various times as described in the previous section and an array of Ag contacts was thermally evaporated onto the surface of the polymer film. The distances between or lengths of the top Ag contacts were 200, 100, 50, and 25 μm, and the widths of the contacts were 2400 and 1200 μm as shown in the diagram in Figure 3-5.

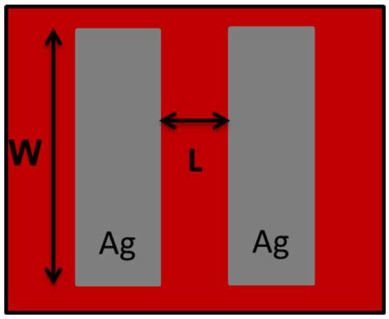

Figure 3-5 Top of the Ag contacts on the polymer film with varying widths and distances apart from each other.

Using a probe station in an N_2-filled glovebox, R_{total} is extracted by running a current-voltage scan. Combining Eqs. (3-2) and (3-3) gives the linear equation:

$$R_{total} = \frac{R_{SH}}{W} L + 2R_C \tag{3-4}$$

By plotting the R_{total} as a function of electrode distance as seen in the example in Figure 3-6, the sheet resistance and the contact resistance can be extracted from the slope and y-intercept of the interpolated line.

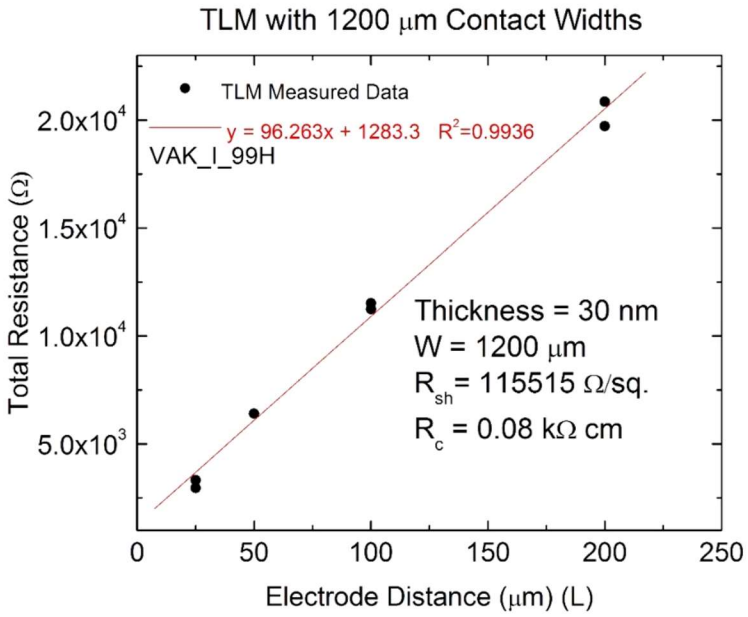

Figure 3-6 Total resistance plotted as a function of electrode distance (L) and the extracted R_{SH} and R_C.

3.3.2 Kelvin Probe

To determine changes between the WFs or Fermi level energies of pristine and doped polymer films, a Kelvin probe was used to measure the contact potential difference (CPD). CPD measurements yield the difference between WFs of the sample (φ_S) and a reference tip (φ_{Tip}) as seen in Figure 3-7.

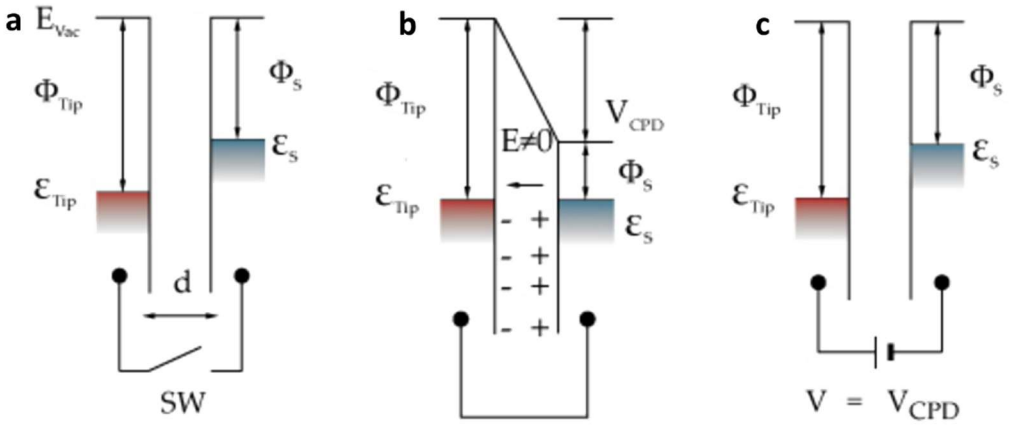

Figure 3-7 Operating principles of a Kelvin probe.

The tip and the sample create a parallel plate capacitor. When the plates are connected with no applied voltage, the potential difference between the two surfaces (U) is the contact potential difference $\left(V_{CPD} = \varphi_{Tip} - \varphi_S\right)$. Changes in the distance between the surfaces (d) induce charge flow and therefore current in the circuit. In the case of a Kelvin probe, the gold grid or tip oscillates sinusoidally. Thus, the distance between the surfaces changes such that:

$$d = d_0 + d_1 \sin(\omega t) \tag{3-5}$$

where d_0 is the initial separation between the surfaces, d_1 is the amplitude of the oscillation, ω is the oscillation frequency, and t is the time. The resulting current is given by:

$$I = U\frac{dC}{dt} = U\frac{d}{dt}\left(\frac{\varepsilon\varepsilon_0 A}{d_0 + d_1 \sin(\omega t)}\right) = -U\varepsilon\varepsilon_0 A\frac{d_1 \cos(\omega t)}{[d_0 + d_1 \sin(\omega t)]^2} \tag{3-6}$$

Where $(U = V_{CPD} - V)$ is the difference between V_{CPD} and the applied bias V, ε is the dielectric constant, and A is the area of the of the capacitor. When $V=V_{CPD}$, the current becomes zero, and since the WF of the reference tip is known, the WF of the sample can be extracted as $\varphi_S = \varphi_{Tip} - V$. These measurements were conducted using a Kelvin probe inside a N_2-filled glovebox shielded by a Faraday cage. They were calibrated to freshly cleaved highly ordered pyrolytic graphite (HOPG) with a known work function of 4.6 eV

[80]. Along with TLM measurements, this is another important technique to characterize the electrical properties of doped polymer films.

3.3.3 XPS

To determine the presence of PMA in a P3HT film, surface survey scans and depth profiling was conducted using a Thermo K-Alpha X-ray photoelectron spectroscopy (XPS) system. XPS is a powerful surface technique used to study material composition and chemical state information. XPS measurements are typically performed by exciting a sample surface with mono-energetic Al kα x-rays causing photoelectrons to be emitted from the surface of the sample. The energy of the emitted photoelectrons is measured with an electron energy analyzer. Intensities of photoelectron peaks at different binding energies determine the elemental identity, chemical state, and quantity of a detected element. Analysis of the intensity peaks is often performed using a Gaussian peak decomposition. The resulting relative peaks and binding energies are compared with references to determine the elemental composition and chemical states.

In this investigation, a low-energy Ar^+ ion beam was used for etching a 210 nm film of P3HT spun on an ITO substrate and immersed in a solution of 0.5 M PMA in nitromethane for 10 min. This low-energy etching combined with subsequent surface scans at various binding energy ranges provides a depth profile with a breakdown of the chemical interactions at each etch with a resolution of 2 - 4 nm.

3.3.4 Ellipsometry

Spectroscopic ellipsometry is a measure of polarization change between the known polarization of the source and the reflected light. These changes are described by the complex ratio (ρ) or the ratio of the *s* and *p* components of polarized light given by:

$$\rho = \tan(\Psi)e^{i\Delta} \tag{3-7}$$

where $\tan(\Psi)$ is the amplitude ratio after reflection and Δ is the phase difference. Since no direct equation exists to relate Ψ and Δ to the optical constants, the refractive index n and the extinction coefficient k, a model must be constructed to calculate the predicted response from Fresnel's equations. The model is then compared to the measured data to determine the accuracy of the fit.

The spectroscopic ellipsometry and transmittance data was collected using a spectroscopic ellipsometer (J.A. Woollam M-2000UI) and data modeled using the software CompleteEASE^{TM} (J.A. Woollam). Ellipsometry measurements in this investigation were used to extract the optical constants, thicknesses, and doping profiles of various materials, described in more detail in a later section. To measure accurate thicknesses of polymer films, a film was spin coated on a glass substrate and taped on the back to eliminate backside reflection.

3.3.5 Solar Simulation

J–V characteristics of the devices were measured with a source meter (Keithley 2400) in an N_2-filled glovebox controlled by a custom written LabView program. A 300 W xenon lamp (6258, Newport) with an air mass 1.5G filter and an intensity of 100 mW cm^{-2} was used as the light source inside the solar simulator (Newport Oriel) with the spectrum shown in Figure 3-8.

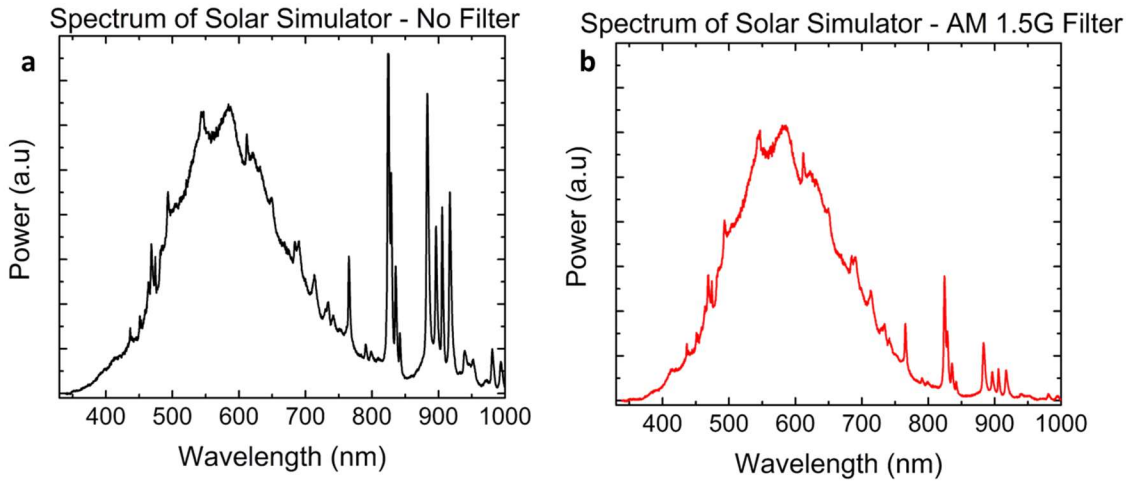

Figure 3-8 Power spectra of the solar simulator **a,** without a filter and **b,** with and AM 1.5G filter used as the source of illumination for OPV device characterization.

The light intensity of the solar simulator was calibrated by a Si photodiode (Hamamatsu S1133) and no mismatch factor was used. In an effort to provide an accurate characterization of OPV devices, individual devices were electrically isolated from each other using a razor blade and tested through an aperture with a well-defined area to avoid overestimation of the J_{SC}. However, variations of less than 5% where observed in OPV performance when tested without electrical isolation and without an aperture as seen for a sample device in Figure 3-9 and described in greater detail in a later section.

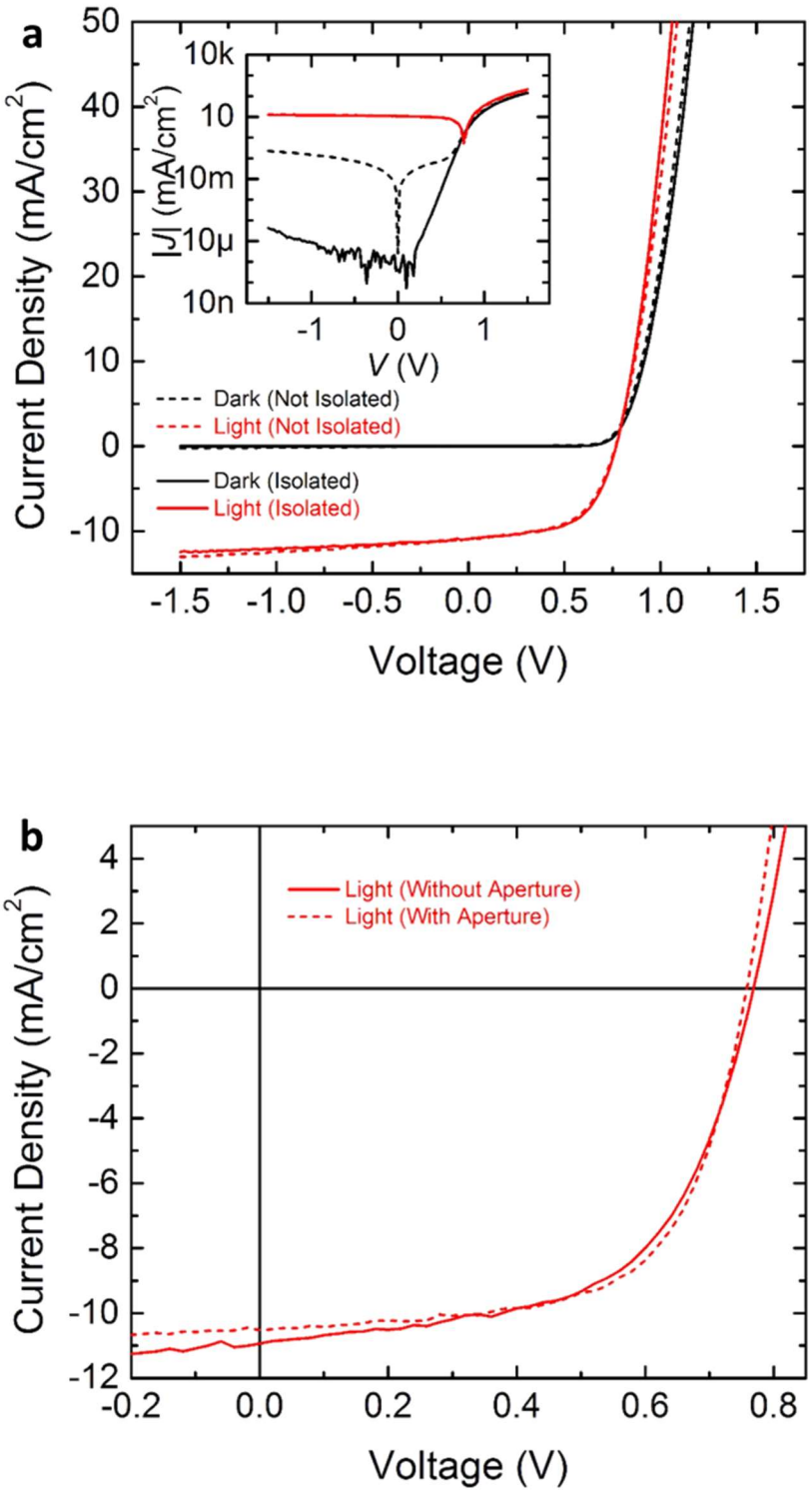

Figure 3-9 a, *J–V* characteristics of devices with doped photoactive layer devices before and after electrical isolation by scratching around the top contacts (immersion in 0.5 M PMA nitromethane solution for 60 s). The inset shows the *J–V* characteristics on a

semilogarithmic scale. **b,** *J–V* characteristics of PMA doped device under simulated 100 mW cm^{-2} AM 1.5 G illumination with and without the use of an aperture after electrical isolation.

Devices with directly doped active layers were tested before and after electrically isolating the contacts. A full table of those results can be found in the appendix. Doped and reference devices were measured using an aperture with a defined area of 0.05 cm^2.

3.3.6 Photo-oxidative Stability

The electro-optical properties and long-term stability of polymers are significantly affected by oxidative decomposition in air. Photo-oxidation refers to this decomposition which is accelerated under light exposure. These chemical changes cause disruptions of the π conjugation of the polymers and reduce photoabsorbance in a process known as photobleaching [81]. Therefore, photo-oxidative stability is critical for the overall stability and lifetime of OPV devices in air that incorporate conjugated polymers.

To test the photo-oxidation of P3HT and PCDTBT, the polymer films were exposed to light from a 300 W Xenon lamp through an infrared (IR) filter in ambient conditions with the spectrum shown in Figure 3-10.

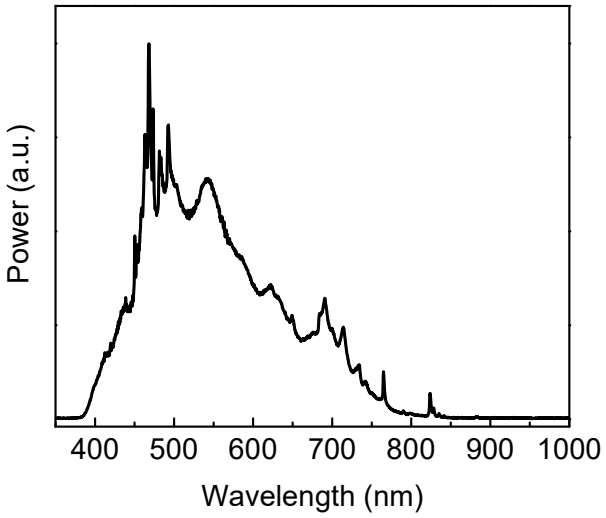

Figure 3-10 Power spectra of the 300 W Xe lamp filtered with an IR filter used as the source of illumination in photo-oxidation experiments with an irradiance of 150 mW cm^{-2}.

The power spectra of the transmitted light were monitored over the course of 19 – 73 h with a spectrometer (Ocean Optics USB2000+) to observe changes in the absorbance of the pristine and PMA doped polymer films. The films were then further characterized by measuring the transmittance using the ellipsometer before and after illumination by the Xenon lamp. For this investigation, pristine films of 210 nm-thick P3HT and 300 nm-thick PCDTBT and PMA doped films in 0.5 M PMA nitromethane solution were used.

3.3.7 External Quantum Efficiency

Another important characterization of an OPV device is the external quantum efficiency (EQE). The EQE determines the ratio of the number charge carriers collected over the number of incident photons for a given wavelength. To measure the EQE, a lamp (CVI Special Products CERMAX) was integrated with a monochromator (CVI Spectral

Products CM110) and focused onto the active area of the OPV devices using optical lenses and mirrors. These measurements were conducted in air on OPV devices encapsulated with a piece of glass sealed with epoxy. To calibrate the system, the output of the monochromator passed through a beam splitter and an optical power meter with a silicon photodiode was used to measure the optical power for each wavelength at the device testing site as well as at the reference site. By measuring the power at the reference site during device testing, the ratio of these powers was used to determine the actual power of the incident light on the OPV device. The output of the monochromator was then varied over a 400 – 1700 nm wavelength range by a custom LabView program. The program was also coupled to an electrometer (Keithley 6517A) to measure the device output current.

CHAPTER 4

Solution-based Electrical P-type Doping of Polymer Films Over a Limited Depth

In the next two chapters, a novel method of solution-based electrical doping of organic semiconductors and its application in OPV devices is introduced. The widely applicable and simple approach broadens the understanding of underlying mechanisms and paves the way for new device architectures. This chapter will uncover how a facile immersion process into a solution of a strong oxidizing agent, PMA, results in drastic changes of the electrical and optical properties of polymer films. Using combinations of experimental and modeling techniques, strong evidence of dopant penetration into and chemical interactions with the polymer films is shown.

4.1 Introduction

Similar to inorganic semiconductor technologies, methods of electrically doping organic semiconductors are expected to be key enabling technologies for optimizing charge collection or injection from organic electronic devices. In contrast with electrical doping in inorganic semiconductors, in organic semiconductors this requires the addition of strong electron-accepting or electron-donating molecules that induce p- or n-type electrical doping through a charge-transfer reaction between the host material and the dopant molecule. One approach is by using small molecule dopants, although this can result in their diffusion throughout the bulk of the material. To reduce diffusion, large molecular dopants [82, 83] and/or dopant or doped interlayers are used instead of direct doping of the semiconductor bulk [52, 53]. In solution, for some dopants, lack of spatial control and

diffusion makes controlled and stable electrical doping challenging [68, 69, 84, 85]. For instance, in OPV devices, p-type dopants such as F4-TCNQ have been used by blending them directly with the active layer solution. However, doped OPV devices typically showed poor device performance due to a higher density of traps introduced into the bulk [68, 69]. In the context of interlayers, polymers containing simple aliphatic amine groups have been shown to lead not only to reductions of the WF of an electrode but also to n-doping of acceptor materials [60].

Recently, we have used PMA to induce *p*-type doping, across the film thickness, and crosslinking of neat films of poly[*N*-9′-heptadecanyl-2,7-carbazole-alt-5,5-(4′,7′-di-2-thienyl-2′,1′,3′-benzothiadiazole)] (PCDTBT) to yield an independent hole-collection interlayer in OPVs [77]. PMA belongs to a class of polyoxometalates (POMs), also known as heteropoly acids, with a Keggin structure [71]. PMA has been used to cross-link films of poly(*N*-vinylcarbazole) (PVK) in organic light-emitting diodes but *p*-type doping was not observed following this approach [72]. Here, we demonstrate oxidative (*p*-type) doping over a limited depth by post-processing immersion of films of donor-like conjugated organic semiconductors into a POM (PMA and PTA) solution in nitromethane. Our key findings are: (i) the use of nitromethane as the solvent of PMA is critical to enable doping into the film *within a limited depth* from the surface by varying the exposure time to the solution; (ii) films of polymers, including state-of-the-art donor-acceptor co-polymers [34, 86-89] that have been doped with PMA *exhibit improved photo-oxidative* stability in air.

4.2 Results and Discussion

4.2.1 Optical Properties and Chemical Interactions

We studied the optical properties of P3HT films immersed for 30 min in a 0.5 M solution of PMA in nitromethane, chemical structures shown in Figure 4-1, and rinsed with pristine nitromethane to remove excess molecules from the film's surface.

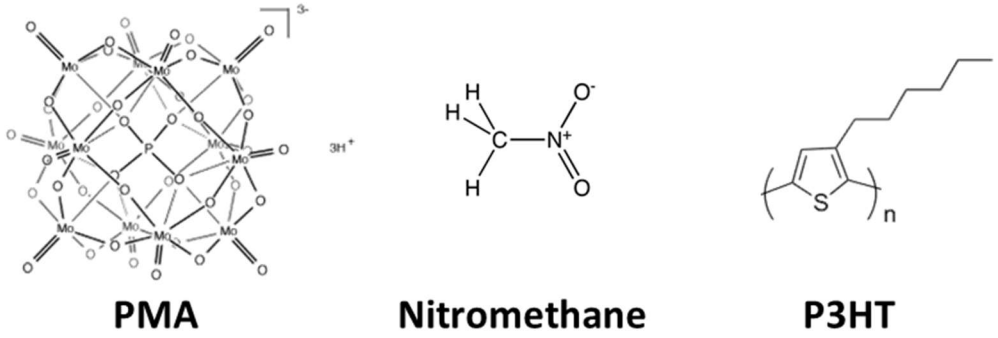

Figure 4-1 Chemical structures of PMA, nitromethane, and P3HT.

Mixing P3HT directly with PMA in solution caused precipitation of the reactants, and, therefore, the films were instead treated by post-process immersion. P3HT films processed following this method, hereon referred to as PMA-im-P3HT (where "im" stands for immersion), displayed notable changes in their transmittance spectra, including the emergence of new absorption bands at near infrared (NIR) wavelengths as demonstrated in Figure 4-2. The normalized change of transmittance $\Delta T/T$ as a function of wavelength (inset of Figure 4-2) reveals spectral signatures that correlate well with those associated with P3HT polaron bands in the region where $\Delta T/T < 0$, and the bleaching of the main π–π* absorption bands, in the region where $\Delta T/T > 0$ [90, 91]. The shape of these polaron bands suggests the presence of additional absorption bands corresponding to PMA

anions[92]. These observations would be consistent with an integer charge transfer from P3HT to PMA, leaving a positively-charged polaron in P3HT and a PMA anion [50, 54].

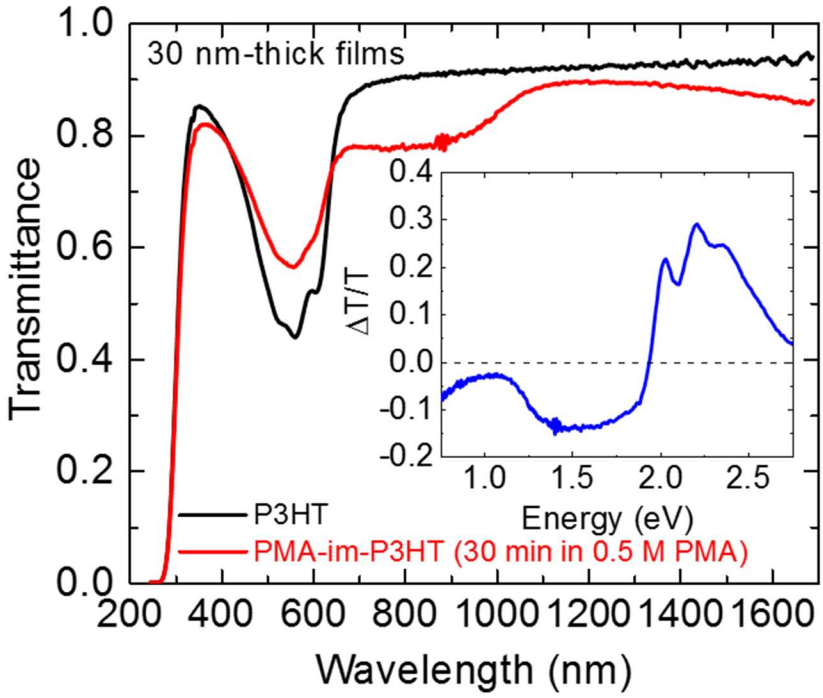

Figure 4-2 The transmittance of 30 nm-thick pristine P3HT and PMA-im-P3HT (after post-process immersion for 30 min in 0.5 M PMA nitromethane solution) films, with the normalized change in the transmittance data in the inset.

To observe the emergence of these polaron bands, 210 nm-thick P3HT films were immersed in a 50 μM PMA nitromethane solution. The increased strength of the polaron bands with longer immersion times suggests an increased amount of PMA within the layer and not just at its surface as seen in Figure 4-3. Similar changes are also observed in Figure 4-4 for P3HT films immersed in a PTA solution in nitromethane.

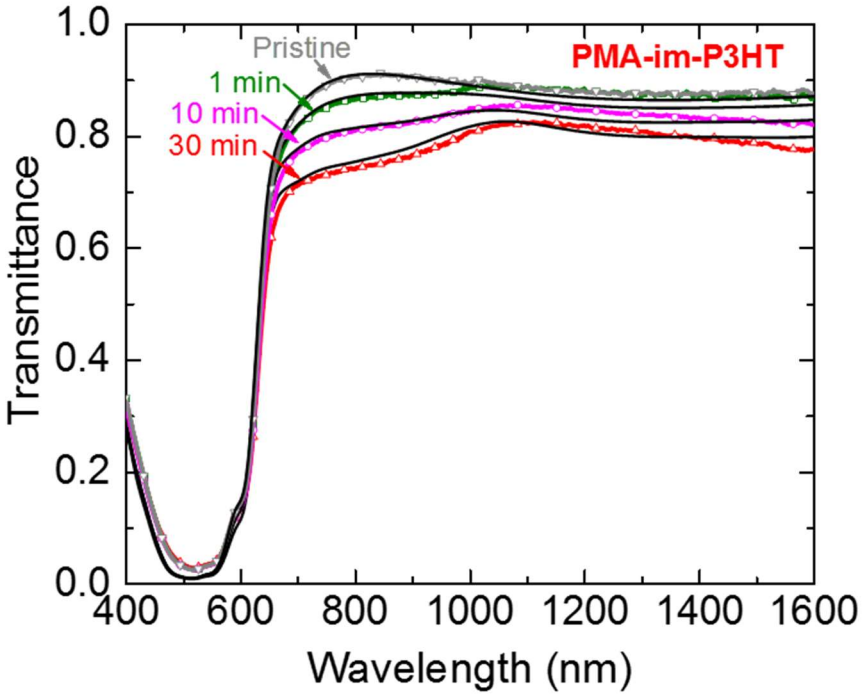

Figure 4-3 The transmittance of 210 nm-thick PMA-im-P3HT films with varying times of post-process immersion in 50 μM PMA nitromethane solution.

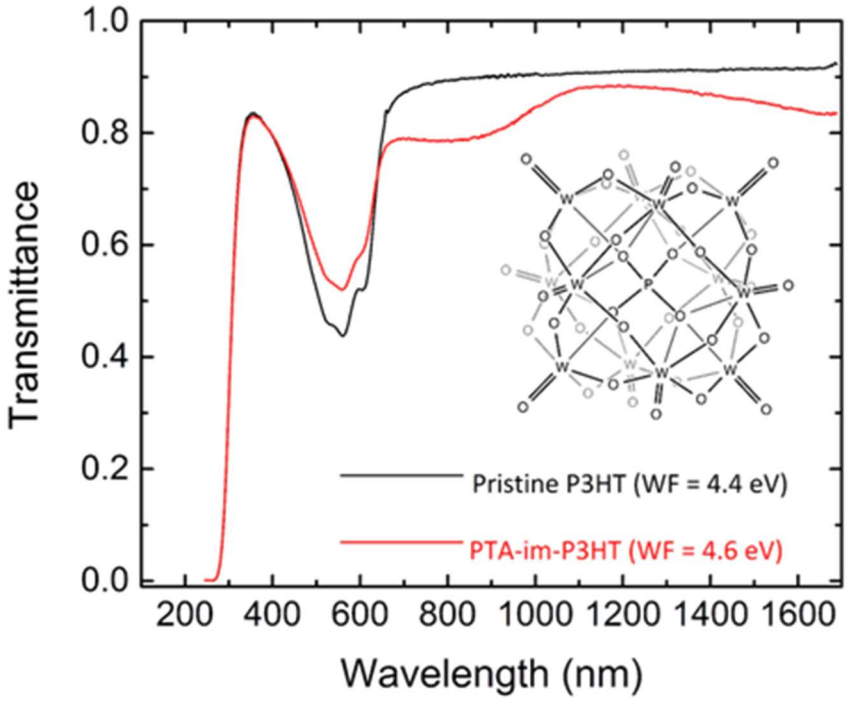

Figure 4-4 Chemical structure of phosphotungstic acid (PTA) and transmittance of 30 nm-thick pristine and P3HT films immersed into a solution of 0.5 M PTA in nitromethane. Work function values as measured by a Kelvin probe are shown in the legend.

To investigate the penetration depth of PMA molecules during post-process immersion of the P3HT films, we conducted XPS depth-profile measurements using ion-beam etching. Figure 4-5 shows high resolution XPS scans at various depths, across different binding energy spectral ranges, displaying a comparison of five characteristic spectral features observed on a 210 nm-thick PMA-im-P3HT film processed by 1 min immersion in a 0.5 M PMA nitromethane solution (for clarity, only the first 77 nm are shown in Figure 4-5).

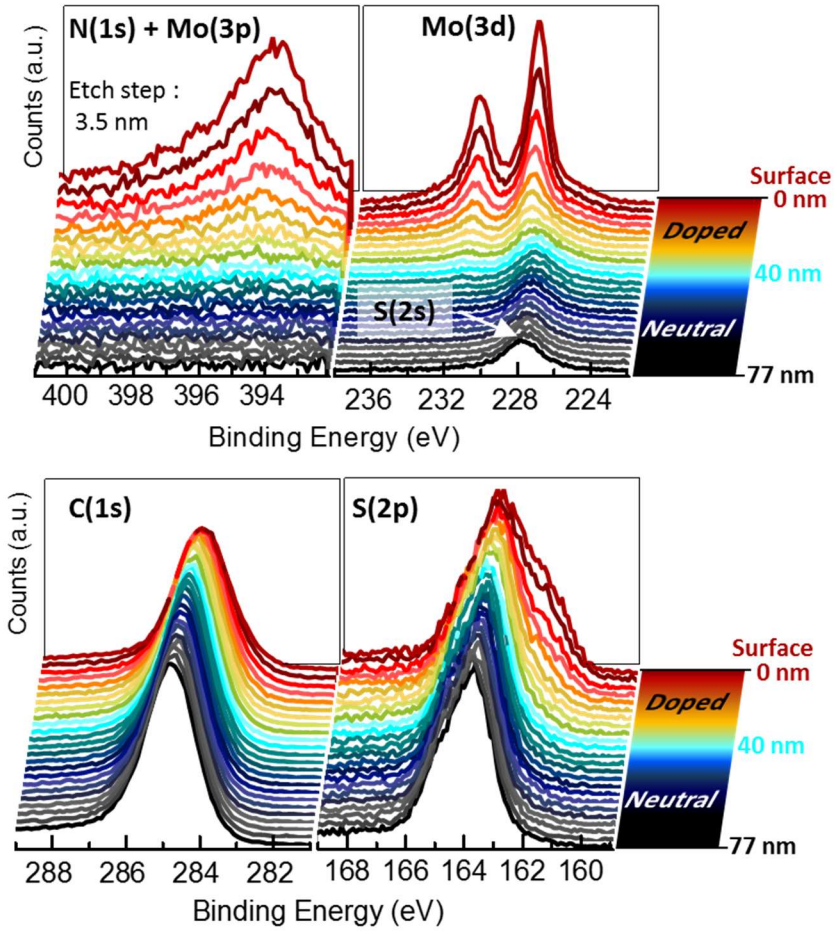

Figure 4-5 High resolution XPS scans as a function of depth at different binding energy spectral ranges on a 210 nm-thick PMA-im-P3HT film processed by 1 min immersion in a 0.5 M PMA nitromethane solution.

The broad spectral feature in the range from ca. 400 to 390 eV is attributed to overlapping N(1s) and Mo($3p_{3/2}$) core level spectra (Figure 4-6) and is found to follow a single exponential decay distribution, with a decay constant of 11 nm, into the film (inset of Figure 4-6).

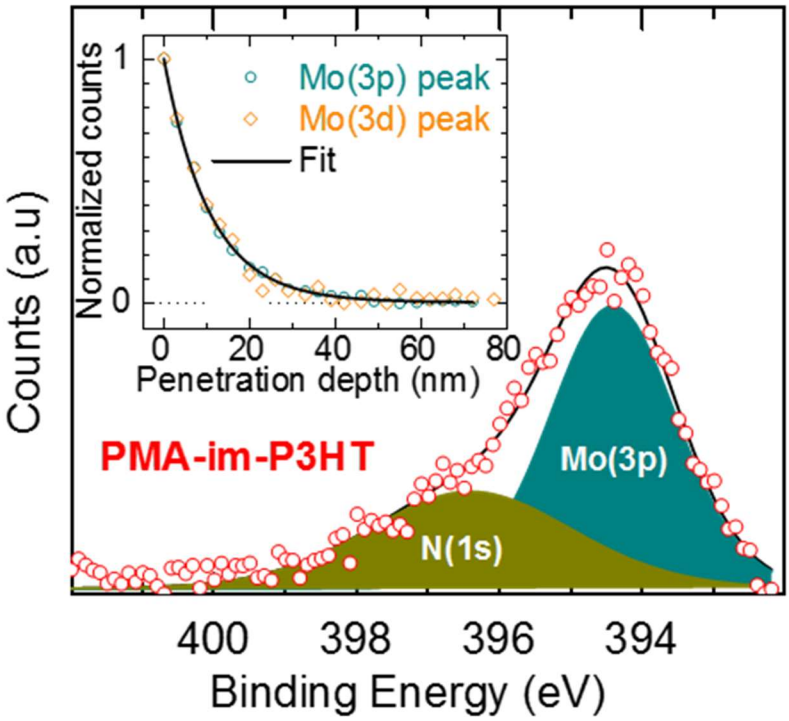

Figure 4-6 Gaussian peak decomposition of the of the XPS measurements of the spectra in the N(1s) binding region showing an overlap with the Mo(3p) peak. The inset shows the exponential decay of the Mo(3p) and Mo(3d) peaks as a function of depth.

The presence of N is attributed to the use of the solvent nitromethane. The presence of Mo is attributed to PMA, and its penetration depth is also confirmed through the

evolution of the Mo(3d) core level spectra. The presence of Mo and N in the film is also correlated with shifts and broadening of the C(1s) and S(2p) core level spectra from P3HT which reveal the existence of substantial electronic interactions in the doped region. Finally, the small peak around 228 eV is attributed to S(2s) core level spectra from P3HT and consequently is observed from the top to the bottom of the film.

4.2.2 Optical Modeling

Considering the exponential profile of the atomic distributions of the dopant molecules observed in XPS, we modeled the optical properties of PMA-im-P3HT films by using an exponential profile to describe the concentration of doped-P3HT phases seen in Figure 4-9. Analysis of the spectroscopic ellipsometry data was carried out using CompleteEASE^{TM} (J.A. Woollam). The Kramers-Kronig-consistent complex refractive index values of P3HT (Figure 4-7) were derived from spectroscopic ellipsometry measurements on pristine P3HT films. The Kramers-Kronig-consistent complex refractive index values of doped-P3HT were found by assuming an isotropic Bruggeman effective medium comprised of pristine P3HT and the unknown doped-P3HT phase. Using this model, we varied the concentration of the doped-P3HT phase and its complex refractive index values to best fit the spectroscopic ellipsometry and transmittance measurements on a 30 nm-thick PMA-im-P3HT film immersed for 30 min in a 5 mM PMA nitromethane solution (Figure 4-7).

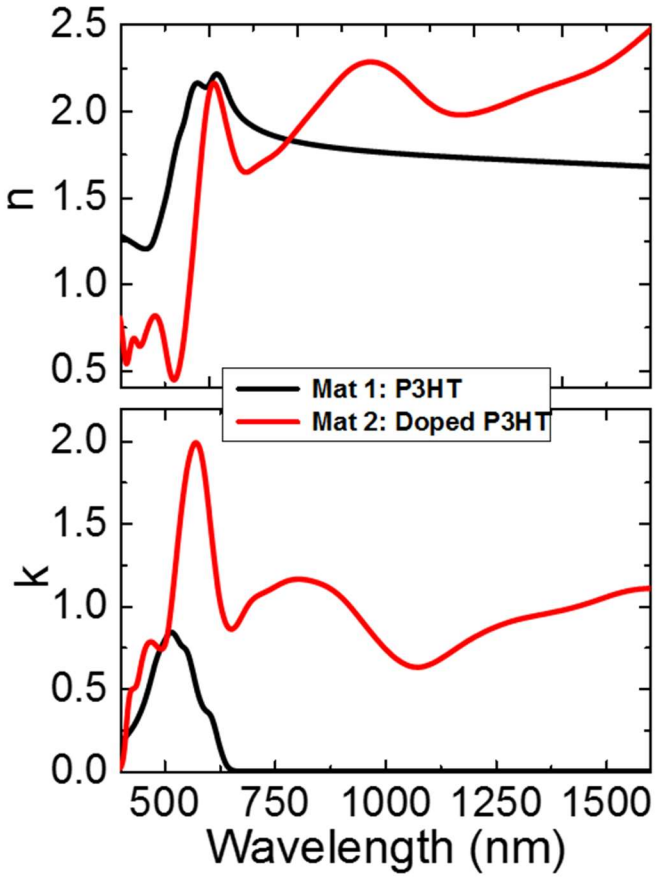

Figure 4-7 Complex refractive index values determined by spectroscopic ellipsometry.

The optical properties of ca. 200 nm-thick PMA-im-P3HT films were modeled using an isotropic Bruggeman effective medium comprised of pristine P3HT and doped-P3HT phases by taking 50 levels across the film depth and by assuming an exponential decay distribution. Using this model, we varied the concentration of the doped-P3HT phase in each layer as well as the decay constant and amplitude of the exponential distribution to best fit the spectroscopic ellipsometry (Figure 4-8) and the transmittance data (Figure 4-3).

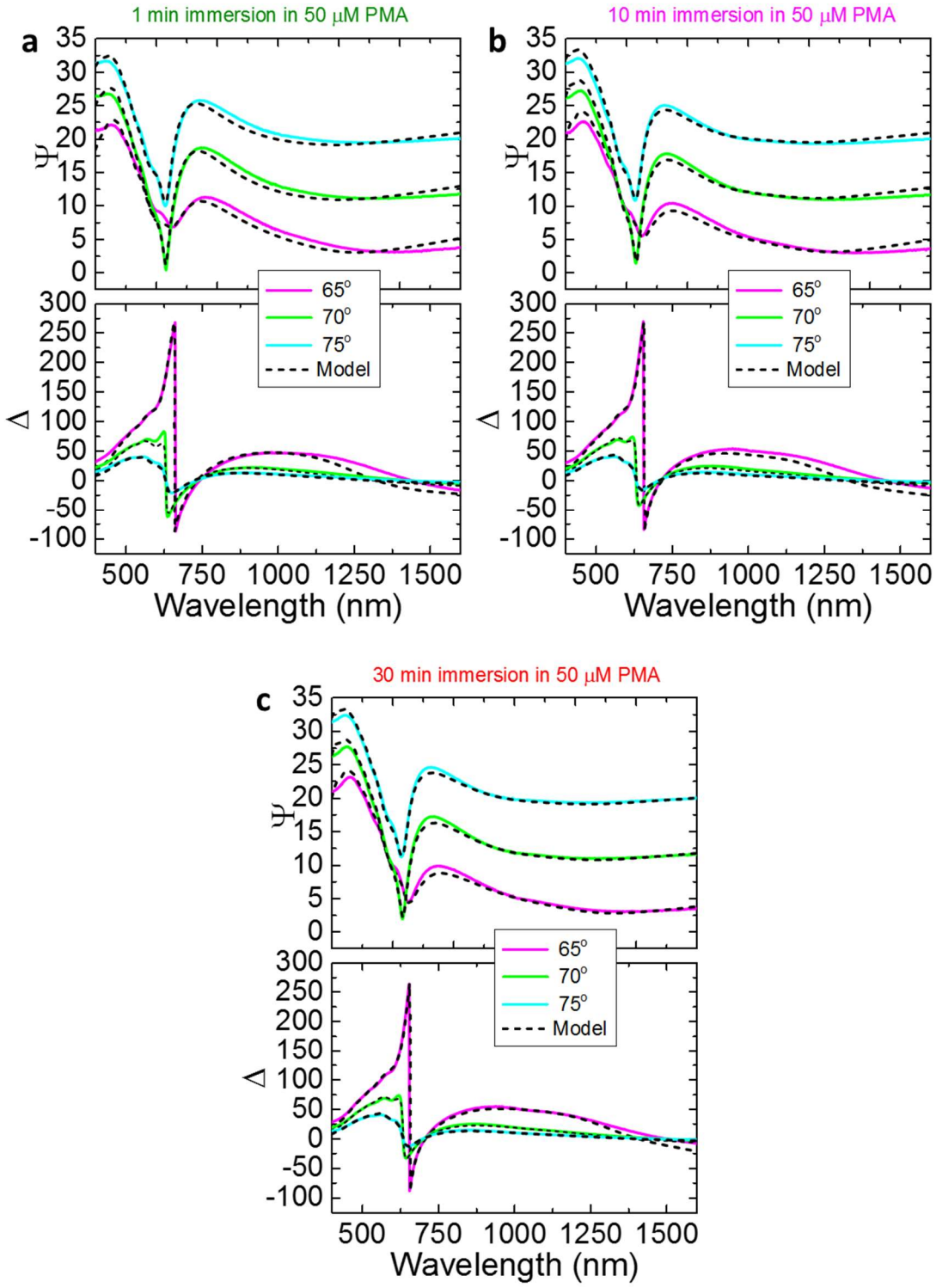

Figure 4-8 Ellipsometric angles measured on a 190 nm-thick P3HT layer immersed for **a,** 1 min **b,** 10 min, and **c,** 30 min in 50 μM PMA nitromethane solution.

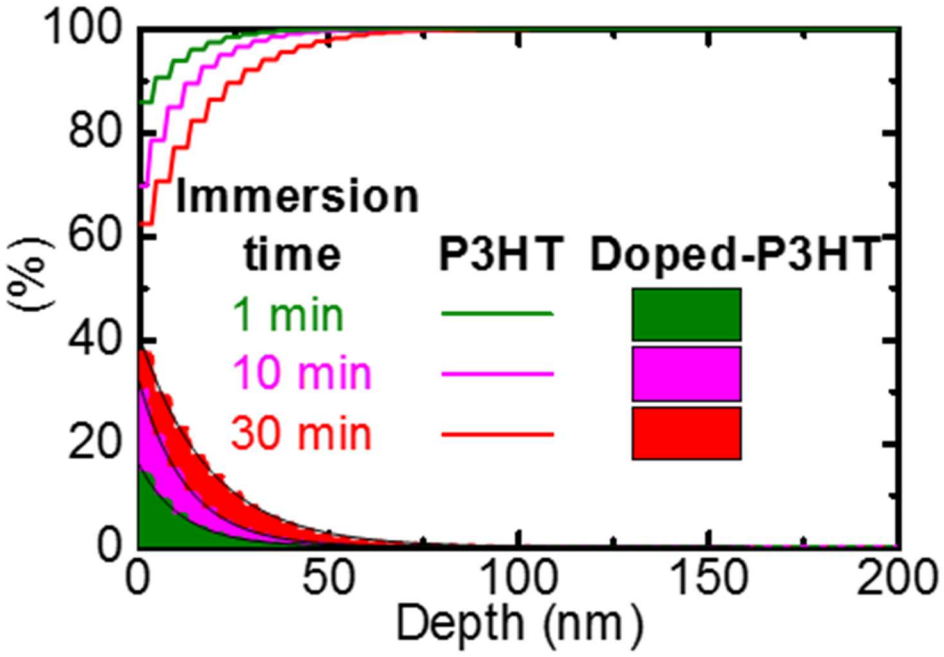

Figure 4-9 The exponential profiles having decay constants of 12, 13 and 18 nm, for 1, 10, and 30 min immersion times in 50 μM PMA nitromethane solutions.

This model reproduces the ellipsometric angles, measured by spectroscopic ellipsometry, as well as the evolution of the transmittance as a function of immersion time and dopant concentration (Figure 4-3). Within the experimental resolution, these results are in good agreement with the XPS studies.

4.2.3 Doping Efficiency

Next, we conducted a comparative analysis of the S(2p) and Mo(3d) core level spectra, near the surface of a pristine P3HT and a PMA-im-P3HT film. In the S(2p) region, Figure 4-10 displays the signature doublet of pristine P3HT with peaks separated by 1.2 eV apart and with an amplitude ratio of 2:1, as previously reported [93]. In contrast, in the

same spectral region a PMA-im-P3HT film produces a broader spectral feature. Figure 4-10 displays a Gaussian peak decomposition of this feature which reveals the appearance of a central doublet corresponding to pristine P3HT, ca. 30% of the S(2p) spectral area; a doublet at higher binding energies corresponding to oxidized P3HT, ca. 35% of the peak area; and a third peak at lower binding energies, which at this point is unidentified and accounting for ca. 35% of the area.

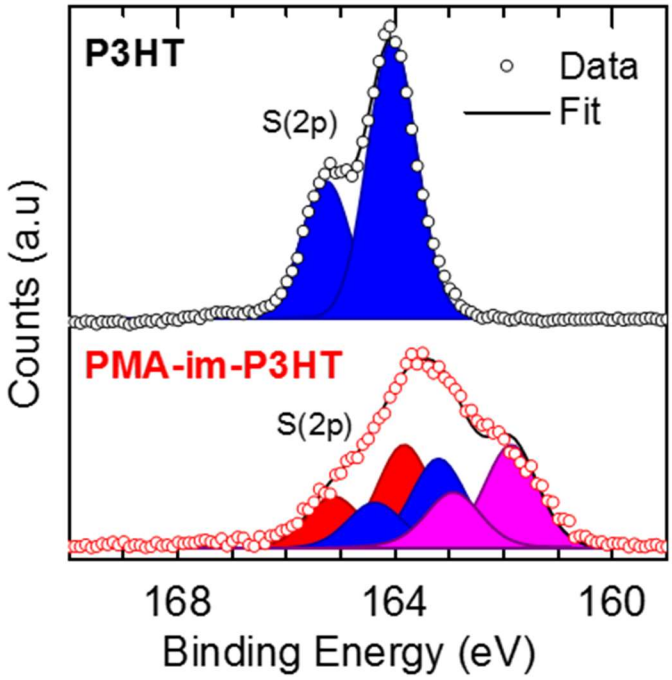

Figure 4-10 Gaussian peak decomposition of XPS measurements in the S(2p) region for pristine and PMA doped P3HT. The shaded regions correspond to neutral P3HT (blue), oxidized P3HT (red), and unidentified peaks (magenta).

We should note that when films are immersed in a 0.5 M PMA solution, the area of oxidized P3HT peaks appears similar regardless of immersion time as seen from Figure 4-11.

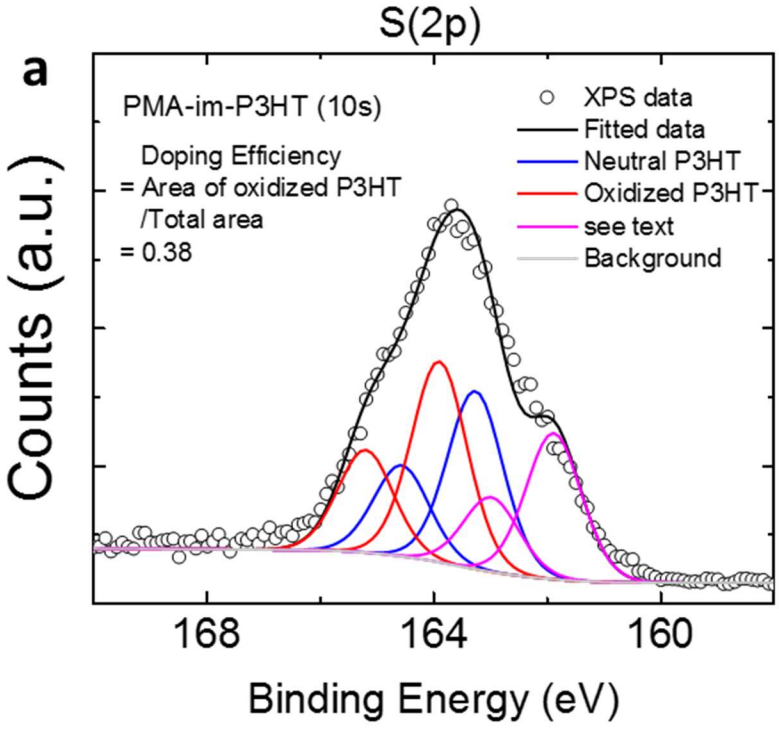
S(2p)
a
PMA-im-P3HT (10s)
Doping Efficiency
= Area of oxidized P3HT
/Total area
= 0.38
XPS data
Fitted data
Neutral P3HT
Oxidized P3HT
see text
Background
Counts (a.u.)
168
164
160
Binding Energy (eV)

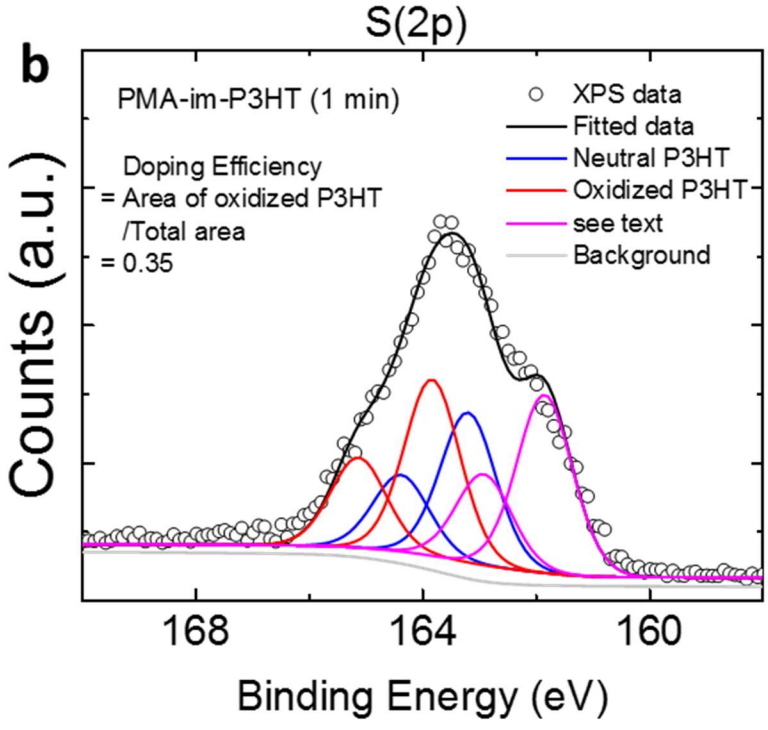
S(2p)
b
PMA-im-P3HT (1 min)
Doping Efficiency
= Area of oxidized P3HT
/Total area
= 0.35
XPS data
Fitted data
Neutral P3HT
Oxidized P3HT
see text
Background
Counts (a.u.)
168
164
160
Binding Energy (eV)

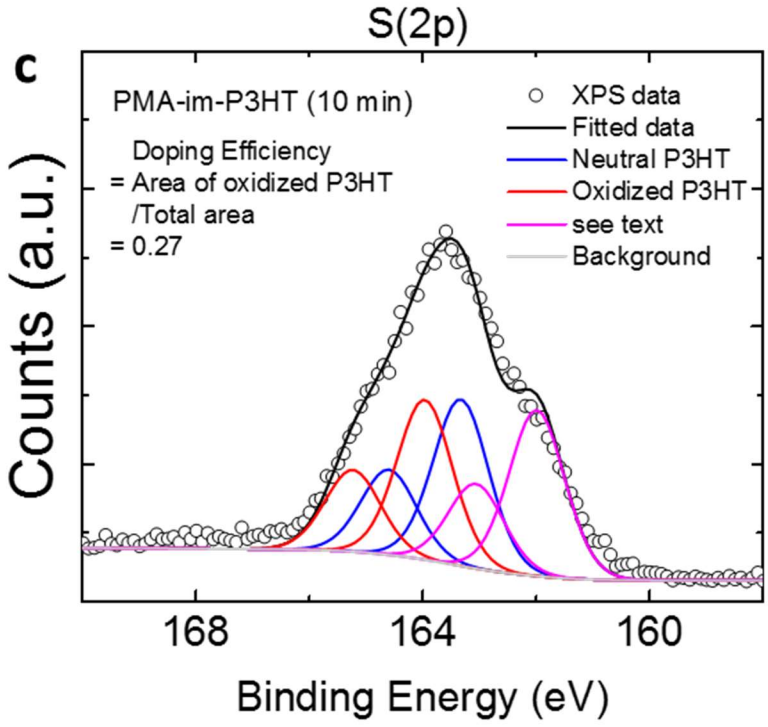

Figure 4-11 a,b,c Gaussian peak decomposition for 210 nm-thick PMA-im-P3HT films immersed for 10 s, 1 min, and 10 min in 0.5 M PMA nitromethane solution.

In the Mo(3d) spectral region pristine P3HT only displays a weak S(2s) peak (Figure 4-12). In contrast, a PMA-im-P3HT film reveals a complex spectral feature comprising five Gaussian peaks. To rationalize the origin of these peaks, XPS measurements were taken on pure PMA powder (Figure 4-12) and revealed four peaks corresponding to the signatures of Mo($3d_{3/2}$) and ($3d_{5/2}$) orbitals in the dominant Mo^{6+} oxidation states and much weaker Mo^{5+} oxidation states. In contrast, XPS spectra on a PMA-im-P3HT film reveals four main peaks corresponding to the signatures of Mo($3d_{3/2}$) and ($3d_{5/2}$) orbitals in the dominant Mo^{4+} peaks and weaker Mo^{5+} oxidation states.

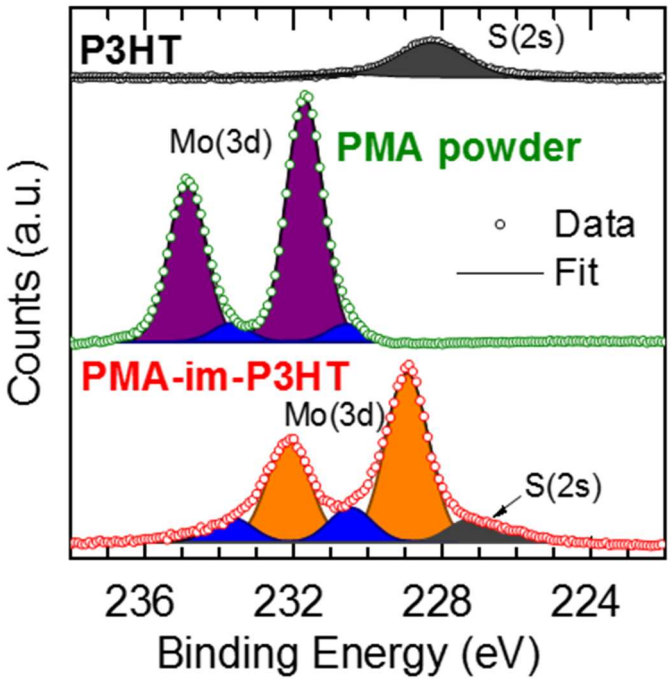

Figure 4-12 Gaussian peak decomposition of XPS measurements in the Mo(3d) region for pristine P3HT, pure PMA powder, and doped P3HT. The shaded regions correspond to Mo^{6+} (purple), Mo^{5+} (blue), Mo^{4+} (orange), and S (gray).

The reduction of molybdenum (PMA) (or tungsten in PTA-im-P3HT films (Figure 4-13)) observed in the doped region accompanied by the oxidation of sulfur in P3HT provides clear evidence of the charge transfer reaction from P3HT to PMA (or PTA), as also suggested by the optical transmittance measurements.

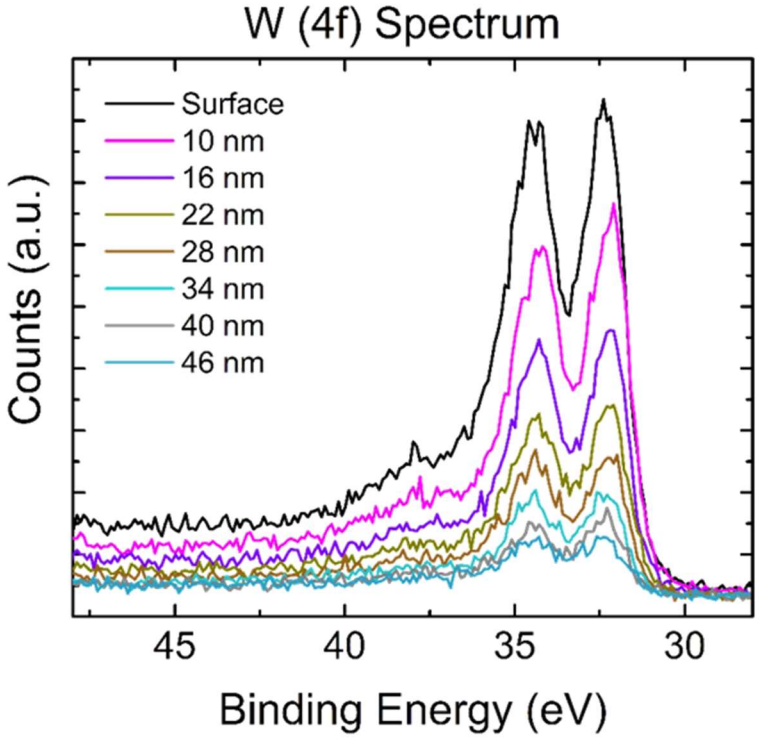

Figure 4-13 Penetration of tungsten at the W (4f) binding energies into the bulk of a 52 nm film of P3HT immersed in a 0.5 M PTA solution in nitromethane for 30 min .

In contrast, P3HT films immersed in a solution of PMA in ethanol display smaller changes of their transmittance spectra, and depth profile XPS studies reveal a significantly smaller concentration of reduced PMA across the film (i.e. the strength of the Mo(3d) peak is weaker than that of the S(2s) peak, as shown in Figure 4-14), thus confirming the enabling role of nitromethane. Collectively, these spectra demonstrate that immersion in PMA leads to oxidative doping of P3HT to a limited depth. Furthermore, an analysis of the atomic composition at the surface of PMA-im-P3HT films also reveals that Mo is ca. 4 times more abundant than S. Considering that the area ratio of oxidized P3HT is 35% at the surface of the film, this implies that ca. 12 Mo atoms yield an oxidized S atom. Hence,

to first approximation a single PMA molecule is sufficient to produce an oxidized thiophene in P3HT.

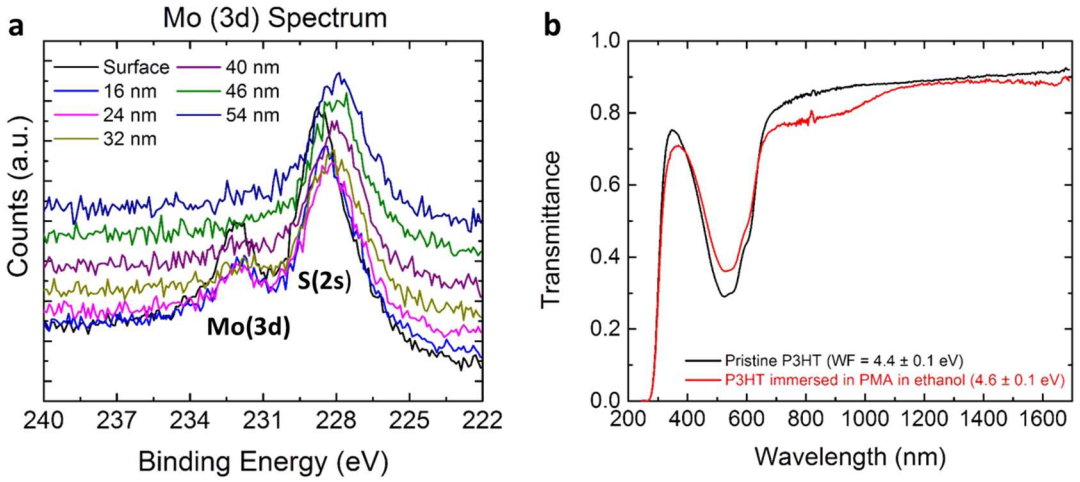

Figure 4-14 a, Depth profile XPS of a 50 nm-thick P3HT film immersed in a 0.5 M PMA solution in ethanol for 30 min at the Mo(3d) binding energies showing a very weak signature of Mo(3d) when compared with films immersed in PMA solutions in nitromethane as shown in Figure 2 in the main text. **b,** Transmittance and WF of the P3HT film after immersion.

4.2.4 Photo-oxidative Stability

Next, we investigated the stability of PMA-im-P3HT films. First, P3HT and PMA-im-P3HT films were continuously illuminated in air for 19 h using a Xenon lamp through a NIR filter. Figure 4-15 displays the absorptance spectrum of the films before and after continuous illumination in air, which reveal the complete photo-oxidation of P3HT films in contrast with the much improved photo-oxidation resilience of PMA-im-P3HT films; the amplitude of the polaron bands decreases significantly less than that of the main π–π* absorption bands, suggesting that the photo-oxidation of the thiophene groups in P3HT is indeed hindered by PMA. The temporal evolution of the normalized absorbed power

reveals that the overall rate of photo-oxidation of PMA-im-P3HT films is decreased by 2 to 3 times compared to that of P3HT films (inset of Figure 4-15).

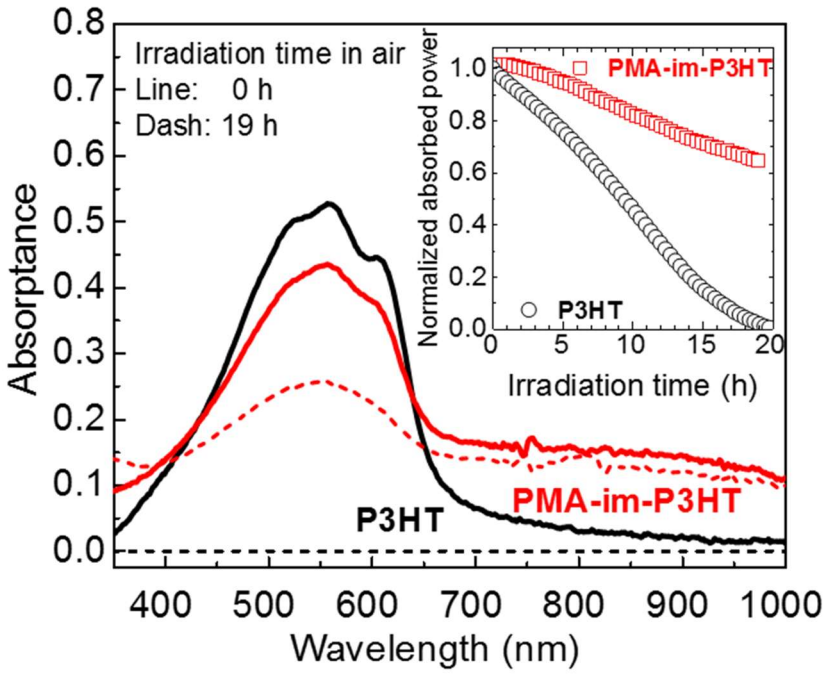

Figure 4-15 Absorptance of P3HT and PMA-im-P3HT films (immersed in 0.5 M PMA nitromethane for 30 min.) before and after 19 h of light exposure in air; inset shows the temporal dependence of the normalized absorbed power.

Furthermore, even in PCDTBT (Figure 4-16), a polymer that is more resistive to photo-oxidation than P3HT, PMA-im-PCDTBT films also display improved photo-oxidation stability over pristine films. The improved photo-oxidation resilience of PMA-im-polymer films could therefore lead to organic optoelectronic devices with longer lifetimes.

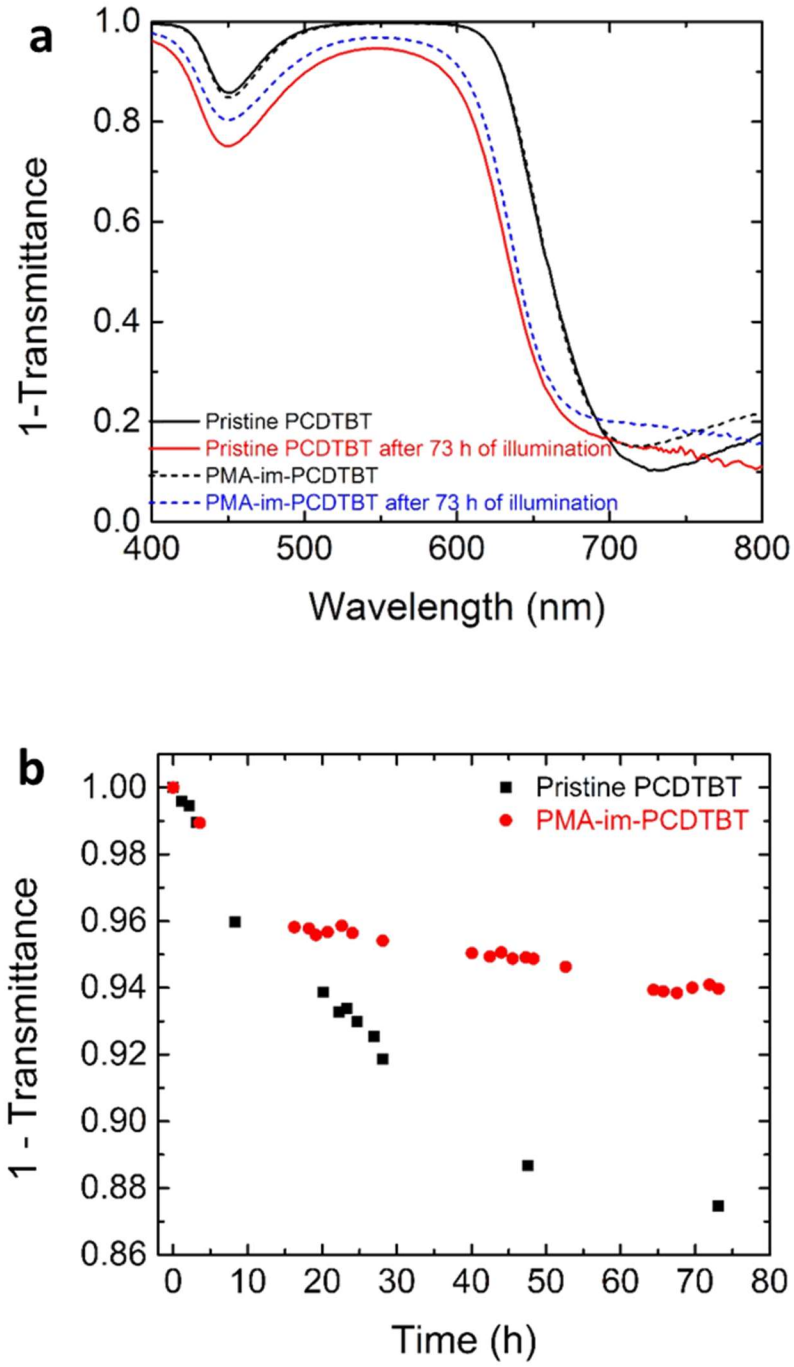

Figure 4-16 a, 1 – Transmittance of a 300 nm-thick pristine and PMA-im-PCDTBT film in 0.5 M PMA nitromethane solution before and after 73 h of illumination under a Xenon lamp. **b,** 1 – Transmittance as a function of time under illumination of a pristine and PMA-im-PCDTBT film.

4.2.5 Insolubility and Reversibility

An investigation of the solubility of PMA-im-P3HT films in chlorobenzene, the processing solvent of P3HT, revealed it was significantly reduced to the point that it is possible to rinse the film without washing it away as seen from the transmittance and WF measurements in Figure 4-17 and Table 4-1. Furthermore, the optical and electrical properties of P3HT can be recovered after immersing PMA-im-P3HT films in hydrazine hydrate for 30 min (Figure 4-17).

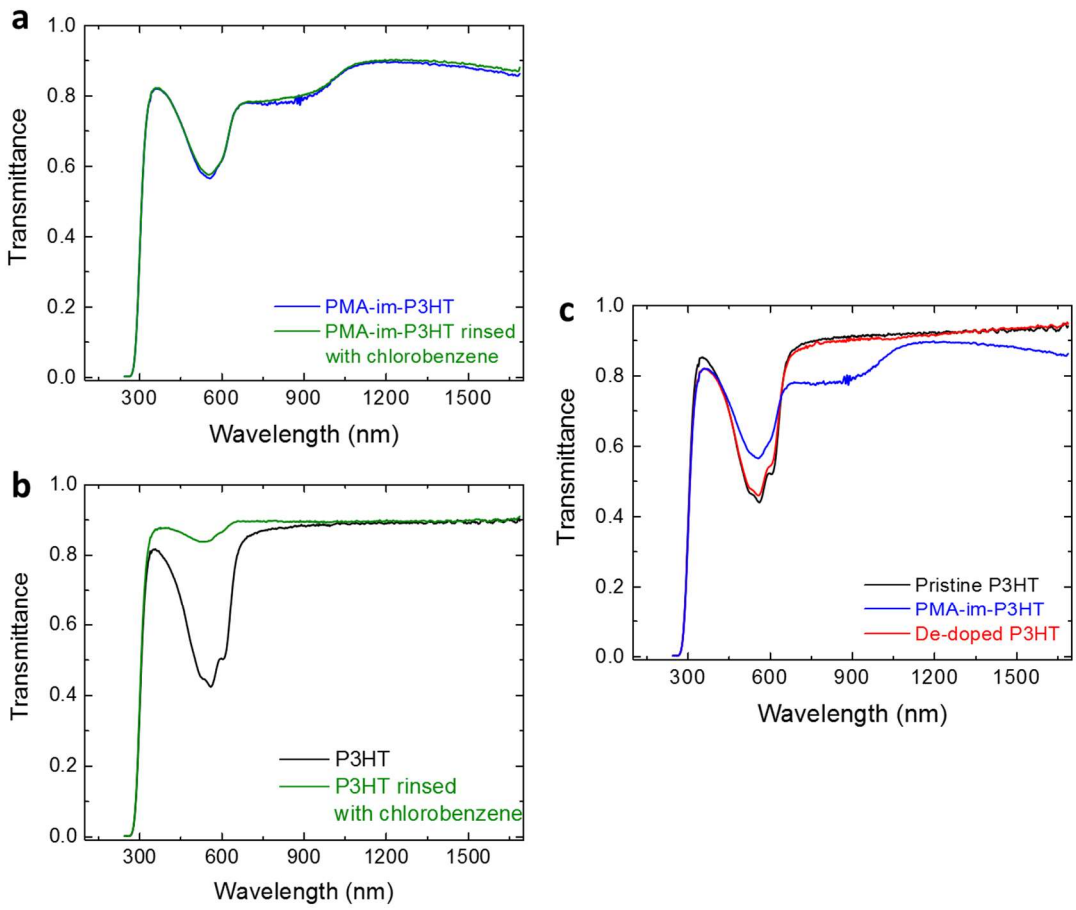

Figure 4-17 a, Transmittance data of a 30 nm-thick P3HT film immersed in 0.5 M PMA nitromethane solution for 30 min and the PMA-im-P3HT film after rinsing with the processing solvent, chlorobenzene. **b,** Transmittance data of a pristine P3HT film, PMA-im-P3HT film, and a PMA-im-P3HT film treated with a solution of 0.5 M hydrazine hydrate. **c,** Transmittance data of a pristine P3HT film and a pristine P3HT film rinsed with the processing solvent, chlorobenzene.

Table 4-1 Work function values of all films.

Film Description	WF (eV)
Pristine P3HT	4.4 ± 0.1
PMA-im-P3HT (30 min)	4.8 ± 0.1
PMA-im-P3HT Rinsed with Chlorobenzene	4.8 ± 0.1
De-doped P3HT	4.4 ± 0.1

4.2.6 Electrical Properties

Next, we studied the electrical properties of 210 nm-thick P3HT films after immersion in 50 μM and 0.5 M PMA nitromethane solutions using the transmission line method to measure the sheet resistance (Figure 4-18) as a function of immersion time.

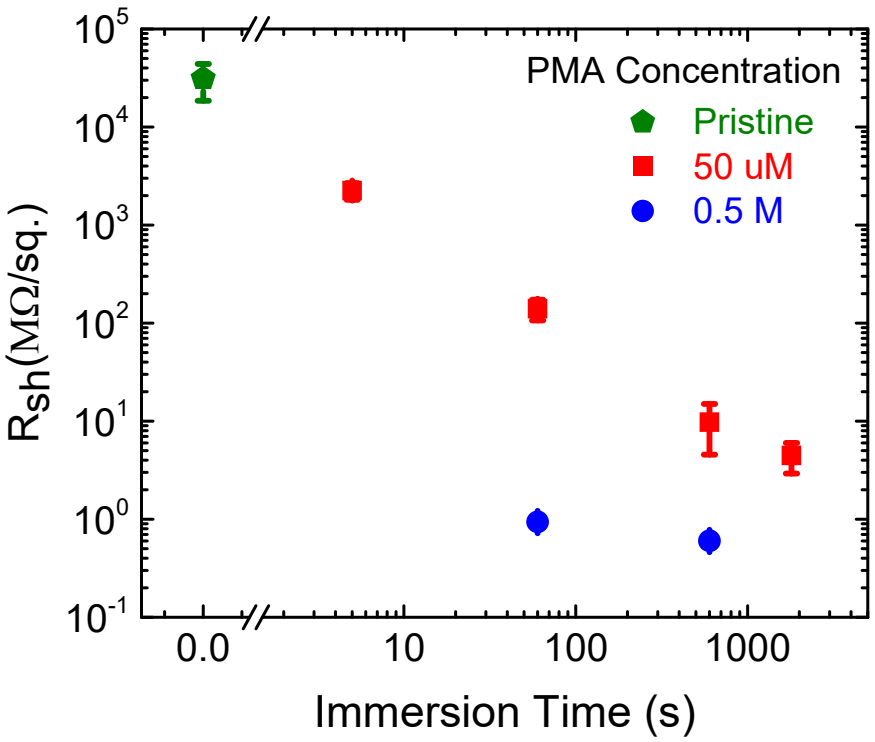

Figure 4-18 Sheet resistance of a 210-nm thick PMA-im-P3HT layers immersed in 50 µM or 0.5 M PMA nitromethane solution for varying immersion times. Error bars for sheet resistance represent statistical variations from TLM measurements across two arrays of metal contacts of each width (2400 µm and 1200 µm).

The degree of electrical doping varies with immersion time and concentration (Figure 4-3 and Figure 4-18). When immersed in a 50 µM PMA nitromethane solution, the sheet resistance of PMA-im-P3HT films decreases monotonically by ca. 4 orders of magnitude with increasing immersion time from 30 ± 10 GΩ sq.$^{-1}$, as measured for an intrinsic P3HT layer, to 4 ± 2 MΩ sq.$^{-1}$ after 30 min. Similar measurements conducted for a 30 nm- thick P3HT layer immersed in a 0.5 M PMA nitromethane solution revealed sheet resistance values down to ca. 0.13 ± 0.01 MΩ sq.$^{-1}$ from Figure 4-19.

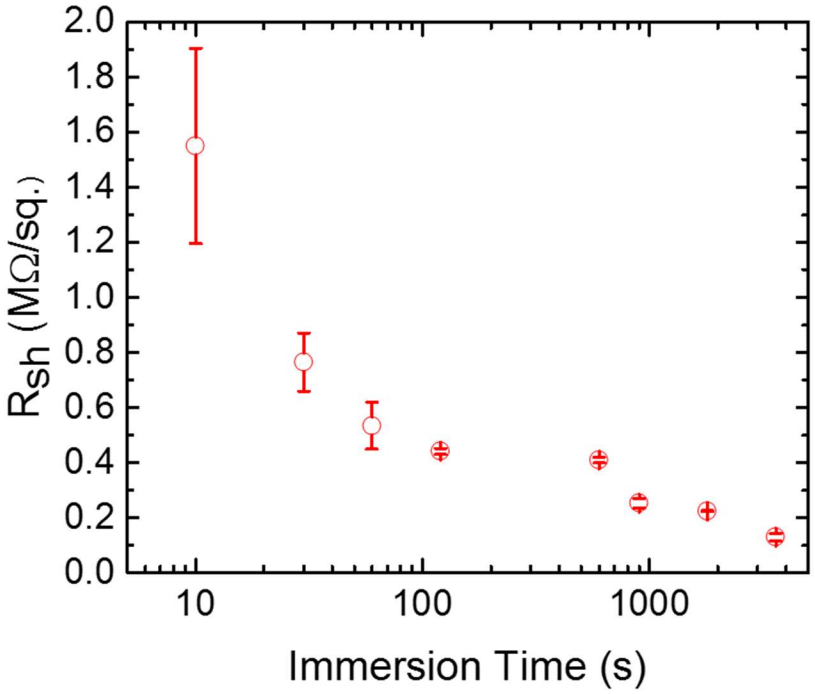

Figure 4-19 Sheet resistances for a 30 nm-thick PMA-im-P3HT film in 0.5 M PMA nitromethane solution. Error bars for sheet resistance represent statistical variations from TLM measurements across two arrays of metal contacts of each width (2400 µm and 1200 µm).

Using a decay constant of 11 ± 1 nm, extracted from XPS and ellipsometry measurements, maximum conductivity values of 7.0 ± 0.5 S cm^{-1} can be derived for such doped layers. In contrast, a pristine P3HT layer displays a conductivity value of 1 ± 1 µS cm^{-1}. These results demonstrate that PMA electrically dopes P3HT films.

Kelvin probe measurements were then used to determine variations in the work function (WF) of PMA-im-P3HT films. Figure 4-20 shows an increase of the WF value from 4.4 eV, in P3HT, to 4.8 eV after 5 s of immersion and remains constant for immersion times up to 30 min.

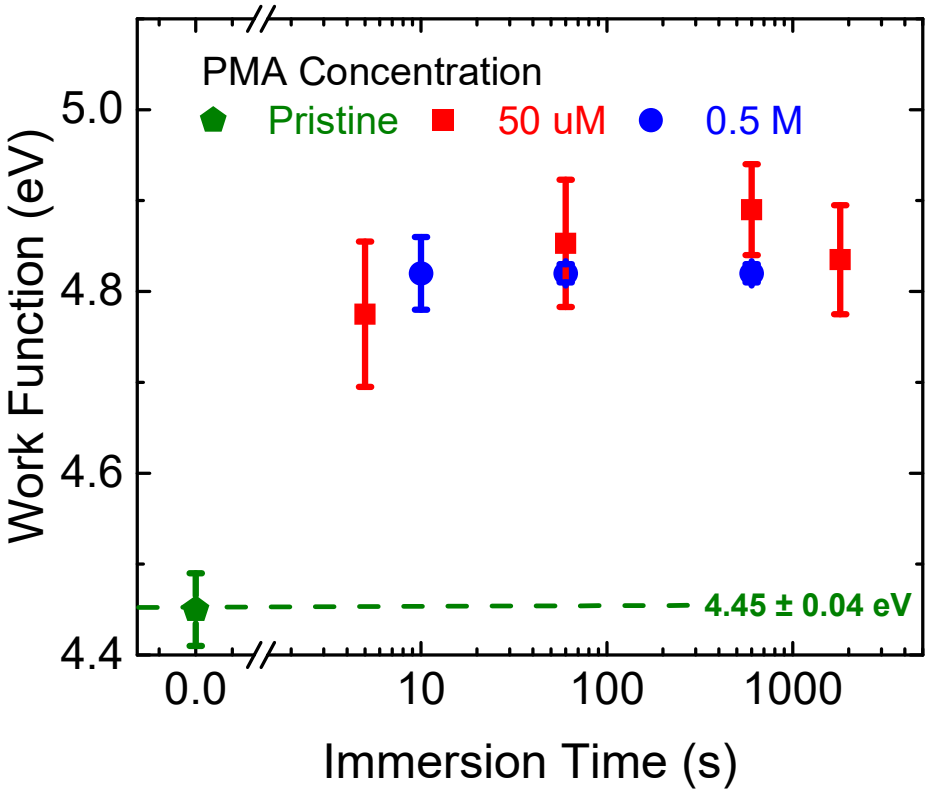

Figure 4-20 WF values of a 210-nm thick PMA-im-P3HT layers immersed in 50 µM or 0.5 M PMA nitromethane solution for varying immersion times. Error bars for WF measurements (bottom) represent statistical variations over a minimum of four spots on each film.

Similarly, the 30 nm-thick P3HT films from Figure 4-19 also show an increase in the WF of 0.4 eV and remain constant up to 60 min of immersion as seen in Table 4-2.

Table 4-2 Work function measurements for a 30 nm-thick PMA-im-P3HT film in 0.5 M PMA nitromethane solution.

P3HT Sample	**WF (eV)**
Pristine	4.4 ± 0.1

PMA-im-P3HT (10 s)	4.8 ± 0.1
PMA-im-P3HT (30 min)	4.8 ± 0.1
PMA-im-P3HT (60 min)	4.8 ± 0.1

The change of WF of PMA-im-P3HT films is consistent with a shift in the Fermi level energy closer to the HOMO band of P3HT upon *p*-type electrical doping. Similar shifts, albeit smaller in magnitude (ΔWF = 0.2 eV), of the Fermi level are also observed in PTA-im-P3HT films (Figure 4-4). It should be noted that if we neglect the presence of surface dipoles and assume that the work function values reflect only the Fermi level energy in the semiconductor, then an increase of the work function value by 0.4 eV would reflect an increase of carrier density of ca. 10^6 cm^{-3}, which at the surface of the film would be consistent with changes of conductivity in the volume observed between pristine P3HT and PMA-im-P3HT films. Since the WF remains nearly independent of immersion time and PMA concentration, Figure 4-20 suggests that the doping at the surface rapidly saturates, in agreement with the XPS studies. At low PMA concentrations, changes in sheet resistance and transmittance observed as a function of immersion time and concentration can be attributed to the penetration of the dopant into the film down to a limited depth, in agreement with the ellipsometry results. At higher PMA concentrations the penetration depth and sheet resistance saturate.

4.2.7 Applicability

The general nature of this method can be extended to small-molecule films (Figure 4-21) and other polymers.

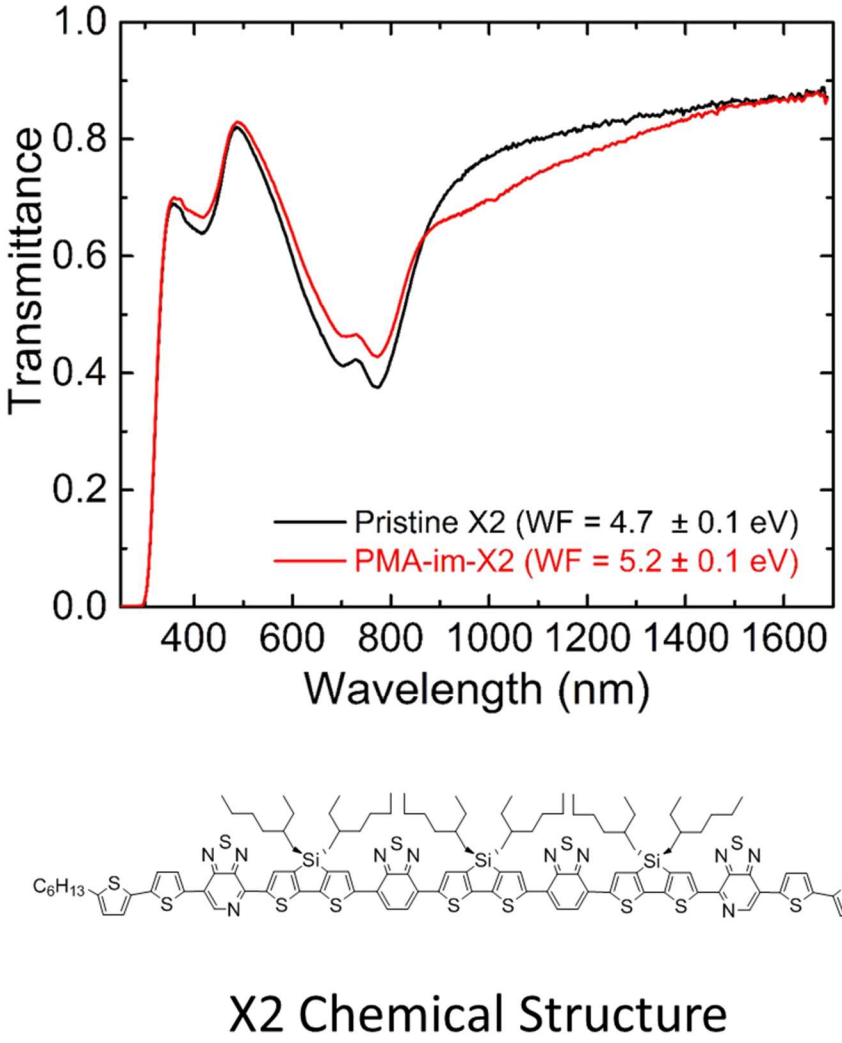

Figure 4-21 Chemical structure of the small molecule X2, transmittance of pristine X2 films and X2 films immersed into a 0.5 M PMA nitromethane solution for 5 min. Work function values as measured by a Kelvin probe are shown in the legend.

Indeed, we have observed spectroscopic evidence of PMA-doping in acene derivatives (e.g. 6,13-bis(triisopropylsilylethynyl) pentacene (TIPS-pentacene) (Sigma Aldrich) and rubrene (Sigma Aldrich)) and triarylamine derivatives (e.g. poly(triarylamine) (PTAA) (Sigma Aldrich) and poly(acrylic tetraphenyldiaminobiphenol) (PATPD) (synthesized in

Marder's group). Of particular relevance, evidence of PMA-doping by post-process immersion in a PMA nitromethane solution has also been confirmed in donor-acceptor polymers, in particular those relevant for OPVs and OFETs, such as PIPCP, PTB7, and PBDTTT-C, and PffBT4T-2OD (Figure 4-22).

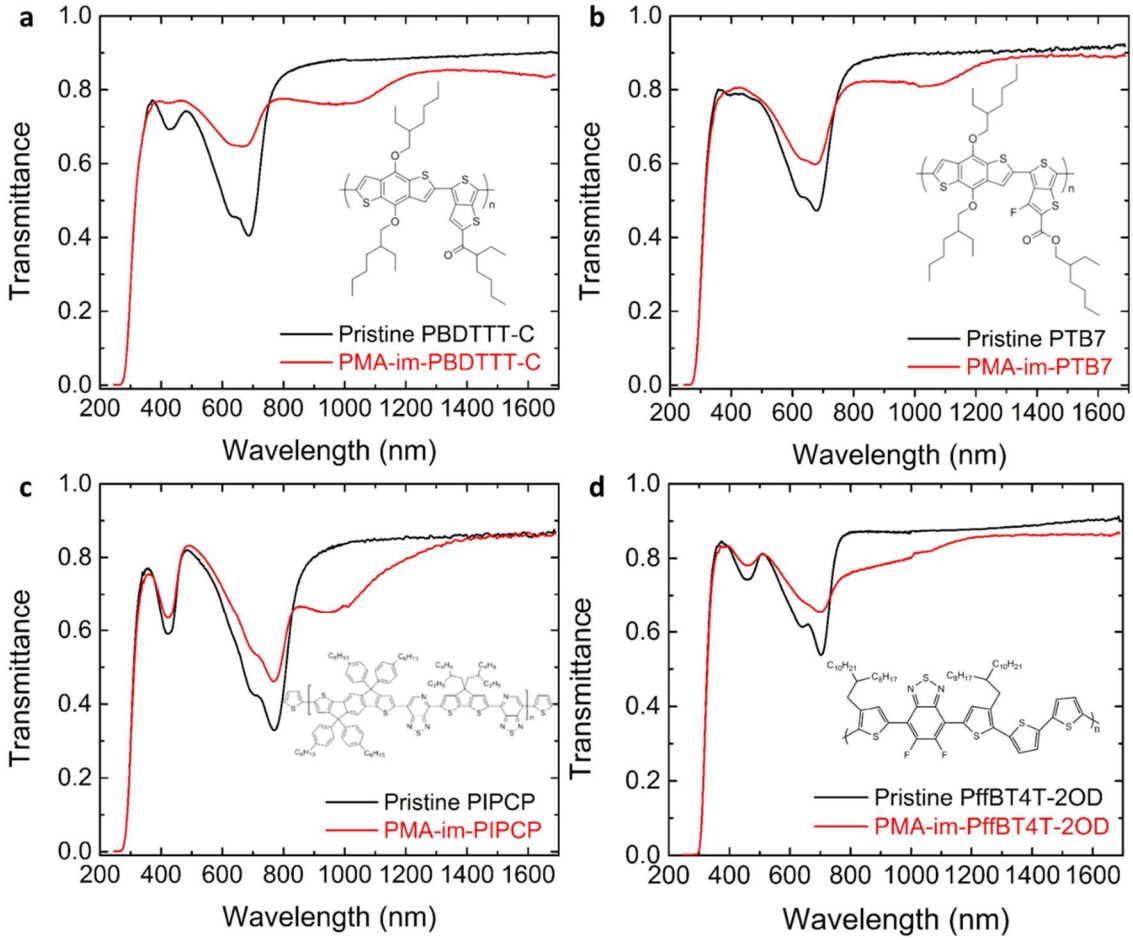

Figure 4-22 Transmittance data of a polymer films immersed in 0.5 M PMA nitromethane solution for 10 min and pristine a, PBDTTT-C, b, PTB7, c, PIPCP, and d, PffBT4T-2OD films.

Electrical doping of these polymers is again confirmed with measurements of the WF after immersion into a 0.5 M PMA solution for 10 min in Table 4-3.

Table 4-3 Work function values of doped polymer films from Figure 4-22.

Polymer Film	WF (eV) (Pristine)	WF (eV) (Doped)
PBDTTT-C	4.8 ± 0.1	5.1 ± 0.1
PTB7	4.8 ± 0.1	5.0 ± 0.1
PIPCP	4.8 ± 0.1	5.1 ± 0.1
PffBT4T-2OD	4.8 ± 0.1	5.3 ± 0.1

4.3 Summary

In summary, we have presented a solution-based approach for electrical p-doping of films of donor-like conjugated organic semiconductors and their blends with acceptors over a limited depth by post-process immersion in polyoxometalate (PMA and PTA) solutions in nitromethane. PMA-doped films show increased electrical conductivity and work function, reduced solubility in the processing solvent, and improved photo-oxidation stability in air. We have shown that this method is applicable to a wide range of relevant donor polymers and their blends with fullerene acceptors. These results indicate that this technique has the potential to be implemented in a multitude of device platforms.

CHAPTER 5

Single-Layer Organic Photovoltaic Devices

In this chapter, the application of the solution-based electrical doping technique previously described is shown in OPV devices. This method significantly reduces the fabrication complexity and eliminates some energy intensive vacuum deposition steps. In contrast to previous attempts, it will also be shown that direct doping of the photoactive layer in an OPV device does not impact the recombination mechanisms, device performance, or device stability.

5.1 Introduction

Electrical doping of organic semiconductors using vacuum-based techniques already plays a central role in the design and fabrication of high performance organic electronic devices [66, 67, 94-97], but the fabrication of multilayer devices with doped layers using vacuum-free solution-based processing techniques remains a major challenge. This is in part because the underlying doping mechanisms of organic semiconductors are poorly understood, and their low doping efficiencies necessitate a high dopant concentration, causing a high density of traps that is detrimental to their mobility and conductivity [56, 98]. Furthermore, controlled and stable electrical doping requires the addition and immobilization of strong oxidizing or reducing molecules in specific regions of a device. Despite challenges, a solution-based method of electrical doping is particularly desirable for organic photovoltaics because Fermi level engineering could facilitate charge extraction and may eliminate the need for the use of expensive metals. In turn, such

advances could have a significant impact on reducing OPV's cost-of-electricity and energy-payback times [23].

Several approaches have been implemented to achieve low-resistance contacts for hole-collection. Previously, layers of donor polymers such as P3HT p-doped with molybdenum tris[1-(methoxycarbonyl)-2-(trifluoromethyl)-ethane-1,2-dithiolene] ($Mo(tfd\text{-}CO_2Me)_3$) have been used as a hole-collecting layer by transfer laminating onto inverted OPV device structures [52, 53]. Other previously reported attempts used spin-coated layers of PMA and PTA processed from IPA to behave as standalone hole-collecting interlayers in both conventional and inverted OPV architectures [73-76]. However, it was suggested, through measurements of the XPS spectrum of the solution-processed POMs, that either no doping or only slight interfacial *p*-type doping was present in these devices [75].

Here, we demonstrate the application of oxidative (*p*-type) doping over a limited depth by post-processing immersion of films of donor-like conjugated organic semiconductors and their blends with acceptors into a PMA solution in nitromethane. We show that this PMA doping method enables efficient *single layer* OPV devices processed at room temperature and OPVs that display stable shelf lifetime at 60° C for at least 280 h. Here, the terminology single layer is adopted because the functions of hole-and electron-collection are contained in the photoactive layer and the electrodes have no other function than to provide low-sheet-resistance pathways for the photogenerated current [62, 63, 99, 100].

5.2 Results and Discussion

We have seen that P3HT films doped with PMA improve the lateral conductivity and also shifts the Fermi level energy closer to the ionization potential of the polymer. This indicates that PMA doped P3HT has the potential serve the same electrical function as a hole-collecting layer. In the context of OPV devices, efficient hole-collection (injection) is necessary for optimal device performance. To determine whether this method can be used to control the vertical conductivity and injection (collection), we fabricated hole-only devices with P3HT immersed in PMA for various times. Figure 5-1 shows that devices with a pristine P3HT layer display the expected current-density vs. voltage (*J-V*) characteristics of a diode due to the large energy mismatch between the WF of Ag and the ionization energy of P3HT. However, devices with PMA-doped P3HT layers display the *J-V* characteristics of a resistor, demonstrating that charge injection and collection is significantly improved even with the use of an Ag electrode.

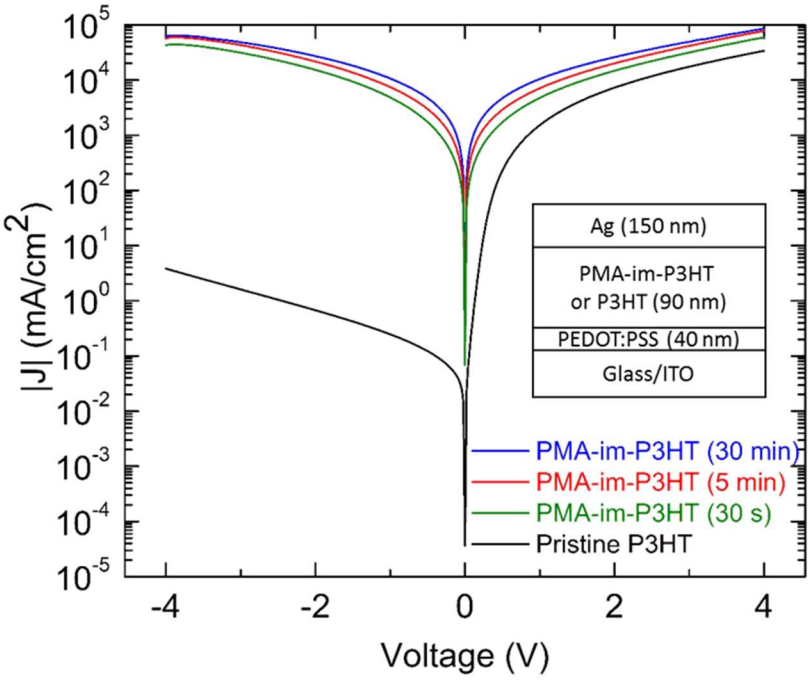

Figure 5-1 *J–V* characteristics of the hole-only devices showing improved hole injection with increased immersion time.

Turning to the realization of OPV devices implementing doped P3HT as a separate hole-collecting layer, we investigated the performance of devices with a transfer laminated layer of P3HT immersed in PMA nitromethane solution for 5 and 15 min (Figure 5-2). The results are comparable to the reference device with the MoO_3 hole-collecting layer as seen in the Table A-1 of the appendix.

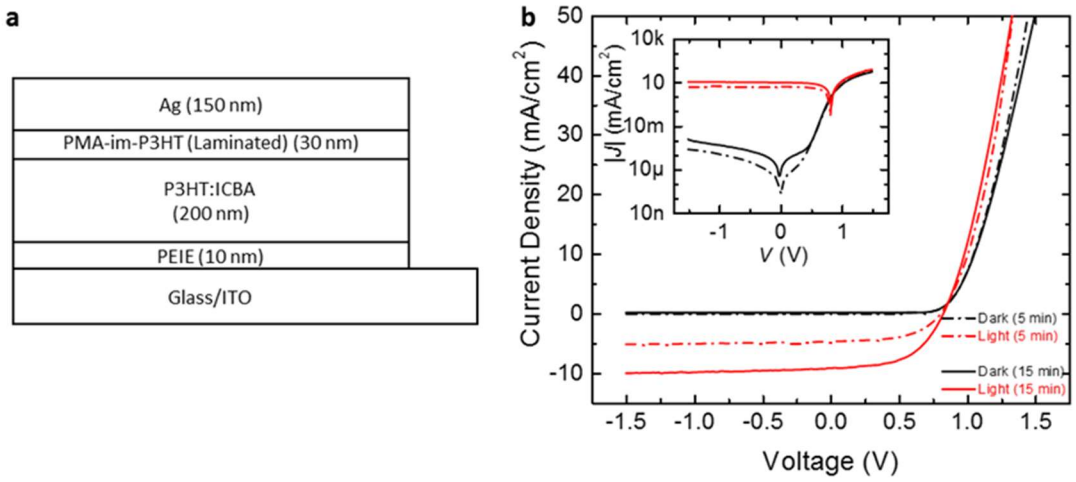

Figure 5-2 a,b, Device structure and *J–V* characteristics of devices with a 200 nm active layer and a 30 nm transfer-laminated P3HT buffer layer doped for 5 or 15 min in a 0.5 M PMA nitromethane solution with PCE up to 4.1 ± 0.3%. The inset shows the *J–V* characteristics on a semilogarithmic scale. The full performance characteristics of the devices are shown in Table 5-1.

5.2.1 PMA Doped Donor-Acceptor Blends

More importantly, this method also enables the direct electrical doping to a limited depth of donor-acceptor blend films used as photoactive layers in OPVs (Figure 5-3).

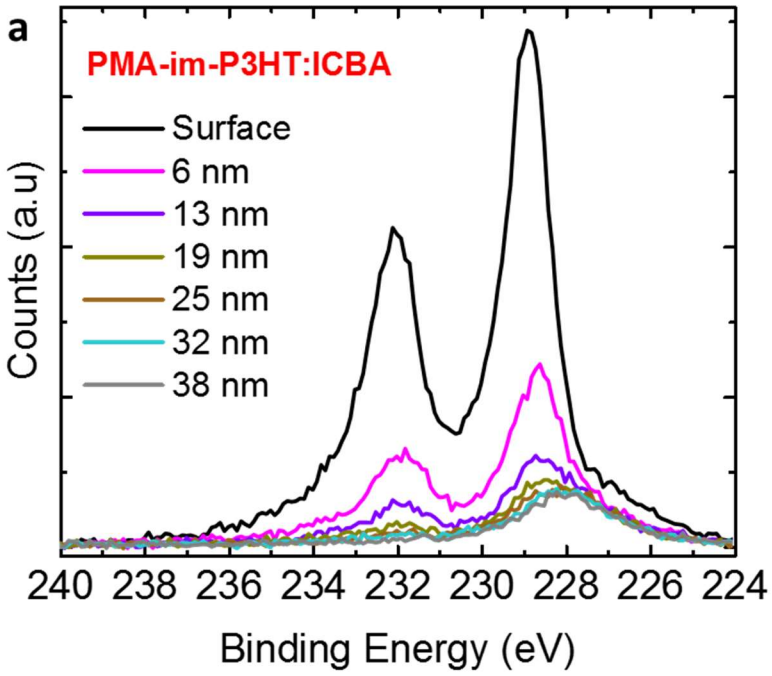

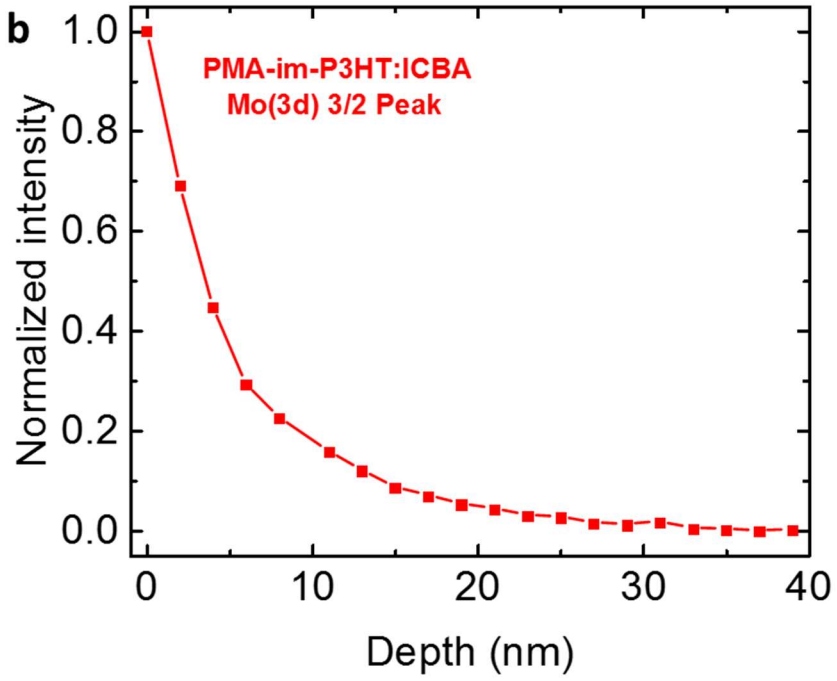

Figure 5-3 a, Depth profile of a 200 nm P3HT:ICBA film immersed in a 0.5 M PMA nitromethane solution for 10 min at the Mo(3d) binding energies showing penetration of molybdenum into the bulk to a depth of approximately 40 nm, with only a small S(2s) peak remaining, seen in pristine P3HT in Fig. 2d, after 40 nm. **b,** Normalized intensity of the Mo($3d_{3/2}$) peak as a function of depth etched into the PMA-im-P3HT:ICBA film.

Neat $PC_{61}BM$ films immersed in a 0.5 M PMA nitromethane solution revealed no evidence of doping and very poor solubility in nitromethane (Figure 5-4).

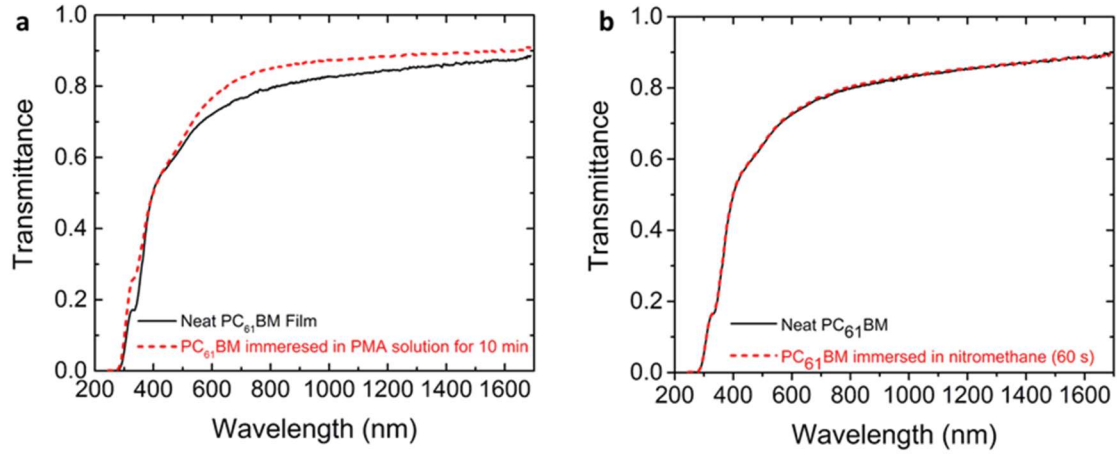

Figure 5-4 . **a,** Transmittance of a neat film of $PC_{61}BM$, and a $PC_{61}BM$ film immersed into a solution of 0.5 M PMA in nitromethane for 10 min. **b,** Transmittance of a neat film of $PC_{61}BM$, and a $PC_{61}BM$ film immersed into pure nitromethane for 60 s.

5.2.2 OPV Devices with Directly Doped Photoactive Layers

Consequently, we investigated the performance of OPVs immersed in 0.5 M PMA nitromethane solution for 60 s having a 500 nm-thick PMA-im-P3HT:ICBA photoactive layer with ITO/PEIE electron-collecting bottom-electrode and Ag top-electrode. We fabricated reference OPVs where the photoactive layer was not immersed into a PMA nitromethane solution and where MoO_3 (WF values of 5.5–6.9 eV) [57, 101-105] was used as a hole-collecting interlayer and Ag as an electrode. The performance parameters of PMA-doped and reference OPVs in the dark and under simulated AM 1.5G solar illumination were found comparable (Figure 5-5 and Table 5-1).

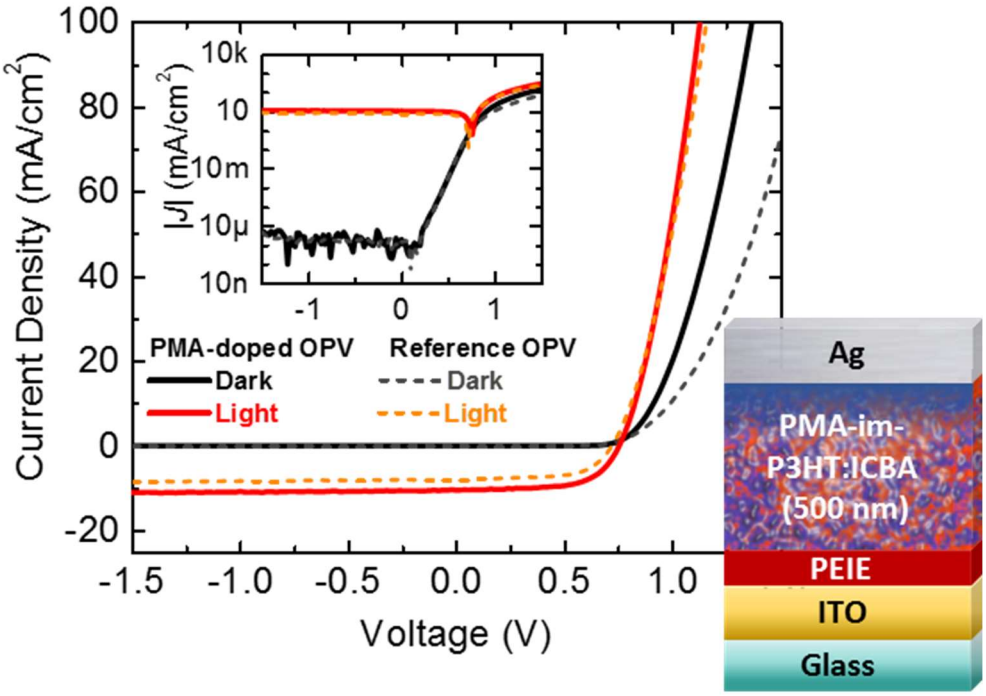

Figure 5-5 *J–V* characteristics of PMA-doped and reference OPVs having the structure: ITO/PEIE/PMA-im-P3HT:ICBA/Ag and ITO/PEIE/P3HT:ICBA/MoO_3/Ag, respectively. Insets shows the *J-V* characteristics on a semilogarithmic scale.

To rule out that Ag alone could provide efficient hole-collection, we also fabricated OPVs with Ag top electrodes deposited directly on a pristine photoactive layer. These devices showed poor rectification and average PCE values of 0.1 ± 0.1% (Appendix Table A-1). Furthermore, EQEs and the irradiance-dependent response of PMA-doped OPVs and reference OPVs were also found to be comparable (Figure 5-6 and Figure 5-7).

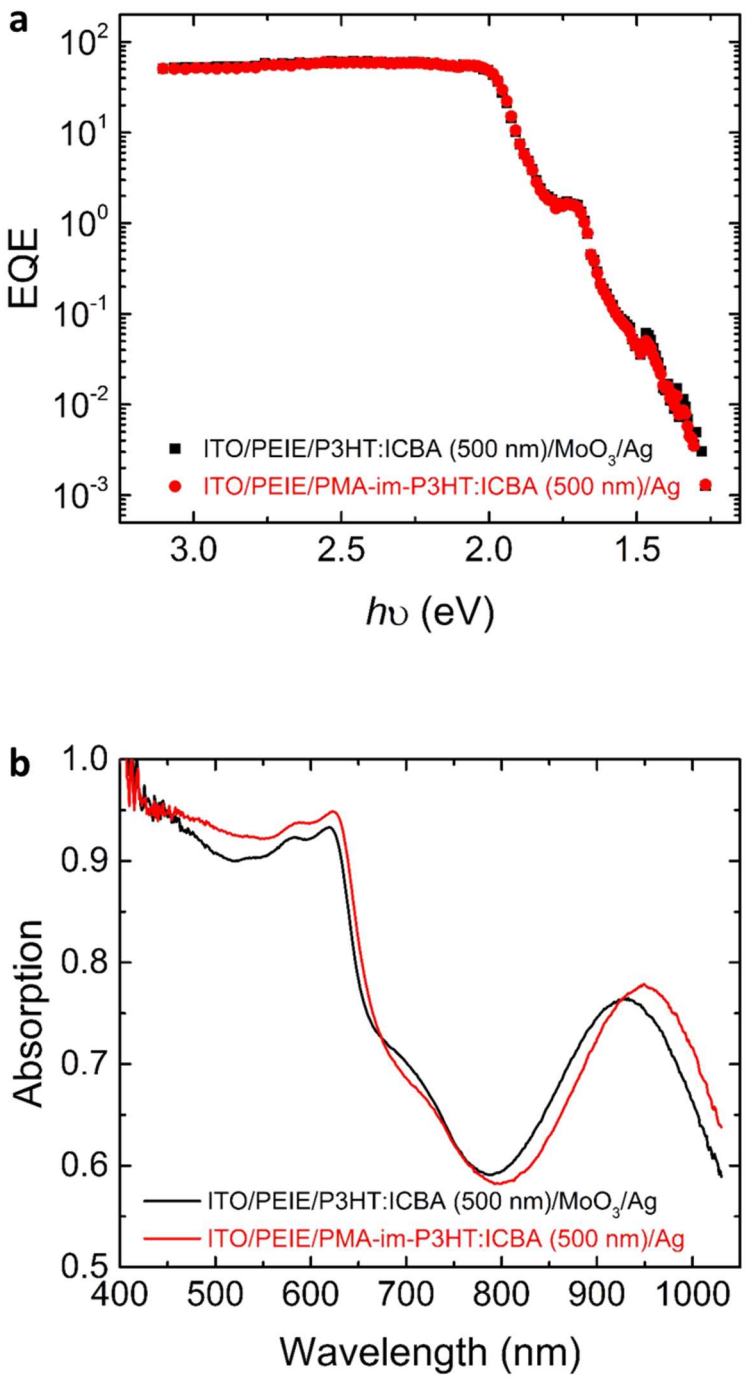

Figure 5-6 a, EQE and **b,** absorption measured in reflection of ITO/PEIE/P3HT:ICBA (500 nm)/MoO_3/Ag reference devices and ITO/PEIE/PMA-im-P3HT:ICBA (500 nm)/Ag doped devices (immersion in 0.5 M PMA nitromethane solution for 60 s).

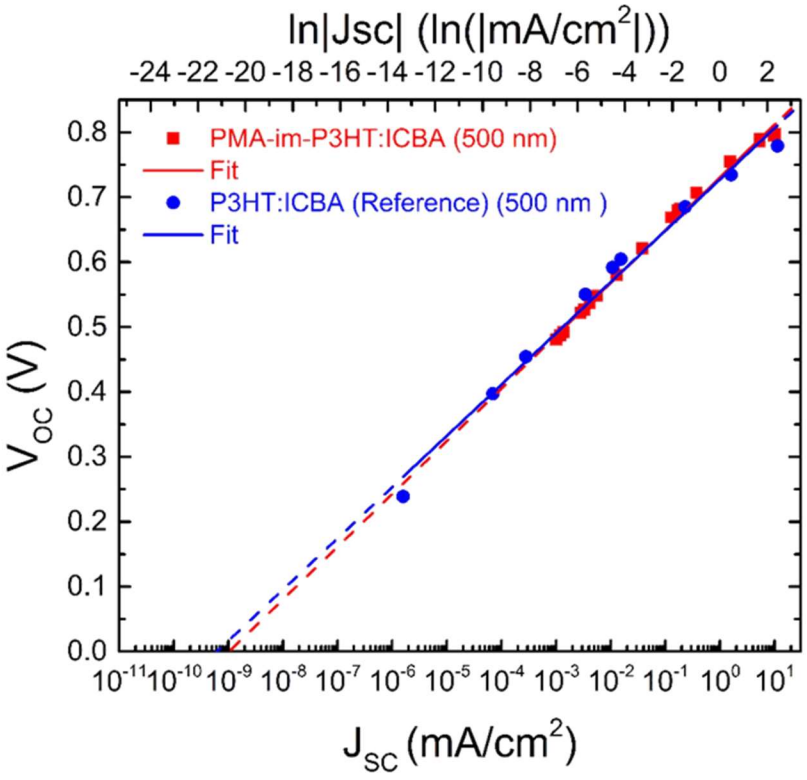

Figure 5-7 V_{OC} as a function of J_{SC} for variable irradiance for ITO/PEIE/P3HT:ICBA (500 nm)/MoO_3/Ag reference devices and ITO/PEIE/PMA-im-P3HT:ICBA (500 nm)/Ag doped devices (immersion in 0.5 M PMA nitromethane solution for 60 s).

In addition, PMA-doped OPVs with Al electrodes (with an expected WF value of 4.3 eV compared to that of Ag (4.7 eV)) [106, 107] displayed performance parameters comparable to those of PMA-doped OPVs with Ag top electrodes and of reference OPVs (Table 5-1 and Figure 5-8).

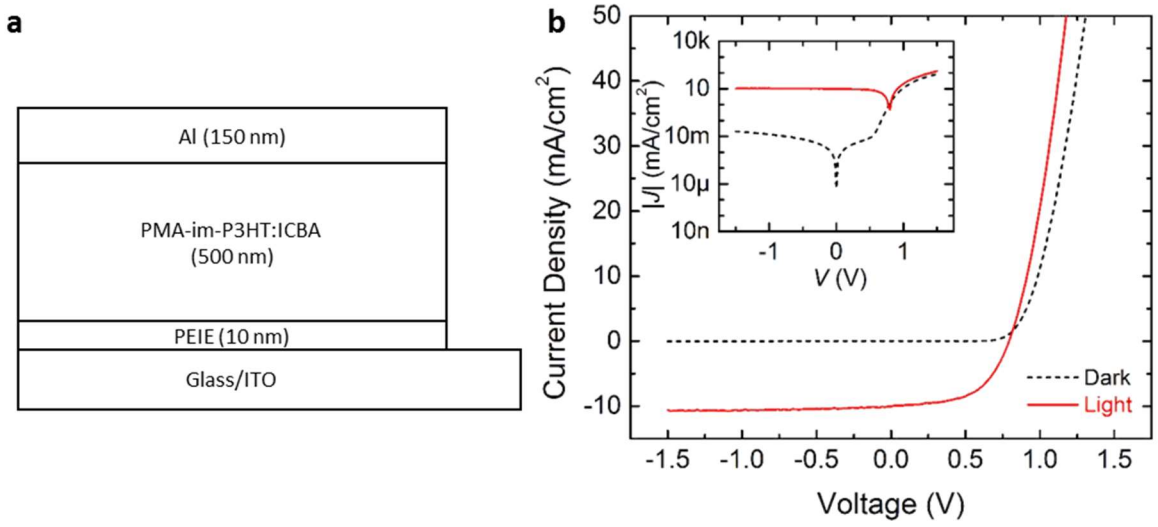

Figure 5-8 a, Device structure and **b,** *J–V* characteristics of device with 500 nm PMA-im-active layer and Al top contacts (immersion in 0.5 M PMA nitromethane solution for 60 s). The inset shows the *J–V* characteristics on a semilogarithmic scale.

Therefore, PMA-doping of the photoactive layer allows for the use of cheaper metals having a wider range of WF values.

5.2.3 Shelf Lifetime

To investigate the diffusivity of PMA in a completed OPV device, we studied the shelf lifetime of devices with a PMA-im-P3HT:ICBA active layer at 60 °C inside an N_2-filled glove box. The performance of PMA-doped OPV devices under illumination does not display evident signs of degradation over a period of 282 h (Figure 5-9).

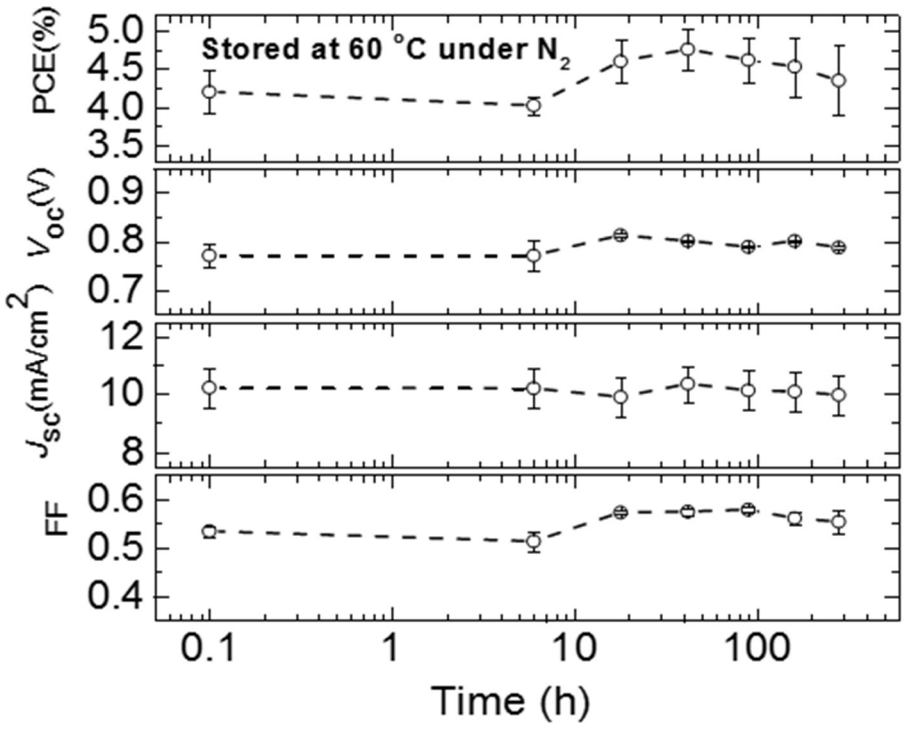

Figure 5-9 Temporal evolution of photovoltaic parameters for 500 nm-thick PMA-im-P3HT:ICBA OPV kept in N_2-filled glove box at 60 °C up to 282 h.

These results suggest that while PMA shows sufficient penetration in the polymer films during doping by immersion, it also displays little, if any, diffusivity post fabrication and provides a robust method to create a stable hole-collecting contact.

5.2.4 Two-Layer OPV Devices With High Efficiency Polymers

To demonstrate that this method can be applied to thinner photoactive layers, we first demonstrated OPV devices having 200 nm-thick PMA-im-P3HT:ICBA photoactive layers using an ITO/PEIE electron-collecting electrode and an Ag top-electrode (Table 5-1 and Figure 5-10).

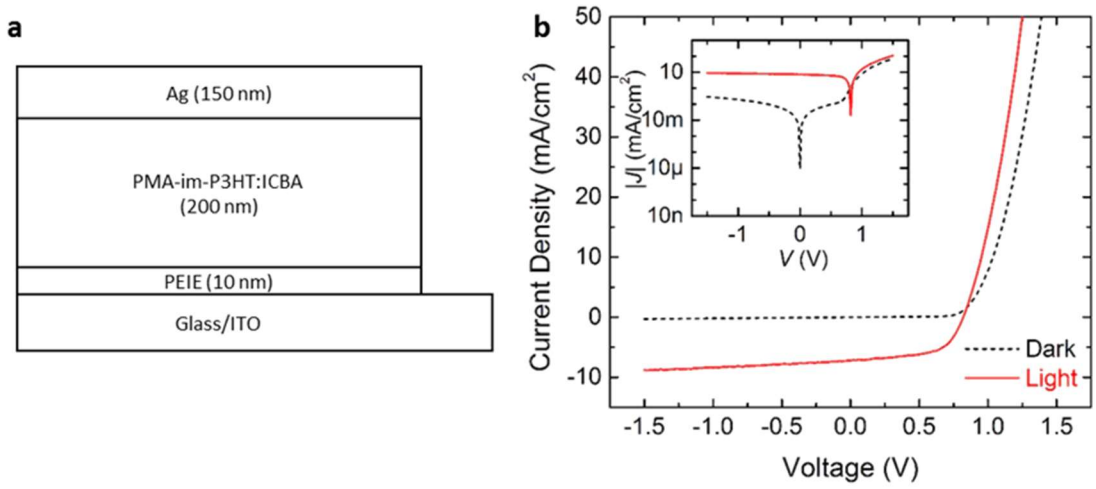

Figure 5-10 a, Device structure and **b,** *J–V* characteristics ITO/PEIE/PMA-im-P3HT:ICBA (200 nm)/Ag devices (immersion in 0.5 M PMA nitromethane solution for 60 s). The inset shows the *J–V* characteristics on a semilogarithmic scale.

To further show the versatility of this approach, we explored the use of a higher efficiency polymer PIPCP [87, 108]. PIPCP has been shown to have a low photon energy loss and therefore affords a high V_{OC} in OPVs using this donor. OPVs immersed in 0.05 M PMA nitromethane solution for 60 s having a 110 nm-thick PMA-im-PIPCP:$PC_{61}BM$ photoactive layer using a ITO/PEIE electron-collecting electrode and an Ag top-electrode were fabricated (Figure 5-11).

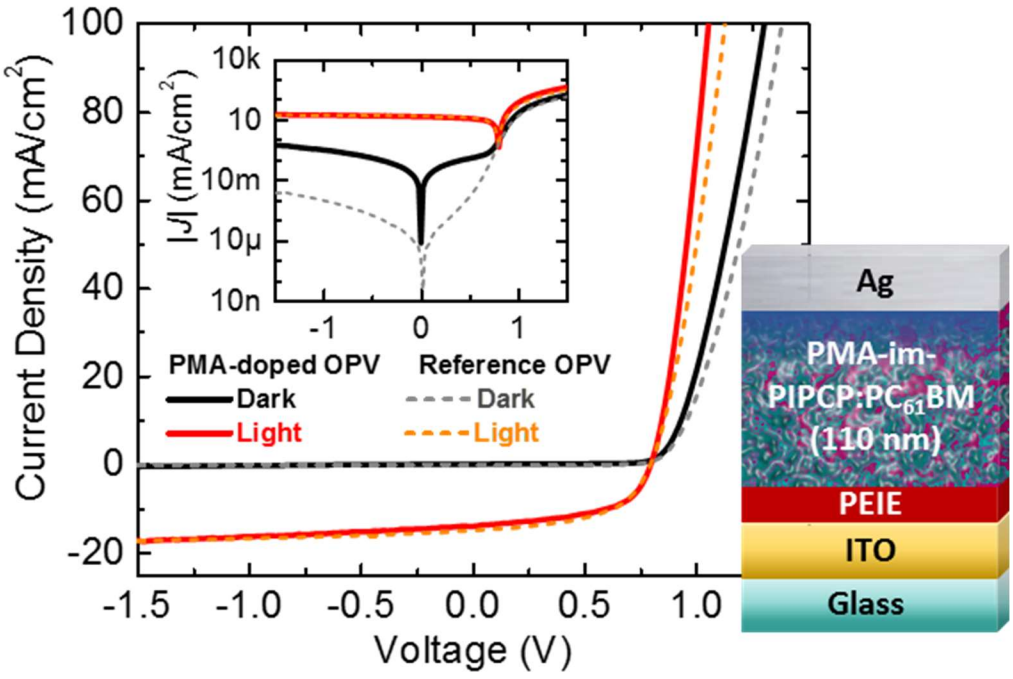

Figure 5-11 *J–V* characteristics of PMA-doped and reference OPVs having the structure: ITO/PEIE/PMA-im-PIPCP:$PC_{61}BM$/Ag and ITO/PEIE/PIPCP:$PC_{61}BM$/MoO_3/Ag, respectively. Insets shows the *J-V* characteristics on a semilogarithmic scale.

These devices had a comparable performance to the reference OPVs with a pristine 110 nm-thick PIPCP:$PC_{61}BM$ photoactive layer and MoO_3/Ag hole-collecting electrode (Table 5-1) and also to previous reports in the literature [87, 108]. Figure 5-12 further demonstrates that this approach can be extended to other donor polymers such as PffBT4T-2OD, OPVs immersed in 0.1 M PMA nitromethane solution for 60 s with a 230 nm –thick PMA-im-PffBT4T-2OD:$PC_{71}BM$ photoactive layer display a PCE = 7.8 ± 0.2%, with champion devices yielding a PCE of 8.4% (Table 5-1). As before, reference devices with an undoped photoactive layer and MoO_3/Ag electrodes show a comparable performance with an average PCE = 7.7 ± 0.1% (Table 5-1).

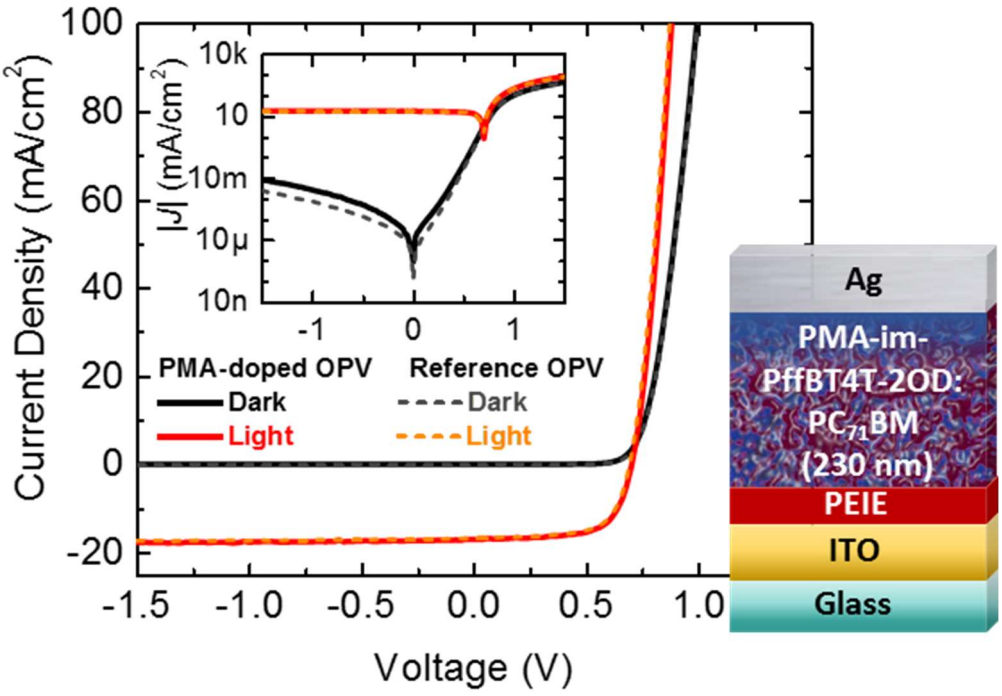

Figure 5-12 *J–V* characteristics of PMA-doped and reference OPVs having the structure: ITO/PEIE/PMA-im-PffBT4T-2OD:$PC_{71}BM$/Ag and ITO/PEIE/PffBT4T-2OD:$PC_{71}BM$ /MoO_3/Ag, respectively. Insets shows the *J-V* characteristics on a semilogarithmic scale.

The chemical structures of the donors and acceptors used in these OPVs are shown in Figure 5-13.

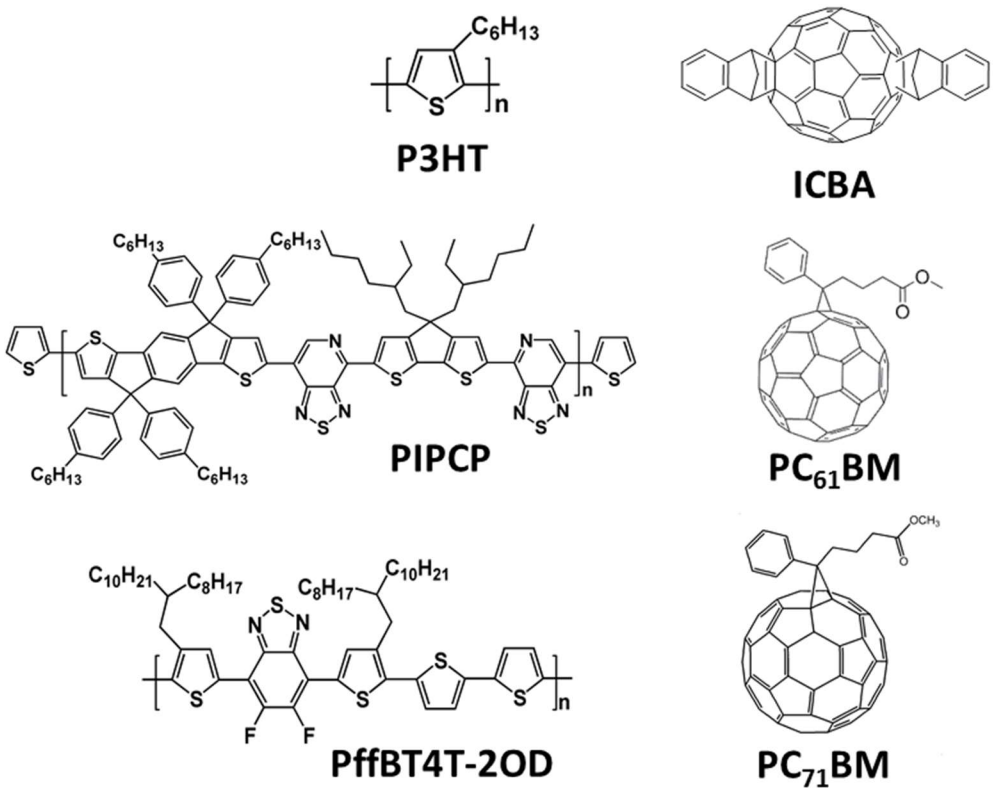

Figure 5-13 Chemical structures of donor polymers and acceptor fullerenes used in these OPVs.

5.2.5 Single-Layer OPV Devices

Finally, we demonstrate single-layer OPV devices by combining this method with spontaneous vertical phase separation of PEIE [62]. Single-layer OPVs were realized by a single spin-coating of a solution of the mixture PEIE:P3HT:ICBA onto ITO followed by PMA doping by post-process immersion and deposition of a top-electrode. Figure 5-14 shows that 500 nm-thick OPV devices with a single-layer of PMA-im-PEIE:P3HT:ICBA, yield a performance comparable to that of three-layer and two-layer OPVs discussed above (Table 5-1).

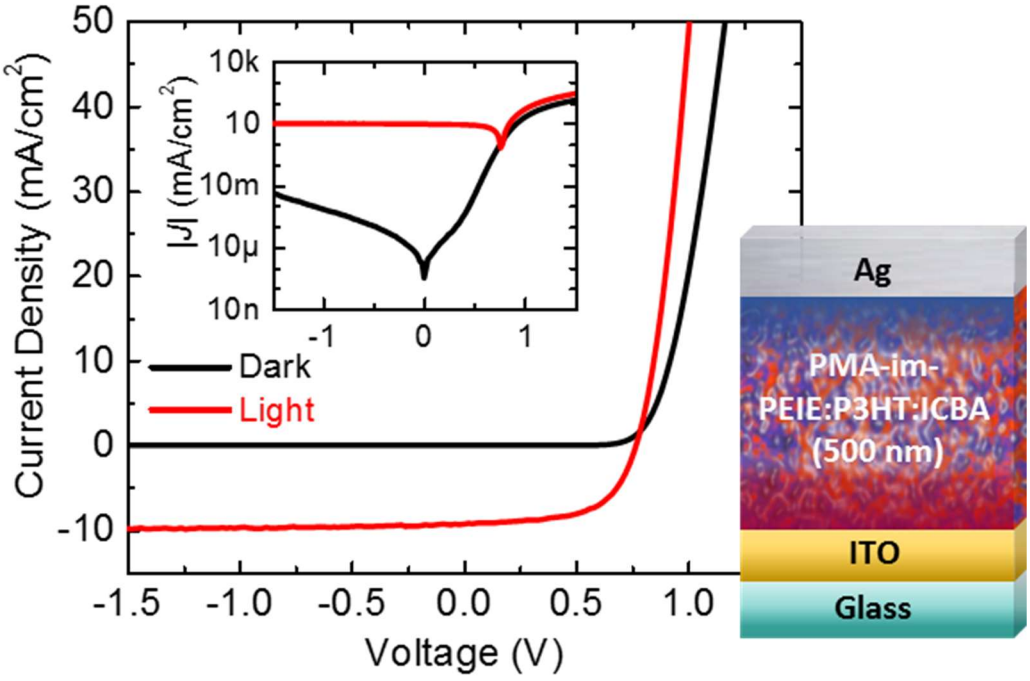

Figure 5-14 *J–V* characteristics and structure of a single-layer ITO/PMA-im-PEIE:P3HT:ICBA (500 nm)/Ag device. The insets show the *J–V* characteristics on a semilogarithmic scale.

In addition, 110 nm-thick single layer PMA-im-PEIE:PIPCP:$PC_{61}BM$ OPV devices also yield a performance comparable to that of two-layer OPVs having ITO/PEIE electron-collecting electrodes (Table 5-1 and Figure 5-15). Here, it is important to highlight that the entire processing of the PMA-im-PEIE:PIPCP:$PC_{61}BM$ layer was carried-out at room-temperature without the need of a post-fabrication thermal annealing step.

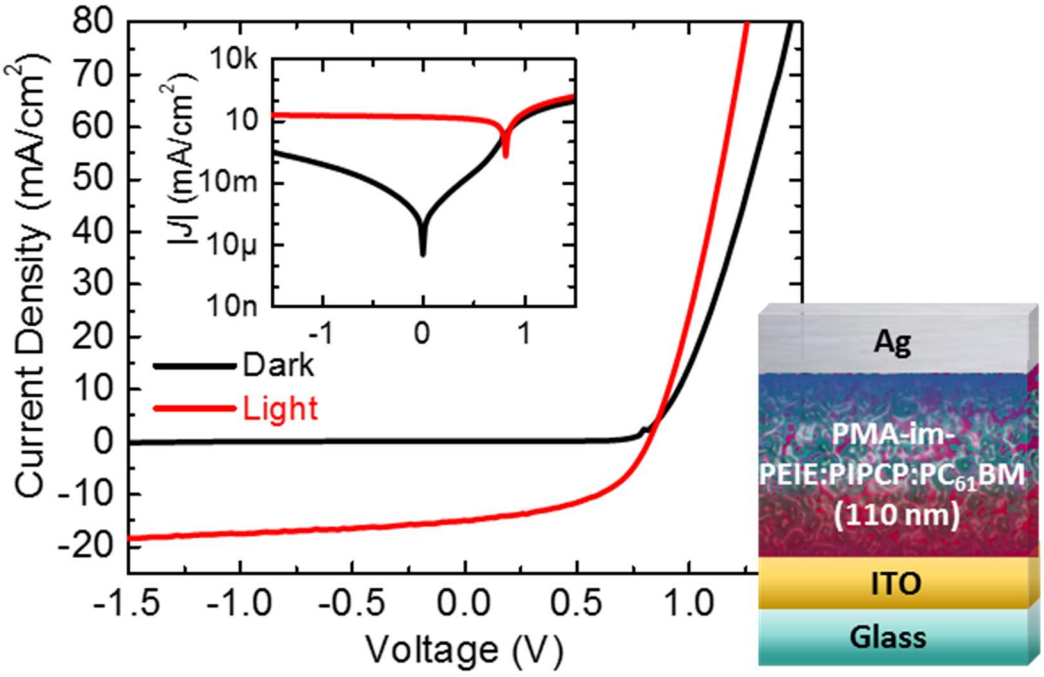

Figure 5-15 *J–V* characteristics and structure of a single-layer ITO/PMA-im-PEIE:PIPCP:$PC_{61}BM$ (110 nm)/Ag device. The insets show the *J–V* characteristics on a semilogarithmic scale.

Table 5-1 Photovoltaic performance parameters of reference and PMA doped devices measured under simulated 100 mW cm^{-2} AM 1.5 G illumination.

Structure	J_{sc} (mA cm^{-2})	V_{oc} (mV)	FF	PCE (%)	Number of Devices
ITO/PEIE/P3HT:ICBA (500 nm)/MoO_3/Ag	8.5 ± 0.6	741 ± 12	0.65 ± 0.02	4.1 ± 0.4	11
ITO/PEIE/PMA-im-P3HT:ICBA (500 nm)/Ag	10.1 ± 0.4	754 ± 8	0.62 ± 0.02	4.8 ± 0.3	15
ITO/PMA-im-PEIE:P3HT:ICBA (500 nm)/Ag	9.6 ± 0.3	771 ± 4	0.60 ± 0.02	4.4 ± 0.2	13
ITO/PEIE/PMA-im-P3HT:ICBA (200 nm)/Ag	7.5 ± 0.3	822 ± 2	0.59 ± 0.01	3.7 ± 0.2	5
ITO/PEIE/PMA-im-P3HT:ICBA (500 nm)/Al*	10.0 ± 0.5	795 ± 2	0.55 ± 0.01	4.4 ± 0.3	8
ITO/PEIE/PIPCP:$PC_{61}BM$ (110 nm)/MoO_3/Ag	15.2 ± 0.2	793 ± 4	0.53 ± 0.01	6.4 ± 0.1	5
ITO/PEIE/PMA-im-PIPCP:$PC_{61}BM$ (110 nm)/Ag	13.6 ± 0.4	799 ± 3	0.55 ± 0.01	6.0 ± 0.1	4
ITO/PMA-im-PEIE:PIPCP:$PC_{61}BM$ (110 nm)/Ag	14.7 ± 0.4	822 ± 11	0.49 ± 0.01	5.9 ± 0.2	4
ITO/PEIE/PffBT4T-2OD:$PC_{71}BM$ (230 nm)/MoO_3/Ag	16.8 ± 0.1	690 ± 4	0.67 ± 0.01	7.7 ± 0.1	10
ITO/PEIE/PMA-im-PffBT4T-2OD:$PC_{71}BM$ (230 nm)/Ag	16.8 ± 0.3	704 ± 1	0.66 ± 0.02	7.8 ± 0.2	4

*Tested without an aperture

5.3 Summary

In summary, the combined properties of PMA-doped polymer layers can be used to facilitate hole injection or collection from organic electronic devices. As a result, it enables a simple approach for the realization of single-layer OPV devices with a scalable method of fabrication, significantly reduces the overall energy budget necessary to fabricate these OPV devices, and is thus expected to have an impact on cost and to shorten the energy pay-back time. These single-layer OPV devices have a simplified geometry and consequently a reduced number of interfaces. Future research will focus on extending the application of this doping technique to a broader range of organic semiconducting materials, including blends of donor polymers and non-fullerene acceptors. Additional thermal and photo-oxidative stability studies should be conducted to further explore the robustness of organic optoelectronic devices fabricated using this method. We believe that the ease and wide applicability of this solution-based method will impact many other device platforms in organic and hybrid printed electronic applications.

CHAPTER 6

Conclusions and Future Work

This chapter will present the conclusions of this work as well as the outlook for future research.

6.1 Conclusions

In summary, this work reported on a novel solution-based method of doping donor polymer and donor-acceptor blend films as well as their application in greatly simplified OPV device structures with only a single-layer sandwiched in between two electrodes. This new design of device architecture has the potential to reduce fabrication costs, lower the thermal budget, and improve device stability, thus leading to much lower energy payback times.

Chapter 4 detailed the post-process immersion technique used to dope various polymer films to limited depths. During studies of the optical properties, additional peaks due to the PMA anions and polymer polarons were observed, indicating penetration of the dopant into the film and suggesting integer charge transfer with the host molecule. Immersion of P3HT films in PMA nitromethane solution for longer times resulted in a decrease of sheet resistance by four orders of magnitude and an increase in the work function by 0.4 eV. Previous methods of electrical doping of polymers used small amounts of p-dopants blended directly with the polymer solution resulting in a processed film containing dopants distributed throughout the bulk [52, 53]. This discovery shows the first time in which a simple post-process immersion of polymer films displayed p-type electrical doping that is self-limiting. It was also discovered that doping of polymer films showed an improved photo-oxidative stability, which has the potential to be a game-changing

breakthrough in improving the device lifetimes of organic optoelectronics implementing this technique. Not only was this approach also shown to extend to a variety of donor polymers used in high efficiency OPV devices, but it can be further applied to materials used in organic light emitting diodes, photodetectors, sensors, and may impact many other device platforms.

In Chapter 5, the new doping approach was applied to OPV devices. Not only did neat polymer films show strong evidence of doping, but it was also evidenced in donor-acceptor blends. The PMA penetrates to a limited depth into the blend and creates a hole-collecting region processed entirely at room temperature in OPV devices. Eliminating the commonly used and vacuum-deposited hole-collecting MoO_3 layer could lead to drastic reduction in material and fabrication costs as well as greatly reducing the thermal budget. The devices with a directly doped photoactive layer show a comparable performance or outperform the reference devices. In previous reports, introducing p-type dopants even at low concentrations directly into the photoactive layer had detrimental effects on device performance, potentially stemming from morphological changes or additional trap-assisted recombination [56, 68]. Other groups have also reported dopant diffusion in organic optoelectronic devices necessitating buffer layers to prevent the device performance deterioration at normal operating conditions [52, 56, 68, 69, 82-85]. We demonstrated that not only is the performance of the solar cells as efficient after doping with PMA and, from variable irradiance measurements, does not seem to indicate any additional recombination, but also that it remains stable and unaffected at temperatures of 60° C, a normal operating temperature for a deployed solar cell, for over 280 hours. Paired with the demonstration of improved photo-oxidative stability of doped polymer films, this can further have a

significant impact on device lifetimes and bring organic solar cells one step closer to becoming a viable commercial PV technology. Furthermore, by blending a small concentration of PEIE into the photoactive layer ink, an electron-collecting region self-assembles on the bottom electrode, we demonstrate the first efficient single-layer OPV device in which the function of light absorption, charge generation, and charge collection is entirely self-contained and sandwiched in between two electrodes. The simplicity of this device geometry resulted in high efficiency solar cells fabricated completely at room-temperature, bringing the possibility of reducing the energy payback times of organic solar cells down to just a few dozen hours much closer to reality [23]. This discovery of simplified single-junction solar cells can be extended to create some of the simplest multi-junction solar cell architectures while improving device efficiencies by absorbing more light.

6.2 Future Work

This work can be further developed and extended in several directions to further exploit all of the benefits of the previously described method. Since the underlying doping mechanism in organic semiconductors is still poorly understood, further studies and characterization of the interaction of PMA and the host materials could open up new avenues in the field of organic solar cells.

6.2.1 Interactions of PMA in Polymer Films

Although XPS studies and optical measurements have revealed that we do indeed have a charge transfer between PMA and the polymer as it penetrates to limited depth into the

film, the exact nature or cause of this interaction is unclear. Further investigation of the mechanism could allow for greater control over the doping concentration and penetration depth of the dopant. Additional characterization using techniques such as atomic-force microscopy (AFM), X-ray diffraction (XRD), Rutherford backscattering (RBS), and secondary ion mass spectroscopy (SIMS) could also reveal whether the penetration is due to a simple diffusion process or due to pinholes in the film. The choice of solvent has also shown to be relevant factor for the doping penetration depth, which needs to be further studied. Controlled doping has been a significant challenge in organic semiconductors, and fully understanding the mechanism behind PMA doping could result in precise control seen in inorganic semiconductors. The process could then be limited to just contact doping or extended to differential doping across an entire film.

6.2.2 Device Stability

Improving OPV device stability and lifetime is one of the most important aspects for the development of widespread and commercial PV technology. In this work, the photo-oxidative stability of neat polymer films doped with PMA was investigated. It showed that the stability did indeed significantly improve after doping. The investigation also demonstrated stability at elevated temperatures of 60 °C for extended periods of time in a nitrogen environment. Extending these studies by measuring completed device photo-oxidative stability in ambient conditions as well as at temperatures >60 °C would be beneficial in determining the effect of PMA doping on lifetimes.

6.2.3 Vacuum-free Solar Cells

Vacuum processes used in the deposition of electrodes for organic solar cells are not a scalable or cost efficient method of device fabrication. To realize the low cost OPVs, the high efficiencies produced in research laboratories must be reproduced using high throughput methods [112]. PMA doping of the photoactive layer creates a hole-collecting region that can replace the often used and thermally evaporated in vacuum MoO_3. Eliminating the top metal contact evaporation would result in a vacuum-free organic solar cell. Several methods have already been developed by using silver nanowires [113, 114], conductive polymers [115], eutectic alloys [116], chemical sintering of Ag nanoparticles [117], and many others. An example of using a low melting point alloy known as the Field's metal in a single-layer structure to fabricate a vacuum-free solar cells is shown in Figure A-1 in the appendix.

6.2.4 Tandem Organic Solar Cells

In an effort to further improve device efficiencies, multi-junction solar cells or tandem cells are fabricated in which the photoactive layers increase the overall absorption of incident photons. Tandem cells connected in series have a resulting open-circuit voltage that is the summation of the two single cells, but it is limited by the smallest short-circuit current in single cells. The delicate balance of obtaining a short-circuit current in the tandem device that does not limit its performance is crucial to its design. By constructing an optical model using the optical constants of each layer and calculating the absorption in each of the single cells, the short-circuit current can be determined for various photoactive layer blends and thicknesses. The most common optical model used for this is known as

the transfer matrix method and is described in detail in Appendix B. Designing a tandem cell with high efficiencies while minimizing fabrication complexity becomes the main challenge. Using our single-layer device structure, one of the simplest tandem cell architectures can be achieved while retaining high device performance as could be seen from the single junction results. With the correct choice of photoactive layers, the simulations show that power conversion efficiencies of close to 12% can be obtained.

6.3 Publication, Presentations, and Patents

Vladimir A. Kolesov, Canek Fuentes-Hernandez, Wen-Fang Chou, Naoya Aizawa, Felipe A. Larrain, Ming Wang, Albertto Perrotta, Sangmoo Choi, Samuel Graham, Guillermo C. Bazan, Thuc-Quyen Nguyen, Seth R. Marder, Bernard Kippelen, "Solution-based electrical doping of semiconducting polymer films over a limited depth." Nature Materials, 2016. http://dx.doi.org/10.1038/nmat4818

Naoya Aizawa, Canek-Fuentes Hernandez, Vladimir A. Kolesov, Talha M. Khan, Junji Kido, and Bernard Kippelen, "Simultaneous cross-linking and p-doping of a polymeric semiconductor film by immersion into a phosphomolybdic acid solution for use in organic solar cells." Chemical Communications, 2016. 52 (3825-3827).

Vladimir A. Kolesov, Bernard Kippelen, Naoya Aizawa, Seth Marder, Canek Fuentes-Hernandez, Junji Kido, Felipe Larrain, Wen-Fang Chou. 2016. "Devices with Organic Semiconductor Layers Electrically-Doped Over a Controlled Depth." Patent Application PCT/US16/35790 based on US 62/173,067. June 3, 2016.

Vladimir A. Kolesov, Canek Fuentes-Hernandez, Naoya Aizawa, Felipe A. Larrain, Wen-Fang Chou, Alberto Perrotta, Samuel Graham, and Bernard Kippelen, "Organic Photovoltaic Devices with a Single-Layer Geometry," SPIE Optics + Photonics, San Diego, California, 2016.

APPENDIX A

Table A-1 All device performance characteristics. Complete set of photovoltaic parameters of reference and PMA doped devices, patterned, and measured through an aperture, averaged over a minimum of 4 devices per structure under simulated 100 mW cm^{-2} AM 1.5 G illumination.

Structure	J_{SC} (mA cm^{-2})	V_{OC} (mV)	FF	PCE (%)
ITO/PEIE/P3HT:ICBA (500 nm)/Ag (No Aperture)	3.7 ± 0.6	134 ± 2	0.26 ± 0.01	0.1 ± 0.1
ITO/PEIE/P3HT:ICBA (500 nm)/MoO_3/Ag (No Aperture)	9.0 ± 0.4	731 ± 2	0.63 ± 0.01	4.2 ± 0.2
ITO/PEIE/P3HT:ICBA (500 nm)/MoO_3/Ag (With Aperture)	8.5 ± 0.6	741 ± 12	0.65 ± 0.02	4.1 ± 0.4
ITO/PEIE/PMA-im-P3HT:ICBA (500 nm)/Ag (Not Electrically Isolated, No Aperture)	11.2 ± 0.4	766 ± 3	0.56 ± 0.01	4.8 ± 0.1
ITO/PEIE/PMA-im-P3HT:ICBA(500 nm)/Ag (Electrically Isolated, No Aperture)	11.2 ± 0.4	770 ± 3	0.58 ± 0.01	5.0 ± 0.1
ITO/PEIE/PMA-im-P3HT:ICBA (500 nm)/Ag (Electrically Isolated, With Aperture)	10.1 ± 0.4	754 ± 8	0.62 ± 0.02	4.8 ± 0.3
ITO/PEIE/PMA-im-P3HT:ICBA (500 nm)/Al (Not Electrically Isolated, No Aperture)	10.0 ± 0.5	795 ± 2	0.55 ± 0.01	4.4 ± 0.3
ITO/PEIE/P3HT:ICBA (200 nm)/PMA-im-P3HT/Ag *Immersed in PMA solution for 5 min	6.0 ± 1.0	821 ± 2	0.55 ± 0.01	2.7 ± 0.5
ITO/PEIE/P3HT:ICBA (200 nm)/PMA-im-P3HT/Ag *Immersed in PMA solution for 15 min	9.0 ± 0.5	835 ± 2	0.54 ± 0.01	4.1 ± 0.3
ITO/PMA-im-PEIE:P3HT:ICBA (500 nm)/Ag (Electrically Isolated, No Aperture)	10.7 ± 0.3	789 ± 4	0.57 ± 0.01	4.9 ± 0.3
ITO/PMA-im-PEIE:P3HT:ICBA (500 nm)/Ag (Electrically Isolated, With Aperture)	9.6 ± 0.3	771 ± 4	0.60 ± 0.02	4.4 ± 0.2
ITO/PEIE/PIPCP:PC_{61}BM (110 nm)/MoO_3/Ag (Electrically Isolated, No Aperture)	16.0 ± 0.3	806 ± 5	0.53 ± 0.01	6.9 ± 0.1
ITO/PEIE/PIPCP:PC_{61}BM (110 nm)/MoO_3/Ag (Electrically Isolated, With Aperture)	15.2 ± 0.2	793 ± 4	0.53 ± 0.01	6.4 ± 0.1
ITO/PEIE/PMA-im-PIPCP:PC_{61}BM (110 nm)/Ag (Electrically Isolated, No Aperture)	13.6 ± 0.4	834 ± 6	0.54 ± 0.01	6.2 ± 0.2
ITO/PEIE/PMA-im-PIPCP:PC_{61}BM (110 nm)/Ag (Electrically Isolated, With Aperture)	13.6 ± 0.4	799 ± 3	0.55 ± 0.01	6.0 ± 0.1
ITO/PMA-im-PEIE:PIPCP:PC_{61}BM (110 nm)/Ag (Electrically Isolated, With Aperture)	14.7 ± 0.4	822 ± 11	0.49 ± 0.01	5.9 ± 0.2
ITO/PEIE/PffBT4T-2OD:PC_{71}BM (230 nm)/MoO_3/Ag (Electrically Isolated, With Aperture)	16.8 ± 0.1	690 ± 4	0.67 ± 0.01	7.7 ± 0.1
ITO/PEIE/PMA-im-PffBT4T-2OD:PC_{71}BM (230 nm)/Ag (Electrically Isolated, With Aperture)	16.8 ± 0.3	704 ± 1	0.66 ± 0.02	7.8 ± 0.2

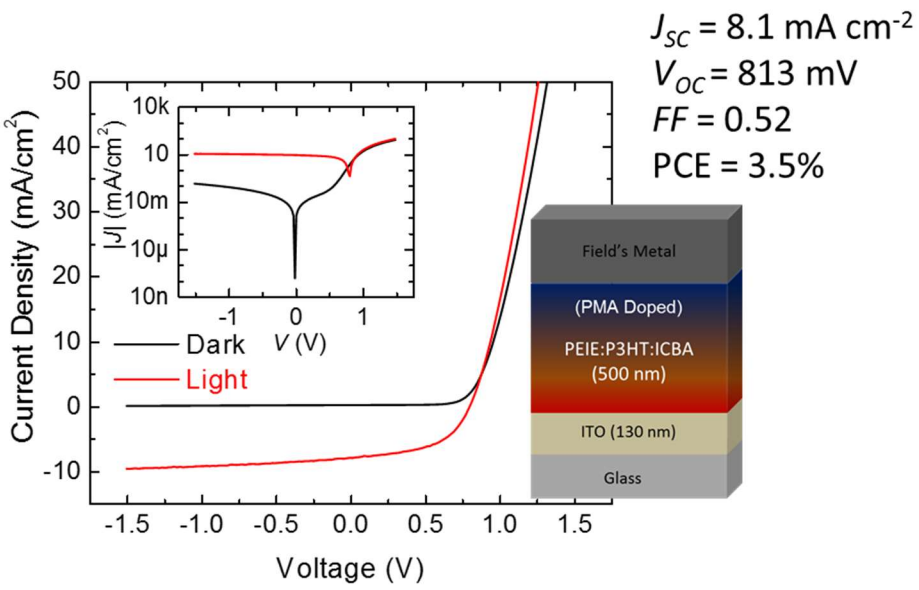

Figure A-1 Vacuum-free solar cell using a low melting point metal alloy (Field's Metal).

APPENDIX B

Optical Modeling of Tandem Organic Solar Cells

B.1 Introduction

Tandem solar cells provide a way to improve device efficiencies through increased overall absorption. Although a three-terminal device with two cells connected in parallel can be designed, the majority of tandem organic solar cells consist of two independent sub-cells connected in series. The general structure of a tandem cell connected in series consists of two or more stacked solar cells separated by a semitransparent recombination layer. The resulting V_{OC} is the sum of the open-circuit voltages of the individual cells $\left(V_{OC,Total} = V_{OC,1} + V_{OC,2}, \text{assuming 2 cells}\right)$ and the J_{SC} is limited by the smallest J_{SC} $\left(J_{SC,Total} = \min\left(J_{SC,1} + J_{SC,2}\right), \text{assuming 2 cells}\right)$. This limitation stresses the importance of balancing the absorption and therefore the photocurrent of the two sub-cells. Typically, this can be achieved either by using active layers with complimentary absorption spectra or two of the same active layer (homo-tandem) with varying thicknesses to obtain greater overall absorption.

The first organic tandem solar cell was reported by Hiramoto *et al.* comprised of two thermally evaporated and stacked sub-cells of metal-free phthalocyanine (H_2PC) and perylene tetracarboxylic derivative (Me-PTC) separated by an ultra-thin (2 nm) Au layer [109]. The addition of the gold layer showed a doubling of the V_{OC}, acting as a recombination site. Solution processed organic tandem cells still pose a challenge in designing a simple and robust recombination layer that prevents the bottom cell from being

dissolved during the processing of the top cell, to maintain overall fabrication simplicity while producing high efficiency devices. This has been accomplished by using a high performance polymeric layer with the combination of PEDOT:PSS/PEIE [110] in tandem OPV devices with efficiencies of 8.2%. A further simplification of the tandem structure was demonstrated by mixing the PEIE directly into the active layer solution, resulting in a self-assembling recombination layer and devices with a PCE of 10.8%. More recently, solution processed organic tandem solar cells have reached efficiencies of >12% [111].

B.2 Modeling Tandem Solar Cells Using the Transfer Matrix Method

To construct an optical model for a multilayer structure such as a tandem organic solar cell, the optical constants n and k can be used to determine the reflection and transmission of electromagnetic radiation at each interface. The solar cell structure can be described by a dielectric medium shown in Figure B-1.

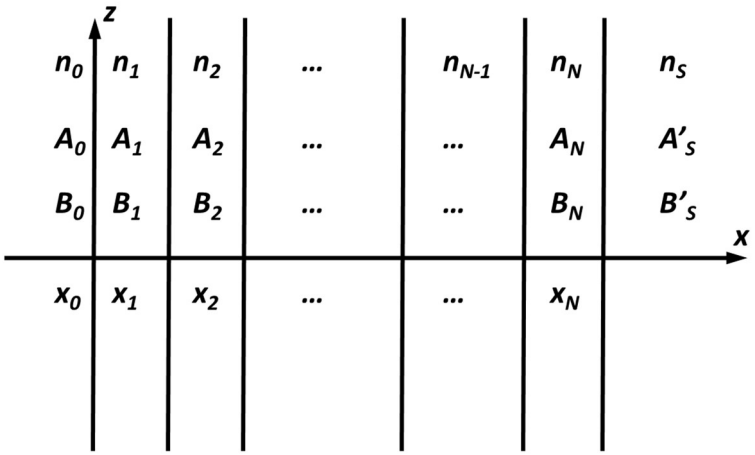

Figure B-1 Multilayer dielectric medium.

Here the complex refractive index of each layer is given by $\hat{n}_N = n_N + ik_N$ and the thickness is given by $d_N = x_N - x_{N-1}$. The electric field of a general plane-wave solution of the wave equation can be written as:

$$E = E(x)e^{i(\omega t - \beta z)} \tag{B-1}$$

where the electric field distribution *E(x)* consists of a left and right propagating wave written as:

$$E(x) = \begin{cases} A_0 e^{-ik_{0x}(x-x_0)} + B_0 e^{ik_{0x}(x-x_0)}, & x < x_0 \\ A_l e^{-ik_{lx}(x-x_l)} + B_l e^{ik_{lx}(x-x_l)}, & x_{l-1} < x < x_l \\ A'_s e^{-ik_{sx}(x-x_N)} + B'_s e^{ik_{sx}(x-x_N)}, & x_N < x \end{cases} \tag{B-2}$$

where A_l and B_l represent the amplitude of the plane waves and k_{lx} is the x component of the wave vectors

$$k_{lx} = n_l \frac{\omega}{c} \cos(\theta_l) \tag{B-3}$$

where θ_l is the angle of incidence onto interface l. The relationship between the electric field amplitudes at adjacent interfaces can be represented as:

$$\begin{pmatrix} A_0 \\ B_0 \end{pmatrix} = D_0^{-1} D_1 \begin{pmatrix} A_1 \\ B_1 \end{pmatrix} \tag{B-4}$$

$$\begin{pmatrix} A_l \\ B_l \end{pmatrix} = P_l D_l^{-1} D_{l+1} \begin{pmatrix} A_{l+1} \\ B_{l+1} \end{pmatrix}, \qquad l = 1,2,\ldots,\mathrm{N} \tag{B-5}$$

where D_l and P_l are the transmission and propagation matrices respectively. The expression for the transmission matrices is given by:

$$D_l^{-1} D_{l+1} = D_{l,l+1} = \frac{1}{t_{l,l+1}} \begin{pmatrix} 1 & r_{l,l+1} \\ r_{l,l+1} & 1 \end{pmatrix} \tag{B-6}$$

where $t_{l,l+1}$ and $r_{l,l+1}$ are the Fresnel transmission and reflection coefficients, given by:

$$r_{l,l+1} = \begin{cases} \frac{k_{lx} - k_{(l+1)x}}{k_{lx} + k_{(l+1)x}} & for\ s\ wave \\ \frac{n_l^2 k_{(l+1)x} - n_{(l+1)}^2 k_{lx}}{n_l^2 k_{(l+1)x} + n_{(l+1)}^2 k_{lx}} & for\ p\ wave \end{cases} \tag{B-7}$$

$$t_{l,l+1} = \begin{cases} \frac{2k_{lx}}{k_{lx} + k_{(l+1)x}} & for\ s\ wave \\ \frac{2n_l^2 k_{(l+1)x}}{n_l^2 k_{(l+1)x} + n_{(l+1)}^2 k_{lx}} & for\ p\ wave \end{cases} \tag{B-8}$$

Phase change and attenuation caused by propagation through a medium is accounted for by the propagation matrix expressed as:

$$P_l = \begin{pmatrix} e^{i\varphi_l} & 0 \\ 0 & e^{-i\varphi_l} \end{pmatrix} \tag{B-9}$$

where $\varphi_l = k_{lx} d_l$. The relationship between the electric field amplitudes at medium 0 ($x=x_0$) and in medium s at ($x=x_N$) is then given by:

$$\begin{pmatrix} A_0 \\ B_0 \end{pmatrix} = \begin{pmatrix} M_{11} & M_{12} \\ M_{21} & M_{22} \end{pmatrix} \begin{pmatrix} A_s' \\ B_s' \end{pmatrix} \tag{B-10}$$

where

$$\begin{pmatrix} M_{11} & M_{12} \\ M_{21} & M_{22} \end{pmatrix} = D_{01} \left(\prod_{l=1}^{N} P_l\, D_{l,l+1} \right) \tag{B-11}$$

From this we can calculate the total transmittance (T), reflectance (R), and absorption (A) by:

$$T = \frac{n_s \cos(\theta_s)}{n_0 \cos(\theta_0)} |t|^2 = \frac{n_s \cos(\theta_s)}{n_0 \cos(\theta_0)} \left| \frac{1}{M_{11}} \right|^2 \tag{B-12}$$

$$R = |r|^2 = \left| \frac{M_{21}}{M_{11}} \right|^2 \tag{B-13}$$

$$A = 1 - (R + T) \tag{B-14}$$

Using the transmitted electric field amplitude (t), the electric field amplitude in each layer can be back calculated, giving the total electric field distribution in each layer by Eq. B-2). The absorptance per unit volume in each layer, including the current generating active layer (AL), can be obtained from the divergence of the Poynting vector $\left(A_{AL} = -\frac{1}{2} Re(\nabla \cdot S) \right)$. The internal quantum efficiency (IQE), or the ratio of the number of charge carriers collected by the solar cell to the number of incident photons absorbed by the solar cell, is then estimated experimentally using a measured J_{SC}, approximated by:

$$IQE \approx \frac{J_{SC,measured}}{q \int A_{AL}(\lambda) S_{AM1.5}(\lambda) d\lambda} \tag{B-15}$$

Using this approximation, the J_{SC} in each subcell of a tandem organic solar cell can be determined by:

$$J_{SC} = q \int IQE_{ALx} A_{ALx}(\lambda) S_{AM1.5}(\lambda) d\lambda \tag{B-16}$$

where *ALx* represents the first or second active layer (AL1 or AL2), and $S_{AM1.5}$ is the AM1.5 solar spectrum.

B.3 Results and Discussion

Using the measured variable angle spectroscopic ellipsometry data with the appended transmittance data we can use a B-spline model to extract the optical constants *n* and *k* for each of the layers in the tandem cell, including the phototactive layers used in the device structure. An example of this for a tandem cell with a PEIE:P3HT:ICBA (PMA doped) bottom active layer and a PffBT4T-2OD:$PC_{71}BM$ top active layer is shown in Figure B-2.

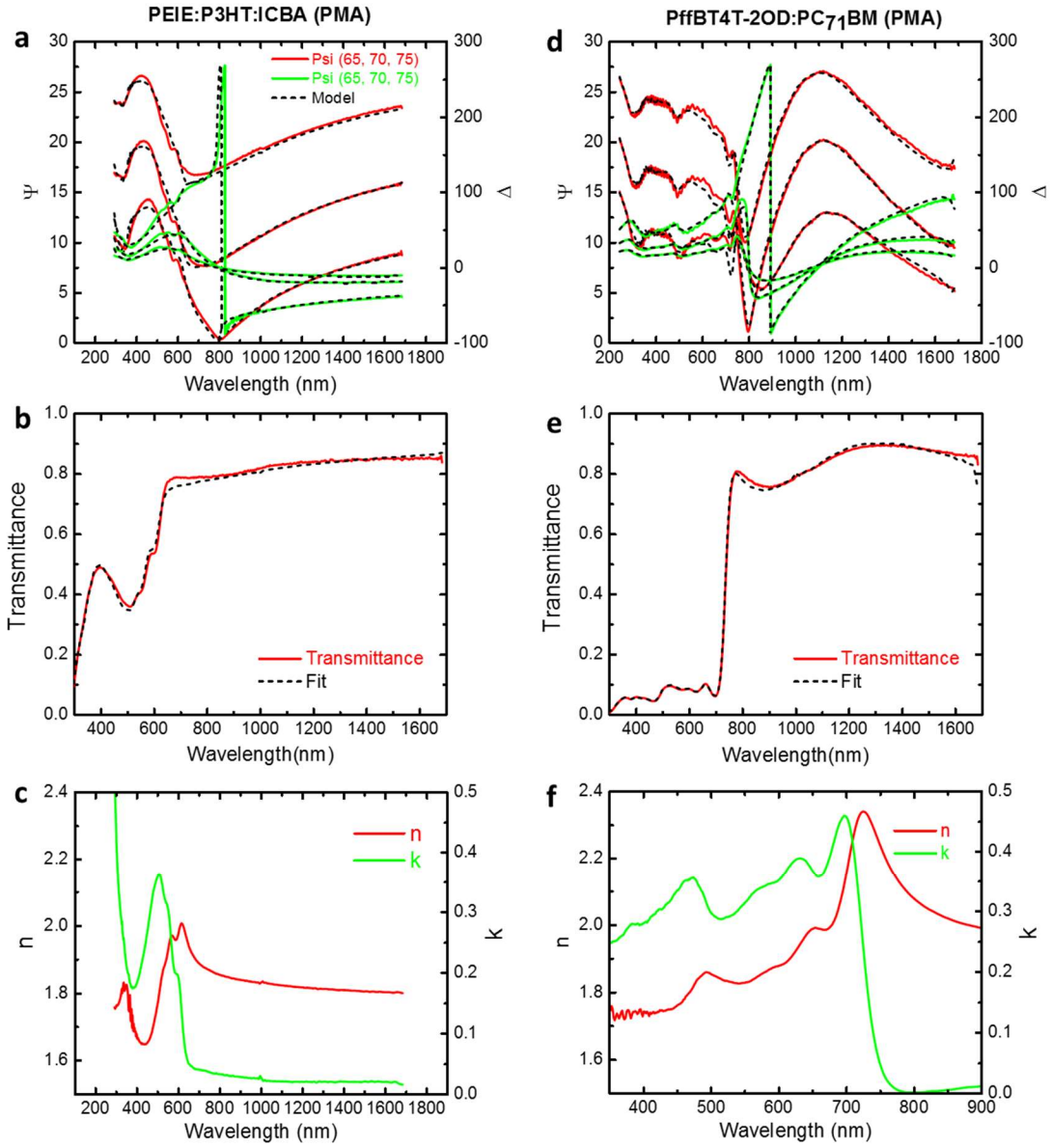

Figure B-2 a,d Variable angle spectroscopic ellipsometry data with fit, **b,e** transmittance data with fit, and **c,f** optical constants for PEIE:P3HT:ICBA (PMA) and PffBT4T-2OD:$PC_{71}BM$.

The device performance of the individual single cells are shown in Figure B-3 and Table B-1.

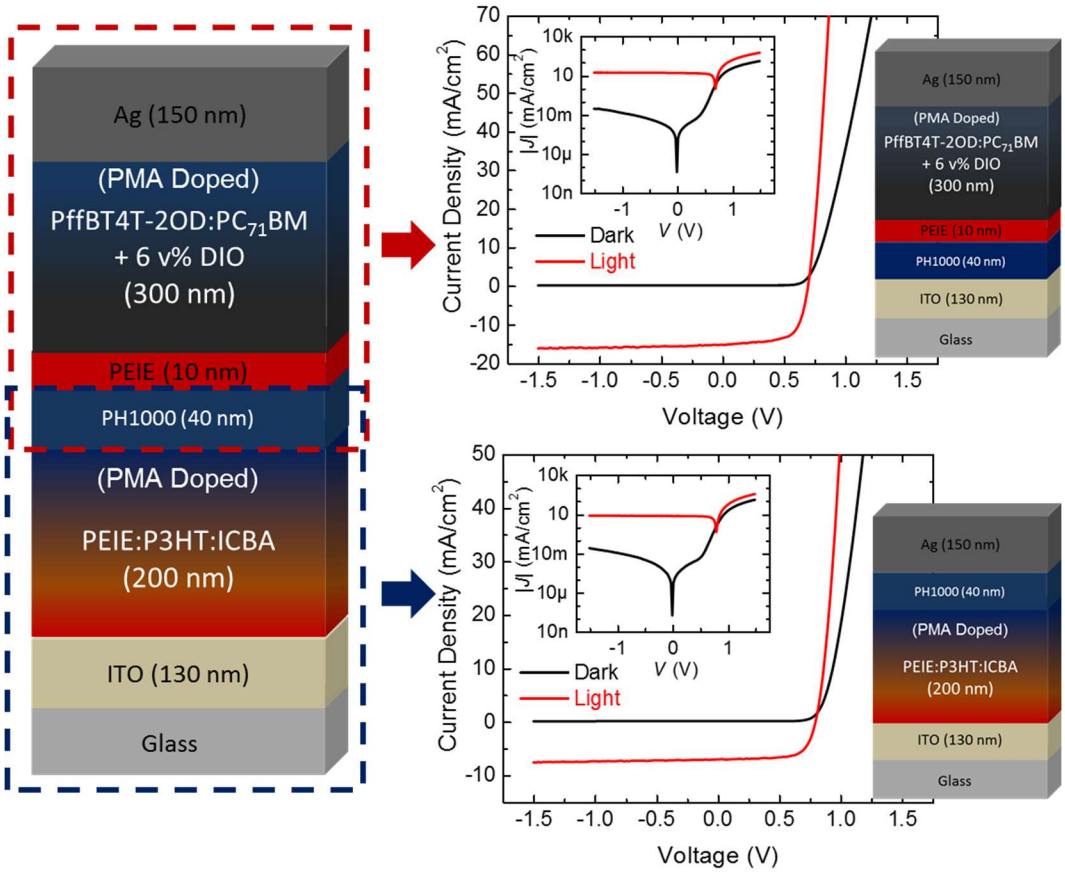

Figure B-3 Tandem solar cell structure and the device performance of the top and bottom cell.

Table B-1 Device performance of the individual cells.

Device	J_{sc} (mA/cm²)	V_{oc} (mV)	FF	PCE (%)
PffBT4T-2OD:$PC_{71}BM$ (PMA Doped)	15.6 ± 0.4	701 ± 3	0.65 ± 0.02	7.1 ± 0.2
PEIE:P3HT:ICBA (PMA Doped)	7.2 ± 0.2	802 ± 3	0.68 ± 0.02	4.0 ± 0.2

From this device performance data, we can extract the internal quantum efficiency using Equation (B-15). Using PH1000 and the amine containing work function reducing surface modifier PEIE as the interconnecting recombination layer in order to obtain the work function contrast necessary to collect holes from the bottom cell and electrons from the top cell, the simple tandem solar cell can be designed. From the optical constants of these active layers we can use the transfer matrix method to determine the J_{SC} for each of the subcells and, therefore, for the entire structure. A plot of the J_{SC} as a function of different thicknesses of the photoactive layers is shown in Figure B-4.

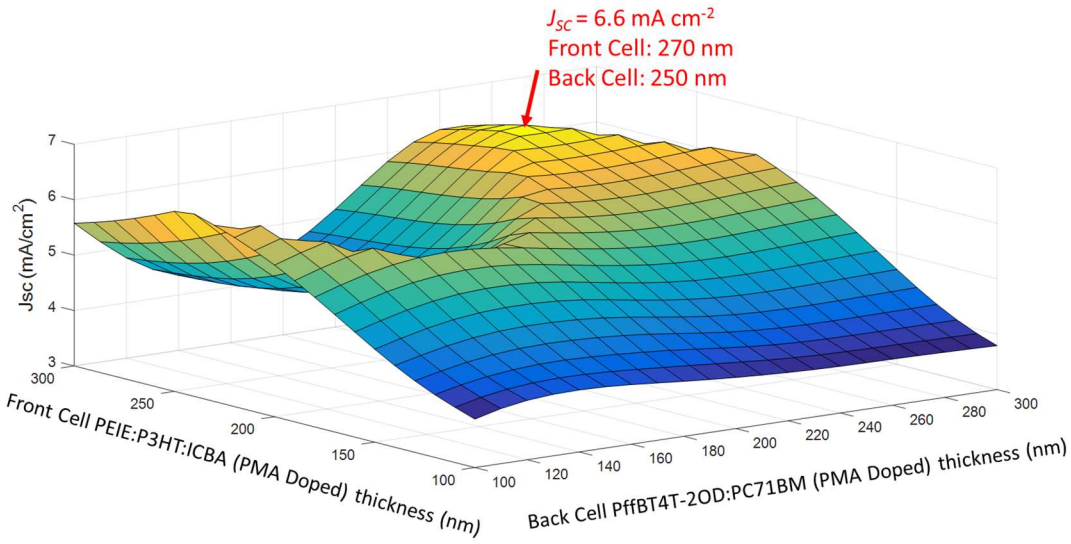

Figure B-4 The short-circuit in a PEIE:P3HT:ICBA (PMA) and PffBT4T-2OD:$PC_{71}BM$ tandem device.

This shows that the maximum attainable short circuit in the tandem device is 6.6 mA cm^{-2}. With the correct choice of active layers and thicknesses, an efficient and simple solar cell can be constructed with a PCE close to 12%. Shown below in Figure B-5 are transfer matrix method simulations for some additional systems.

Front and Back Cells: PIPCP/$PC_{60}BM$

Front cell = 100 nm
Back cell = 150nm
Jsc = 10 mA/cm^2

Front cell = 140 nm
Back cell = 320 nm
Jsc = 11 mA/cm^2

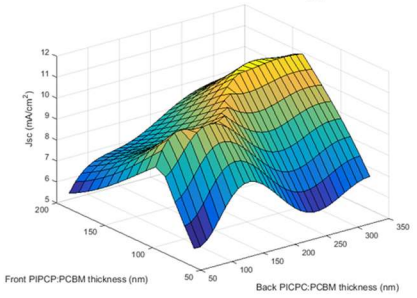

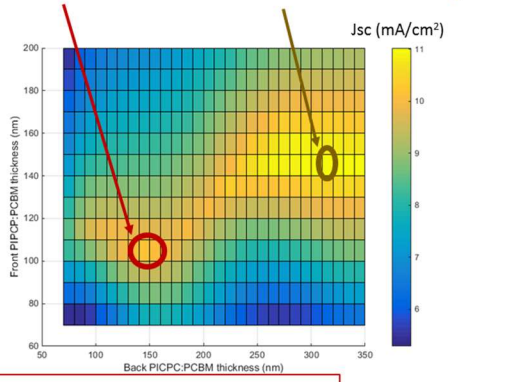

V_{oc} = 1.65 - 1.7 V, *FF* = 0.60, J_{sc} = 10 mA cm^{-2}, PCE= 9.9 -10.2%

Front Cell: PCDTBT/$PC_{70}BM$ and Back Cell: PIPCP/$PC_{60}BM$ layers

Front cell = 160 nm
Back cell = 130 nm
Jsc = 10.5 mA/cm^2

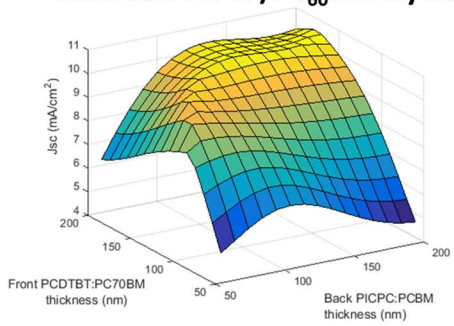

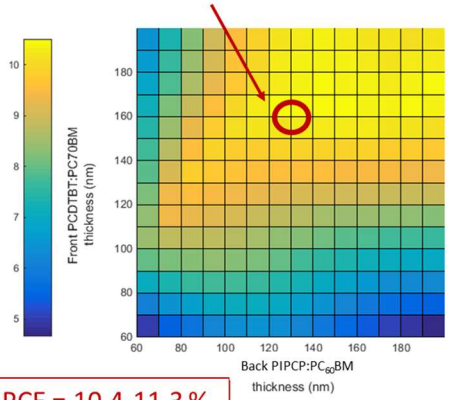

V_{oc} = 1.65 V, *FF* = 0.60 – 0.65, J_{sc} = 10.5 mA cm^{-2}, PCE = 10.4-11.3 %

Front Cell: PBDTT-FTTE:$PC_{70}BM$ Back Cell: PIPCP:$PC_{60}BM$

Front cell = 140 nm
Back cell = 290 nm
Jsc = 10.5 mA/cm^2

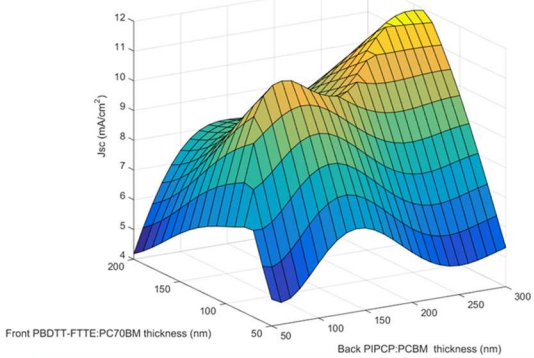

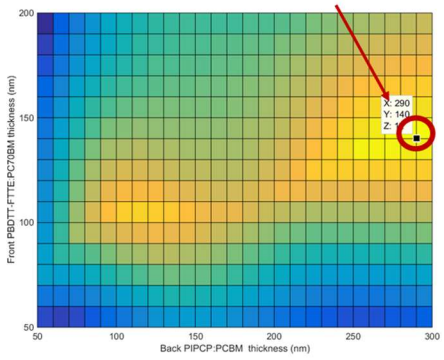

V_{oc} = 1.5 V, FF = 0.60 - 0.65, J_{sc} = 11-12 mA cm^{-2}, PCE = 10.0-11.7 %

Figure B-5 Transfer matrix methods simulations for varying combinations of photoactive layers and thickness with a given estimate of their performance.

B.4 Summary

In summary, an optical model of tandem cell structures was constructed, providing a pathway to high efficiency organic solar cells. The wide applicability of the doping approach indicates that the absorption spectrum of a simplified tandem structure can be tuned by using various donor polymer materials. When two subcells with active layers having complimentary absorption spectra are joined by an interconnecting recombination layer, solar cells with high efficiencies due to their high V_{OC} can be fabricated. This doping approach then allows for the realization of OPV devices having multi-faceted benefits of simplicity and efficiency.

REFERENCES

[1] "Key World Energy Statistics 2016," International Energy Agency, 2016.

[2] "International Energy Outlook 2016," U.S. Energy Information Administration, 2016.

[3] "Renewables 2016 Global Status Report," *Ren21,* 2016.

[4] M. A. Green, *Solar cells: operating principles, technology, and system applications*: Prentice-Hall, 1982.

[5] A. E. Becquerel, "Recherches sur les effets de la radiation chimique de la lumiere solaire au moyen des courants electriques," *Comptes Rendus de L´Academie des Sciences,* vol. 9, 1839.

[6] A. E. Becquerel, "Memoire sur les effects d´electriques produits sous l´influence des rayons solaires," *Annalen der Physick und Chemie,* vol. 54, 1841.

[7] W. G. Adams and R. E. Day, "The Action of Light on Selenium," *Proceedings of the Royal Society, London,* vol. A25, 1877.

[8] D. M. Chapin, C. S. Fuller, and G. L. Pearson, "A New Silicon p-n Junction Photocell for Converting Solar Radiation into Electrical Power," *Journal of Applied Physics,* vol. 25, pp. 676-677, 1954.

[9] P. Wurfel, *Physics of Solar Cells*, 2nd ed. Weinheim, Germany: Wiley-VCH, 2009.

[10] M. A. Green, "Thin-film solar cells: review of materials, technologies and commercial status," *Journal of Materials Science: Materials in Electronics,* vol. 18, pp. 15-19, 2007.

[11] (June). *NREL: National Renewable Laboratory*. Available: www.nrel.gov

[12] C. Battaglia, A. Cuevas, and S. De Wolf, "High-efficiency crystalline silicon solar cells: status and perspectives," *Energy & Environmental Science,* vol. 9, pp. 1552-1576, 2016.

[13] "Photovoltaics Report," Fraunhofer Institute for Solar Energy Systems, 2016.

[14] S. S. Hegedus and A. Luque, "Status, Trends, Challenges and the Bright Future of Solar Electricity from Photovoltaics," in *Handbook of Photovoltaic Science and Engineering*, ed: John Wiley & Sons, Ltd, 2005, pp. 1-43.

[15] M. A. Green, A. Ho-Baillie, and H. J. Snaith, "The emergence of perovskite solar cells," *Nat Photon,* vol. 8, pp. 506-514, 2014.

[16] M. Graetzel, R. A. J. Janssen, D. B. Mitzi, and E. H. Sargent, "Materials interface engineering for solution-processed photovoltaics," *Nature,* vol. 488, pp. 304-312, 2012.

[17] B. O'Regan and M. Gratzel, "A low-cost, high-efficiency solar cell based on dye-sensitized colloidal TiO2 films," *Nature,* vol. 353, pp. 737-740, 1991.

[18] S. Shalini, R. Balasundara prabhu, S. Prasanna, T. K. Mallick, and S. Senthilarasu, "Review on natural dye sensitized solar cells: Operation, materials and methods," *Renewable and Sustainable Energy Reviews,* vol. 51, pp. 1306-1325, 2015.

[19] A. Kojima, K. Teshima, Y. Shirai, and T. Miyasaka, "Organometal Halide Perovskites as Visible-Light Sensitizers for Photovoltaic Cells," *Journal of the American Chemical Society,* vol. 131, pp. 6050-6051, 2009.

[20] M. M. Lee, J. Teuscher, T. Miyasaka, T. N. Murakami, and H. J. Snaith, "Efficient Hybrid Solar Cells Based on Meso-Superstructured Organometal Halide Perovskites," *Science,* vol. 338, pp. 643-647, 2012.

[21] C. W. Tang, "Two-layer organic photovoltaic cell," *Applied Physics Letters,* vol. 48, pp. 183-185, 1986.

[22] H. Hoppe and N. S. Sariciftci, "Organic solar cells: An overview," *Journal of Materials Research,* vol. 19, pp. 1924-1945, 2004.

[23] N. Espinosa, M. Hosel, D. Angmo, and F. C. Krebs, "Solar cells with one-day energy payback for the factories of the future," *Energy & Environmental Science,* vol. 5, pp. 5117-5132, 2012.

[24] D. L. Morel, A. K. Ghosh, T. Feng, E. L. Stogryn, P. E. Purwin, R. F. Shaw*, et al.*, "High-efficiency organic solar cells," *Applied Physics Letters,* vol. 32, pp. 495-497, 1978.

[25] A. K. Ghosh and T. Feng, "Merocyanine organic solar cells," *Journal of Applied Physics,* vol. 49, pp. 5982-5989, 1978.

[26] N. S. Sariciftci, D. Braun, C. Zhang, V. I. Srdanov, A. J. Heeger, G. Stucky*, et al.*, "Semiconducting polymer-buckminsterfullerene heterojunctions: Diodes, photodiodes, and photovoltaic cells," *Applied Physics Letters,* vol. 62, pp. 585-587, 1993.

[27] G. Yu and A. J. Heeger, "Charge separation and photovoltaic conversion in polymer composites with internal donor/acceptor heterojunctions," *Journal of Applied Physics,* vol. 78, pp. 4510-4515, 1995.

[28] I. T. Sachs-Quintana, T. Heumüller, W. R. Mateker, D. E. Orozco, R. Cheacharoen, S. Sweetnam*, et al.*, "Electron barrier formation at the organic-back contact

interface is the first step in thermal degradation of polymer solar cells," *Advanced Functional Materials,* vol. 24, pp. 3978-3985, 2014.

[29] F. Padinger, R. S. Rittberger, and N. S. Sariciftci, "Effects of Postproduction Treatment on Plastic Solar Cells," *Advanced Functional Materials,* vol. 13, pp. 85-88, 2003.

[30] A. Zusan, B. Gieseking, M. Zerson, V. Dyakonov, R. Magerle, and C. Deibel, "The Effect of Diiodooctane on the Charge Carrier Generation in Organic Solar Cells Based on the Copolymer PBDTTT-C," *Scientific Reports,* vol. 5, p. 8286, 2015.

[31] G. Li, V. Shrotriya, Y. Yao, and Y. Yang, "Investigation of annealing effects and film thickness dependence of polymer solar cells based on poly(3-hexylthiophene)," *Journal of Applied Physics,* vol. 98, p. 043704, 2005.

[32] S. H. Park, A. Roy, S. Beaupre, S. Cho, N. Coates, J. S. Moon*, et al.*, "Bulk heterojunction solar cells with internal quantum efficiency approaching 100%," *Nature Photonics,* vol. 3, p. 297, 2009.

[33] H. Y. Chen, J. H. Hou, S. Q. Zhang, Y. Y. Liang, G. W. Yang, Y. Yang*, et al.*, "Polymer solar cells with enhanced open-circuit voltage and efficiency," *Nature Photonics,* vol. 3, pp. 649-653, 2009.

[34] Y. Y. Liang, Z. Xu, J. B. Xia, S. T. Tsai, Y. Wu, G. Li*, et al.*, "For the Bright Future-Bulk Heterojunction Polymer Solar Cells with Power Conversion Efficiency of 7.4%," *Advanced Materials,* vol. 22, pp. E135-E138, 2010.

[35] Y. H. Liu, J. B. Zhao, Z. K. Li, C. Mu, W. Ma, H. W. Hu*, et al.*, "Aggregation and morphology control enables multiple cases of high-efficiency polymer solar cells," *Nature Communications,* vol. 5, p. 8, 2014.

[36] D. R. Klein, *Organic Chemistry, 2nd Edition*: John Wiley & Sons, 2013.

[37] F. A. Carey, *Organic chemistry*: McGraw-Hill, 2000.

[38] J.-L. Bredas, "Mind the gap!," *Materials Horizons,* vol. 1, pp. 17-19, 2014.

[39] C. Kittel, *Introduction to solid state physics*. Hoboken, NJ: Wiley, 2005.

[40] M. Knupfer, "Exciton binding energies in organic semiconductors," *Applied Physics A,* vol. 77, pp. 623-626, 2003.

[41] I. G. Hill, A. Kahn, Z. G. Soos, and R. A. Pascal, "Charge-separation energy in films of pi-conjugated organic molecules," *Chemical Physics Letters,* vol. 327, pp. 181-188, Sep 2000.

[42] W. Zhao, D. Qian, S. Zhang, S. Li, O. Inganäs, F. Gao, *et al.*, "Fullerene-free polymer solar cells with over 11% efficiency and excellent thermal stability," *Advanced Materials,* vol. 28, pp. 4734-4739, 2016.

[43] M. Kaltenbrunner, M. S. White, E. D. Głowacki, T. Sekitani, T. Someya, N. S. Sariciftci, *et al.*, "Ultrathin and lightweight organic solar cells with high flexibility," *Nature Communications,* vol. 3, p. 770, 2012.

[44] V. A. Kolesov, C. Fuentes-Hernandez, W.-F. Chou, N. Aizawa, F. A. Larrain, M. Wang, *et al.*, "Solution-based electrical doping of semiconducting polymer films over a limited depth," *Nat Mater,* vol. advance online publication, 2016.

[45] J. Xue, B. P. Rand, S. Uchida, and S. R. Forrest, "A Hybrid Planar–Mixed Molecular Heterojunction Photovoltaic Cell," *Advanced Materials,* vol. 17, pp. 66-71, 2005.

[46] K. A. Mazzio and C. K. Luscombe, "The future of organic photovoltaics," *Chemical Society Reviews,* vol. 44, pp. 78-90, 2015.

[47] B. Kippelen and J.-L. Bredas, "Organic photovoltaics," *Energy & Environmental Science,* vol. 2, pp. 251-261, 2009.

[48] C. Deibel, T. Strobel, and V. Dyakonov, "Role of the Charge Transfer State in Organic Donor–Acceptor Solar Cells," *Advanced Materials,* vol. 22, pp. 4097-4111, 2010.

[49] *PV Education*. Available: http://pveducation.org/pvcdrom/doping

[50] H. Mendez, G. Heimel, S. Winkler, J. Frisch, A. Opitz, K. Sauer, *et al.*, "Charge-transfer crystallites as molecular electrical dopants," *Nature Communications,* vol. 6, 2015.

[51] S. Olthof, S. Mehraeen, S. K. Mohapatra, S. Barlow, V. Coropceanu, J.-L. Brédas, *et al.*, "Ultralow Doping in Organic Semiconductors: Evidence of Trap Filling," *Physical Review Letters,* vol. 109, p. 176601, 2012.

[52] A. Dai, A. Wan, C. Magee, Y. D. Zhang, S. Barlow, S. R. Marder, *et al.*, "Investigation of p-dopant diffusion in polymer films and bulk heterojunctions: stable spatially-confined doping for all-solution processed solar cells," *Organic Electronics,* vol. 23, pp. 151-157, 2015.

[53] A. Dai, Y. H. Zhou, A. L. Shu, S. K. Mohapatra, H. Wang, C. Fuentes-Hernandez, *et al.*, "Enhanced charge-carrier injection and collection via lamination of doped polymer layers p-doped with a solution-processible molybdenum complex," *Advanced Functional Materials,* vol. 24, pp. 2197-2204, 2014.

[54] P. Pingel and D. Neher, "Comprehensive picture of p-type doping of P3HT with the molecular acceptor F4TCNQ," *Physical Review B,* vol. 87, p. 115209, 2013.

[55] S. J. Yoo and J. J. Kim, "Charge Transport in Electrically Doped Amorphous Organic Semiconductors," *Macromolecular Rapid Communications,* vol. 36, pp. 984-1000, 2015.

[56] I. Salzmann, G. Heimel, M. Oehzelt, S. Winkler, and N. Koch, "Molecular electrical doping of organic semiconductors: fundamental mechanisms and emerging dopant design rules," *Accounts of Chemical Research,* vol. 49, pp. 370-378, 2016.

[57] A. K. K. Kyaw, X. W. Sun, C. Y. Jiang, G. Q. Lo, D. W. Zhao, and D. L. Kwong, "An inverted organic solar cell employing a sol-gel derived ZnO electron selective layer and thermal evaporated MoO3 hole selective layer," *Applied Physics Letters,* vol. 93, p. 221107, 2008.

[58] V. Shrotriya, G. Li, Y. Yao, C.-W. Chu, and Y. Yang, "Transition metal oxides as the buffer layer for polymer photovoltaic cells," *Applied Physics Letters,* vol. 88, p. 073508, 2006.

[59] M. S. White, D. C. Olson, S. E. Shaheen, N. Kopidakis, and D. S. Ginley, "Inverted bulk-heterojunction organic photovoltaic device using a solution-derived ZnO underlayer," *Applied Physics Letters,* vol. 89, p. 143517, 2006.

[60] Y. H. Zhou, C. Fuentes-Hernandez, J. Shim, J. Meyer, A. J. Giordano, H. Li*, et al.*, "A universal method to produce low-work function electrodes for organic electronics," *Science,* vol. 336, pp. 327-332, 2012.

[61] H. Kang, S. Jung, S. Jeong, G. Kim, and K. Lee, "Polymer-metal hybrid transparent electrodes for flexible electronics," *Nat Commun,* vol. 6, 2015.

[62] H. Kang, S. Kee, K. Yu, J. Lee, G. Kim, J. Kim*, et al.*, "Simplified tandem polymer solar cells with an ideal self-organized recombination layer," *Advanced Materials,* vol. 27, pp. 1408-1413, 2015.

[63] I. Deckman, M. Moshonov, S. Obuchovsky, R. Brener, and G. L. Frey, "Spontaneous interlayer formation in OPVs by additive migration due to additive-metal interactions," *Journal of Materials Chemistry A,* vol. 2, pp. 16746-16754, 2014.

[64] I. Dekman, R. Brener, and G. L. Frey, "Thermal metal deposition induces segregation in polymer thin films: a demonstration on OPVs," *Journal of Materials Chemistry C,* vol. 1, pp. 6522-6525, 2013.

[65] B. Maennig, J. Drechsel, D. Gebeyehu, P. Simon, F. Kozlowski, A. Werner*, et al.*, "Organic p-i-n solar cells," *Applied Physics A,* vol. 79, pp. 1-14, 2004.

[66] Heliatek, "Heliatek sets new Organic Photovoltaic world record efficiency of 13.2%," ed. http://www.heliatek.com/en/press/press-releases/details/heliatek-sets-new-organic-photovoltaic-world-record-efficiency-of-13-2, 2016.

[67] K. Walzer, B. Maennig, M. Pfeiffer, and K. Leo, "Highly efficient organic devices based on electrically doped transport layers," *Chemical Reviews,* vol. 107, pp. 1233-1271, 2007.

[68] A. Loiudice, A. Rizzo, M. Biasiucci, and G. Gigli, "Bulk heterojunction versus diffused bilayer: the role of device geometry in solution p-doped polymer-based solar cells," *Journal of Physical Chemistry Letters,* vol. 3, pp. 1908-1915, 2012.

[69] M. M. Mandoc, F. B. Kooistra, J. C. Hummelen, B. de Boer, and P. W. M. Blom, "Effect of traps on the performance of bulk heterojunction organic solar cells," *Applied Physics Letters,* vol. 91, p. 263505, 2007.

[70] G. K. Mor, D. Jones, T. P. Le, Z. Shang, P. J. Weathers, M. K. B. Woltermann*, et al.*, "Contact Doping with Sub-Monolayers of Strong Polyelectrolytes for Organic Photovoltaics," *Advanced Energy Materials,* vol. 4, 2014.

[71] J. F. Keggin, "Structure of the crystals of 12-phosphotungstic acid," *Nature,* vol. 132, pp. 351-351, 1933.

[72] N. Aizawa, Y.-J. Pu, T. Chiba, S. Kawata, H. Sasabe, and J. Kido, "Instant low-temperature cross-linking of poly(N-vinylcarbazole) for solution-processed multilayer blue phosphorescent organic light-emitting devices," *Advanced Materials,* vol. 26, pp. 7543-7546, 2014.

[73] Y. W. Zhu, Z. C. Yuan, W. Cui, Z. W. Wu, Q. J. Sun, S. D. Wang*, et al.*, "A cost-effective commercial soluble oxide cluster for highly efficient and stable organic solar cells," *Journal of Materials Chemistry A,* vol. 2, pp. 1436-1442, 2014.

[74] X. Jia, L. Shen, M. N. Yao, Y. Liu, W. J. Yu, W. B. Guo*, et al.*, "Highly efficient low-bandgap polymer solar cells with solution-processed and annealing-free phosphomolybdic acid as hole-transport layers," *Acs Applied Materials & Interfaces,* vol. 7, pp. 5367-5372, 2015.

[75] M. Alaaeddine, Q. Zhu, D. Fichou, G. Izzet, J. E. Rault, N. Barrett*, et al.*, "Enhancement of photovoltaic efficiency by insertion of a polyoxometalate layer at the anode of an organic solar cell," *Inorganic Chemistry Frontiers,* vol. 1, pp. 682-688, 2014.

[76] M. Vasilopoulou, E. Polydorou, A. M. Douvas, L. C. Palilis, S. Kennou, and P. Argitis, "Annealing-free highly crystalline solution-processed molecular metal oxides for efficient single-junction and tandem polymer solar cells," *Energy & Environmental Science,* vol. 8, pp. 2448-2463, 2015.

[77] N. Aizawa, C. Fuentes-Hernandez, V. A. Kolesov, T. M. Khan, B. Kippelen, and J. Kido, "Simultaneous cross-linking and p-doping of a polymeric semiconductor film by immersion into a phosphomolybdic acid solution for use in organic solar cells," *Chemical Communications,* vol. 52, pp. 3825-3827, 2016.

[78] C.-W. Chu, H. Yang, W.-J. Hou, J. Huang, G. Li, and Y. Yang, "Control of the nanoscale crystallinity and phase separation in polymer solar cells," *Applied Physics Letters,* vol. 92, p. 103306, 2008.

[79] C. Y. Kwong, A. B. Djurišić, P. C. Chui, K. W. Cheng, and W. K. Chan, "Influence of solvent on film morphology and device performance of poly(3-hexylthiophene):TiO2 nanocomposite solar cells," *Chemical Physics Letters,* vol. 384, pp. 372-375, 2004.

[80] T. Takahashi, H. Tokailin, and T. Sagawa, "Angle-resolved ultraviolet photoelectron-spectroscopy of the unoccupied band-structure of graphite," *Physical Review B,* vol. 32, pp. 8317-8324, 1985.

[81] N. Sai, K. Leung, J. Zador, and G. Henkelman, "First principles study of photo-oxidation degradation mechanisms in P3HT for organic solar cells," *Physical Chemistry Chemical Physics,* vol. 16, pp. 8092-8099, 2014.

[82] G. K. Mor, D. Jones, T. P. Le, Z. R. Shang, P. J. Weathers, M. K. B. Woltermann*, et al.*, "Contact doping with sub-monolayers of strong polyelectrolytes for organic photovoltaics," *Advanced Energy Materials,* vol. 4, pp. 1-6, 2014.

[83] J. Li, C. W. Rochester, I. E. Jacobs, S. Friedrich, P. Stroeve, M. Riede*, et al.*, "Measurement of small molecular dopant F4TCNQ and C60F36 diffusion in organic bilayer architectures," *ACS Applied Materials & Interfaces,* vol. 7, pp. 28420-28428, 2015.

[84] B. X. Mi, Z. Q. Gao, K. W. Cheah, and C. H. Chen, "Organic light-emitting diodes using 3,6-difluoro-2,5,7,7,8,8-hexacyanoquinodimethane as p-type dopant," *Applied Physics Letters,* vol. 94, p. 073507, 2009.

[85] J. Huang, J. Blochwitz-Nimoth, M. Pfeiffer, and K. Leo, "Influence of the thickness and doping of the emission layer on the performance of organic light-emitting diodes with PiN structure," *Journal of Applied Physics,* vol. 93, pp. 838-844, 2003.

[86] H.-Y. Chen, J. Hou, S. Zhang, Y. Liang, G. Yang, Y. Yang*, et al.*, "Polymer solar cells with enhanced open-circuit voltage and efficiency," *Nature Photonics,* vol. 3, pp. 649-653, 2009.

[87] M. Wang, H. B. Wang, T. Yokoyama, X. F. Liu, Y. Huang, Y. Zhang*, et al.*, "High open circuit voltage in regioregular narrow band gap polymer solar cells," *Journal of the American Chemical Society,* vol. 136, pp. 12576-12579, 2014.

[88] W. Ma, G. Yang, K. Jiang, J. H. Carpenter, Y. Wu, X. Meng*, et al.*, "Influence of processing parameters and molecular weight on the morphology and properties of high-performance PffBT4T-2OD:PC71BM organic solar cells," *Advanced Energy Materials,* vol. 5, p. 1, 2015.

[89] H. Sirringhaus, "25th anniversary article: organic field-effect transistors: the path beyond amorphous silicon," *Advanced Materials,* vol. 26, pp. 1319-1335, 2014.

[90] P. J. Brown, D. S. Thomas, A. Kohler, J. S. Wilson, J. S. Kim, C. M. Ramsdale*, et al.*, "Effect of interchain interactions on the absorption and emission of poly(3-hexylthiophene)," *Physical Review B,* vol. 67, p. 16, 2003.

[91] P. J. Brown, H. Sirringhaus, M. Harrison, M. Shkunov, and R. H. Friend, "Optical spectroscopy of field-induced charge in self-organized high mobility poly(3-hexylthiophene)," *Physical Review B,* vol. 63, p. 11, 2001.

[92] J.-L. Burgot, "Ionic Equilibria in Analytical Chemistry," in *Ionic Equilibria in Analytical Chemistry*, ed: Springer, 2012, p. 772.

[93] R. C. Shallcross, T. Stubhan, E. L. Ratcliff, A. Kahn, C. J. Brabec, and N. R. Armstrong, "Quantifying the extent of contact doping at the interface between high work function electrical contacts and poly(3-hexylthiophene) (P3HT)," *The Journal of Physical Chemistry Letters,* vol. 6, pp. 1303-1309, 2015.

[94] B. Maennig, J. Drechsel, D. Gebeyehu, P. Simon, F. Kozlowski, A. Werner*, et al.*, "Organic p-i-n solar cells," *Applied Physics a-Materials Science & Processing,* vol. 79, pp. 1-14, 2004.

[95] C. Liu, Y. Xu, and Y.-Y. Noh, "Contact engineering in organic field-effect transistors," *Materials Today,* vol. 18, pp. 79-96, 2015.

[96] B. Lüssem, M. Riede, and K. Leo, "Doping of organic semiconductors," *physica status solidi (a),* vol. 210, pp. 9-43, 2013.

[97] R. Meerheim, M. Furno, S. Hofmann, B. Lüssem, and K. Leo, "Quantification of energy loss mechanisms in organic light-emitting diodes," *Applied Physics Letters,* vol. 97, p. 253305, 2010.

[98] S.-J. Yoo and J.-J. Kim, "Charge transport in electrically doped amorphous organic semiconductors," *Macromolecular Rapid Communications,* vol. 36, pp. 984-1000, 2015.

[99] B. Shamieh, S. Obuchovsky, and G. L. Frey, "Spontaneous generation of interlayers in OPVs with silver cathodes: enhancing Voc and lifetime," *Journal of Materials Chemistry C,* vol. 4, pp. 1821-1828, 2016.

[100] D. Ma, M. Lv, M. Lei, J. Zhu, H. Wang, and X. Chen, "Self-organization of amine-based cathode interfacial materials in inverted polymer solar cells," *ACS Nano,* vol. 8, pp. 1601-1608, 2014.

[101] Z. a. Tan, D. Qian, W. Zhang, L. Li, Y. Ding, Q. Xu*, et al.*, "Efficient and stable polymer solar cells with solution-processed molybdenum oxide interfacial layer," *Journal of Materials Chemistry A,* vol. 1, pp. 657-664, 2013.

[102] C. Girotto, E. Voroshazi, D. Cheyns, P. Heremans, and B. P. Rand, "Solution-processed MoO3 thin films as a hole-injection layer for organic solar cells," *ACS Applied Materials & Interfaces,* vol. 3, pp. 3244-3247, 2011.

[103] S. Murase and Y. Yang, "Solution processed MoO3 interfacial layer for organic photovoltaics prepared by a facile synthesis method," *Advanced Materials,* vol. 24, pp. 2459-2462, 2012.

[104] G. Wang, T. Jiu, P. Li, J. Li, C. Sun, F. Lu*, et al.*, "In situ growth of columnar MoO3 buffer layer for organic photovoltaic applications," *Organic Electronics,* vol. 15, pp. 29-34, 2014.

[105] J. Meyer, S. Hamwi, M. Kroger, W. Kowalsky, T. Riedl, and A. Kahn, "Transition metal oxides for organic electronics: energetics, device physics and applications," *Advanced Materials,* vol. 24, pp. 5408-5427, 2012.

[106] D. R. Lide, *CRC Handbook of Chemistry and Physics*, 2015.

[107] A. W. Dweydari and C. H. B. Mee, "Work function measurements on (100) and (110) surfaces of silver," *physica status solidi (a),* vol. 27, pp. 223-230, 1975.

[108] N. A. Ran, J. A. Love, C. J. Takacs, A. Sadhanala, J. K. Beavers, S. D. Collins*, et al.*, "Harvesting the full potential of photons with organic solar cells," *Advanced Materials,* vol. 28, pp. 1482-1488, 2016.

[109] H. Masahiro, S. Minoru, and Y. Masaaki, "Effect of Thin Gold Interstitial-layer on the Photovoltaic Properties of Tandem Organic Solar Cell," *Chemistry Letters,* vol. 19, pp. 327-330, 1990.

[110] Y. Zhou, C. Fuentes-Hernandez, J. W. Shim, T. M. Khan, and B. Kippelen, "High performance polymeric charge recombination layer for organic tandem solar cells," *Energy & Environmental Science,* vol. 5, pp. 9827-9832, 2012.

[111] M. Li, K. Gao, X. Wan, Q. Zhang, B. Kan, R. Xia*, et al.*, "Solution-processed organic tandem solar cells with power conversion efficiencies >12%," *Nat Photon,* vol. advance online publication, 2016.

[112] R. J. Peh, Y. R. Lu, F. L. Zhao, C. L. K. Lee, and W. L. Kwan, "Vacuum-free processed transparent inverted organic solar cells with spray-coated PEDOT:PSS anode," *Solar Energy Materials and Solar Cells,* vol. 95, pp. 3579-3584, 2011.

[113] F. Guo, N. Li, V. V. Radmilovic, V. R. Radmilovic, M. Turbiez, E. Spiecker*, et al.*, "Fully printed organic tandem solar cells using solution-processed silver nanowires and opaque silver as charge collecting electrodes," *Energy & Environmental Science,* vol. 8, pp. 1690-1697, 2015.

[114] G. A. D. Benatto, B. Roth, M. Corazza, R. R. Sondergaard, S. A. Gevorgyan, M. Jorgensen*, et al.*, "Roll-to-roll printed silver nanowires for increased stability of flexible ITO-free organic solar cell modules," *Nanoscale,* vol. 8, pp. 318-326, 2016.

[115] J. H. Tong, S. X. Xiong, Y. F. Zhou, L. Mao, X. Min, Z. F. Li*, et al.*, "Flexible all-solution-processed all-plastic multijunction solar cells for powering electronic devices," *Materials Horizons,* vol. 3, pp. 452-459, 2016.

[116] E. Pérez-Gutiérrez, D. Barreiro-Argüelles, J.-L. Maldonado, M.-A. Meneses-Nava, O. Barbosa-García, G. Ramos-Ortíz*, et al.*, "Semiconductor Polymer/Top Electrode Interface Generated by Two Deposition Methods and Its Influence on Organic Solar Cell Performance," *ACS Applied Materials & Interfaces,* vol. 8, pp. 28763-28770, 2016.

[117] S. Magdassi, M. Grouchko, O. Berezin, and A. Kamyshny, "Triggering the Sintering of Silver Nanoparticles at Room Temperature," *ACS Nano,* vol. 4, pp. 1943-1948, 2010.